On the Role of Inertial Instability in Stratosphere Troposphere Exchange and the Generation of Inertial Flare-ups near Midlatitude Jets

by

Shellie M. Rowe

A thesis submitted in partial fulfillment of

the requirements for the degree of

Master of Science

(Atmospheric and Oceanic Sciences)

at the

UNIVERSITY OF WISCONSIN – MADISON

2014

Table of Contents

Acknowledgements

I would like to express my sincere gratitude to Professor Matthew Hitchman for his continual guidance, support, advising and expertise throughout the duration of this work. Additional thanks goes to Pete Pokrandt for his help in solving computer glitches that arose along the way. A final word of thanks goes to Professor Greg Tripoli and to Professor Jon Martin. Their input regarding this work was extremely valuable.

List of Figures

isosurface of 4 cm/s. Top left and top right panels also show EPV at the surface, where red shows negative EPV and blue shows EPV larger than 1 PVU. The ribbons in top right panel show trajectories arriving at the region of anomalous EPV in the upper troposphere originating 14 hours earlier. Middle right and left panels also show the red speed isosurface of 60 m/s, while details of EPV (black contours, interval 1 PVU) are highlighted in color, ranging from low values in blue to high values in red. Bottom left panel shows the distribution of TKE (black contours, interval 0.5 m^2/s^2) and Ri in color (blue < 0.25, red > 1). Bottom right panel shows the meridional circulation in the section (arrows), regions of negative EPV (white), a green jet isosurface of 30 m/s, and 24 hr average precipitable water (red exceeds 0.8 kg/m^2).

Figure 4. Synoptic setting for Case 2, using NCEP eta analysis for 0000 UT 23 April 2005: top left panel) sea level pressure (blue contours, interval 4 hPa), top right panel) 850 hPa temperature (color bar, interval 3^oC), middle left panel) 700 hPa vertical pressure velocity (color bar, interval 1 Pa/s), middle right panel) 300 hPa wind speed (color bar, interval 10 m/s), bottom left panel) 300-250 hPa EPV (color bar, interval 1 PVU), and bottom right panel) 24-hr accumulated precipitation during 0000 UT 22 April – 0000 UT 23 April 2005 (color bar, in inches).

Figure 5. UWNMS simulation of Case 2, initialized with ECWMF data on 22 April 2005 showing the relationship among convection along the cold front, negative EPV, and jet location. Top left panel shows a section of EPV (black contours, interval 1 PVU), an isosurface of -2 PVU (dark blue), and thunderstorm updrafts (green isosurfaces of 4 cm/s). Top left panel also shows EPV at the surface (red for EPV < 0 and blue > 1 PVU). The colored ribbons in the top left panel show trajectories arriving at the region of anomalous EPV in the upper troposphere originating 14 hr earlier. Top right panel 2030 UT 22 April, middle left panel 2200 UT 22 April, and middle right panel 0100 23 April show the evolution of anomalous PV (dark blue isosurface

of -2 PVU) and EPV (low in blue, high in red). Contours in top right panel show wind speed every 10 m/s, while those in the middle left and the middle right show PV every 0.1 PVU. Bottom left panel shows the distribution of TKE (contour interval 0.5) and Ri (blue < 0.25, red > 1.0) at 1800 UT 22 April. Bottom right panel shows the meridional circulation around the jet (arrows), regions of negative EPV (white), wind speed contours every 10 m/s, and 24 hr average precipitable water (red exceeds 0.8 kg/m^2) at 2130 UT 22 April.

Figure 5. Synoptic setting for Case 3, using NCEP Eta reanalysis for 1200 UT 20 February 2011: a) sea level pressure (blue contours, interval 4 hPa), b) 850 hPa temperature (color bar, interval 3^oC), c) 700 hPa vertical pressure velocity (color bar, interval 1 Pa/s), d) 300 hPa wind (color bar, interval 10 m/s), e) 300-250 hPa EPV (color bar, interval 1 PVU), and f) 24-hr accumulated precipitation during 0000Z 20 February – 0000Z 21 February 2011 (color bar, in inches).

Figure 6. UWNMS simulation of Case 2 using GOES Ozone showing the relationship between STE, ozone and negative EPV. All panels show jet wind speeds (black contours, every 4 m/s), EPV (light blue contours, every 1 PVU), and red shading (high ozone levels), yellow shading (moderate ozone levels), and blue shading (low ozone levels). Top row (left panel) is at 2000 UTC on 22 April 2005. Top row (right panel) is at 2200 UTC on 22 April 2005. Bottom row (left panel) is at 2330 UTC on 22 April 2005. Bottom row (right panel) is at 0500 UTC 23 April 2005.

Figure 7. Synoptic setting for Case 3, using NCEP eta analysis for 0000 UT 21 February 2011: Top left panel) sea level pressure (blue contours, interval 4 hPa), Top right panel) 850 hPa temperature (color bar, interval 3^oC), Middle left panel) 700 hPa vertical pressure velocity (color bar, interval 1 Pa/s), Middle right panel) 300 hPa wind (color bar, interval 10 m/s), Bottom left

panel) 300-250 hPa EPV (color bar, interval 1 PVU), and Bottom right panel) 24-hr accumulated precipitation during 0000Z 20 February – 0000Z 21 February 2011 (color bar, in inches).

Figure 8. UWNMS simulation of Case 3, initialized with ECWMF data on 1200 UT 20 February 2011, showing the relationship between convection along the cold front, negative EPV, and jet location. A green updraft isosurface of 4 cm/s is shown in Top left panel) 0430 UT, Top right panel) 0400 UT, Middle left panel) 0330 UT, and Middle right panel) 0720 UT on 20 February. Top left and top right panels show an isosurface of -2 PVU (dark blue) and EPV at the surface (red EPV < 0, blue EPV > 1 PVU). The section in the top left panel has contours every 0.1 PVU, while the top right panel shows speed contours every 5 m/s. The colored ribbons in the top left panel show trajectories arriving at the region of anomalous EPV in the upper troposphere originating 14 hr earlier. Middle left and middle right panels show the evolution of EPV, ranging from low (blue) to high (red) values. Bottom left panel shows the distribution of TKE (contours every 0.5 m^2/s^2) and Ri (blue < 0.25, red > 1.0) at 2100 UT 20 February. Bottom right panel shows the meridional circulation around the jet (arrows), regions of negative EPV (white), an isosurface of 30 m/s wind speed (green), and 24 hr average precipitable water (red exceeds 0.8 kg/m^2).

Figure 9. Idealized 300 mb jet streak. Imbalances between the Coriolis force and the pressure gradient force as air flows through a jet streak create areas of upper air convergence (shown in points 2 and 3) and areas of upper air divergence (shown in points 1 and 4). It is these areas of upper air divergence that cause enhanced jet accelerations. (A world of Weather: Fundamentals of Meteorology: a Text Laboratory Manual)

Figure 10. UWNMS simulation of Case 1 initialized with ECMWF data on 00 UTC 6 February 2008 showing relationship between inertial instability and jet speed increase. Top left panel shows a cross section of total wind speed (black contours, interval 5 m/s) and an isosurface of EPV (dark blue, -3 PVU) at 1400 UTC on 6 January 2008. At this time a 60 m/s jet core wind speed is evident. Top right panel (same as in top left) except 1700 UTC on 6 January 2008 is shown. As inertially unstable air (blue shading) interacts with the anticyclonic shear side of the jet, wind speed increases to 75 m/s. Bottom left panel (same as in top left and top right) except 0030 UTC on 7 February 2008 is shown) Inertially unstable air leaves the plane of the cross section and jet core wind speed reduces to 65 m/s.

Figure 11. UWNMS simulation of Case 1 initialized with ECMWF data on 00 UTC 6 February 2008 showing relationship between inertial instability and enhanced divergence associated with jet wind speed increase. Top left panel shows a cross section of wind speed (blue contours, 4 m/s) isosurface of jet (65 m/s), shaded in blue (divergence) and red (convergence) and an isosurface of inertial instability (green shading, -3 PVU) at 1700 UTC on 6 February 2008. As inertially unstable air enhances the divergence in the jet, a distinctive tightening of the isotachs occurs. At 1700 UTC a 75 m/s jet core is identified. At 1730 UTC (top right panel) an 80 m/s jet core wind speed is evident as divergence is enhanced through inertial instability. Bottom left panel (same as in top left and top right) shows 2330 UTC and a relaxation of the jet core as inertially unstable air is less intense. Bottom right (same as in top left and top right and bottom left) only at 0330 UTC on 7 February 2008, shows more enhanced divergence due to the presence of inertial instability and once again a tightening of the isotachs.

Figure 12. UWNMS simulation of Case 1 initialized with ECMWF data on 00 UTC 6 February 2008 showing the relationship between negative absolute vorticity, divergence, negative EPV and a tightening of the isotachs. Left panels show absolute vorticity, (blue shading is negative, red shading is positive), and divergence (white contours, interval 5 x 10^{-5} s^{-1}). Right panels show negative EPV (blue shading is negative, red shading is positive) and jet wind speeds (black contours, every 4 m/s). Top panels are at 0830 UTC on 7 February 2008. Middle panels are at 0930 UTC 7 February 2008. Bottom panels are at 1130 UTC 7 February 2008.

Figure 13. UWNMS simulation of Case 2 initialized at 00 UTC on 22 April 2005 showing the relationship between inertial instability and jet wind speed increase (inertial flare-up). Top left panel shows a cross section of total wind speed (dark blue contours, 3 m/s) and an isosurface of inertial instability (blue isosurface, -1.5 PVU) at 1630 UTC on 22 April 2005. A minor inertial flare-up is evident with a jet core of 15 m/s. Top right panel (same as in top left) at 2000 UTC on 22 April 2005, a more intense inertial flare-up at 30 m/s is evident as more organized areas of inertial instability are present on the anticyclonic shear side of the jet. Bottom left (same as in top left and top right) at 2030 UTC on 22 April 2005 inertial instability continuing to affect the anticyclonic shear side of the jet maintaining a 36 m/s wind speed. Bottom left (same as in top left, top right, and bottom left) at 2100 UTC on 22 April 2005 inertial instability leaving the plane of the cross section and jet core wind speed reduced to 30 m/s.

Figure 14. UWNMS simulation of Case 2 initialized with ECMWF data on 00 UTC 22 April 2005 showing the relationship between inertial instability and enhanced divergence associated with jet wind speed increase. Top left panel shows a cross section of wind speed (blue contours, 4 m/s) isosurface of inertial instability (brown shaded isosurface,-1.5 PVU) and convergence (red shading) divergence (blue shading) patterns at 2130 UTC 22 April 2005. As inertially unstable

air interacts with the anticyclonic shear side of the jet, the divergence is enhanced resulting in a tightening of the isotachs and increased wind speed. At 2030 UTC (top right panel, shading the same as in top left panel) wind speed is enhanced as inertial instability creates an area of increased divergence (blue shading). At 2130 UTC (bottom left panel, shading the same as in top left and top right panel) a continuation of enhanced divergence is evident as inertially unstable air continues to affect the anticyclonic shear side of the jet, resulting in a tightening of the isotachs. At 2200 UTC (bottom left panel, shading the same as in top left, top right, and bottom left panel) shows a continual interaction between inertial instability, enhanced divergence and a local wind speed maximum (inertial flare-up).

Figure 15. UWNMS simulation of Case 2 initialized with ECMWF data on 00 UTC 22 April 2005 showing the relationship between negative absolute vorticity, divergence, negative EPV and a tightening of the isotachs. Left panels show absolute vorticity, (blue shading is negative, red shading is positive), and divergence (white contours, interval 5 x 10^{-5} s^{-1}). Right panels show negative EPV (blue shading is negative, red shading is positive) and jet wind speeds (black contours, every 4 m/s). Top panels are at 2130 UTC on 22 April 2005. Middle panels are at 2330 UTC 22 April 2005. Bottom panels are at 0930 UTC 23 April 2005.

Figure 16. UWNMS simulation of Case 3 initialized at 00 UTC on 21 February 2011 showing relationship between inertial instability and jet wind speed increase (inertial flare-up). Top left panel shows a cross section of wind speed (dark blue contours, 3 m/s) and an isosurface of inertial instability (blue isosurface, -1.5 PVU) on 9300 UTC on 21 February 2011. No flare-ups are evident as inertial instability has not crossed the plane of the cross section. Top right panel (same as in top left panel) at 1500 UTC a 40 m/s jet wind speed is evident as inertial instability interacts with the anticyclonic shear side of the jet. Bottom left panel (same as in top left, top

right, and bottom left panels) at 1530 UTC another jet speed maximum is evident. Bottom right panel (same as in top left, top right, and bottom left) at 1800 UTC inertial instability no longer in the plane of the cross section and no inertial flare-ups are evident.

Figure 17. UWNMS simulation of Case 3 initialized with ECMWF data on 00 UTC 20 February 2011showing relationship between inertial instability and enhanced divergence associated with jet core wind speed increase in a horizontal map view at 13 km. The star indicates the location of Madison, WI. Top left panel (and all panels in this figure) shows a horizontal map at 13 km of wind speed (white contours, 4 m/s) isosurface of inertial instability (dark brown, -1.5 PVU) convergence (shaded in red) and divergence (shaded in blue) at 1400 UTC 21 February 2011. As inertially unstable air enhances the divergence in the jet, a distinctive tightening of the isotachs occurs. At 1400 UTC (top left panel) a 40 m/s inertial flare-up is evident as divergence is enhanced through interaction with inertial instability. At 1430 UTC (top right panel) a 52 m/s inertial flare-up is shown. At 1500 UTC (middle right panel) a 64 m/s jet core wind speed is shown. At 1530 UTC (middle right panel) a 64 m/s jet core wind speed is maintained through enhanced divergence. At this time note a new inertial flare-up at 44 m/s just to the west of the 64 m/s flare-up. At 1600 UTC (bottom left panel) the new inertial flare-up now at 52 m/s due to enhanced divergence from the anomalous inertial instability. At 2000 UTC (bottom right panel) a relaxed jet is shown with no notable inertial flare-ups as anomalous inertial instability is not in the horizontal plane of this plot.

Figure 18. UWNMS simulation of Case 3 initialized with ECMWF data on 00 UTC 21 February 2011 showing the relationship between negative absolute vorticity, divergence, negative EPV and a tightening of the isotachs. Left panels show absolute vorticity, (blue shading is negative, red shading is positive), and divergence (white contours, interval 5 x 10^{-5} s^{-1}). Right panels show

negative EPV (blue shading is negative, red shading is positive) and jet wind speeds (black contours, every 4 m/s). Top panels are at 1500 UTC on 21 February 2011. Middle panels are at 1900 UTC 21 February 2011. Bottom panels are at 1930 UTC 21 February 2011.

Figure 19. Transverse circulation in the vicinity of an idealized jet core. Dashed lines are U isotachs, dotted lines are V isotachs, and solid lines are streamlines of transverse circulation. Taken from Eliassen (1962).

Figure 20. Cross section of potential vorticity (10^{-6} sec^{-1} °K mb^{-1}). Taken from Shapiro (1974). Potential vorticity contours are similar to that of Fig. 5 (middle right panel) and Fig. 15 (middle right panel).

Figure 21. Cross section of potential vorticity (10^{-7} K s^{-1} mb^{-1}). Taken from Shapiro (1978). Note the potential vorticity contours are similar to Fig. 24 middle left panel.

Figure 22. Eulerian cross sections for Case 1 at 0330 UTC on 6 February 2008. Left panels show an isosurface of jet at 60 m/s and the black line shows where the cross section occurs along the jet. Right panels show negative EPV (red shadings is positive EPV and blue shadings is negative) and streamfunction (black contours). Black J indicative of jet max at 60 m/s. Black box reveals Sawyer-Eliassen circulation as described in text.

Figure 23. Eulerian cross sections for Case 2 at 0230 UTC on 22 April 2005. Left panels show an isosurface of jet at 40 m/s and the black line shows where the cross section occurs along the jet. Right panels show negative EPV (red shadings is positive EPV and blue shadings is negative) and streamfunction (black contours). Black J indicative of jet max of 40 m/s. Black box shows Sawyer-Eliassen circulation as described in text.

Figure 24. Eulerian cross sections for Case 3 at 1630 UTC on 21 February 2011. Left panels show an isosurface of jet at 50 m/s and the black line shows where the cross section occurs along the jet. Right panels show negative EPV (red shadings is positive EPV and blue shadings is negative) and streamfunction (black contours). Black J shows jet maximum at 50 m/s. Black box indicates Sawyer-Eliassen circulation as discussed in text.

Figure 25. UWNMS longitudinal sampling of meridional cross section across the length of the westerly jet from the west coast of the United States (top panel) to the east coast of the United States (bottom panel) for 6 February 2008 Case showing connection between negative EPV and STE. All panels show jet wind speeds (black contours, every 4 m/s), PV (red shading, PV values < 0, yellow shading, PV values at 0, blue shading, PV values < 0, isosurface of EPV (dark blue isosurface, -3 PVU). Top row (left panel) is at 1200 UTC on 5 February 2008. Top row (right panel) is at 1430 UTC on 5 February 2008. Second row (left panel) is at 1500 UTC on 5 February 2008. Second row (right panel) is at 1800 UTC on 5 February 2008. Third row (left panel) is at 2200 UTC on 5 February 2008. Third row (left panel) is at 0030 UTC on 6 February 2008. Bottom row (left panel) is at 0230 UTC 6 February 2008. Bottom row (right panel) is at 0600 UTC on 6 February 2008.

Figure 26. UWNMS longitudinal sampling of meridional cross section across the length of the westerly jet from the west coast of the United States (top panel) to the east coast of the United States (bottom panel) for 22 April 2005 Case showing connection between negative EPV and STE with the use of GEOS ozone. Top row (left panel) shows jet wind speeds (black contours, every 4 m/s), isosurface of EPV (-2 PVU), and ozone (red shading, high levels of ozone, yellow intermediate levels, and blue low levels) at 1530 UTC on 22 April 2005. Top row (right panel), same as in top row (left panel) except for PV (black contours, every 1 PVU), and no jet wind

speed. Second row (left panel) same as in top row (left panel) except time is at 1600 UTC on 22 April 2005. Second row (right panel) same as in top row (right panel) except time is same as second row (left panel). Third row (left panel) same as in second row (left panel) except time is at 0130 UTC on 23 April 2005. Third row (right panel) same as in second row (right panel) except time is same as in third row (left panel). Bottom row (left panel) same as in third row (left panel) except time is at1530 UTC 23 April 2005. Bottom row (right panel) same as in third row (right panel) except time is the same as bottom row (left panel).

Figure 27. UWNMS longitudinal sampling of meridional cross section across the length of the westerly jet from the west coast of the United States (top panel) to the east coast of the United States (bottom panel) for 21 February 2011 Case showing connection between negative EPV and STE. All panels show jet wind speeds (black contours, every 4 m/s), PV (red shading, PV values < 0, yellow shading, PV values at 0, blue shading, PV values <0, isosurface of EPV (dark blue isosurface, -3 PVU). Top row (left panel) is at 0830 UTC 20 February 2011. Top row (right panel) is at 1500 UTC 20 February 2011. Second row (left panel) is at 1730 UTC on 20 February 2011. Second row (right panel) is at 2030 UTC on 20 February 2011. Third row (left panel) is at 0930 UTC on 21 February 2011. Third row (right panel) is at 1330 UTC on 21 February 2011. Bottom row (only panel) is at 2330 UTC on 21 February 2011.

Figure 28. The Moderate Resolution Imaging Spectroradiometer (MODIS) on NASA's Terra satellite acquired this natural-color image on 2 September 2011 (top left panel). CIMSS track of Talas moving over Japan (top right panel). This color-coded image shows rainfall totals from Tropical Storm Talas from 30 August to 5 September 2011(bottom left panel).The heaviest rainfall, more than 14 inches, appears in dark blue. The lightest rainfall, less than 2 inches appears in light green. Areas with only a trace of rain appear pale yellow (bottom left panel). On

31 August 2011 at 7:21 p.m. EDT, TRMM captured several intense thunderstorms in Talas' northern edge- that were about 10 km high. Yellow and green indicate rainfall occurring between .78 to 1.57 inches per hour. Dark red areas are considered heavy rainfall, as much as 2 inches of rain per hour highlighted by the cross sectional line A to B (bottom right panel).

Figure 29. UWNMS model output using 2.5 degree ECMWF reanalysis and a 16 km model top showing (top left panel) 1 September 1530Z showing theta-e (black contours, interval 4K), the .4 m/s vertical velocity isosurface in purple, EPV values in PVU shaded showing positive EPV in red, moderate values in orange, and negative values in blue, and surface pressure contours (yellow contours, interval 4 hPa). (Top right panel) 1 September 2100Z showing (shading same as in top left panel), EPV (black contours, interval 1 PVU), the EPV-2 PVU isosurface in red, and the 45 m/s U component of the wind isosurface in green. (Bottom left panel) 1 September 130Z showing sea level pressure (blue contours, interval 4 hPa). (Bottom right panel) shows 1 September 2011 1530Z (same as in bottom left panel).

Figure 30. UWNMS simulation of typhoon Talas using 2.5 degree ECMWF data with a 25 km model top at 1 September 2011 showing the relationship between inertial instability, vertical motion, STE and sea level pressure. The top left panel shows an east-west cross section through Talas just to the south of Japan at 1530 UTC with theta-e (black contours, 5 K), vertical motion (pink isosurface, 4 cm/s), negative EPV (yellow isosurface, -2 PVU), and potential vorticity, (red shading, high PV stratospheric air). Top right panel at 2100 UTC same as in top left panel except PV contours (blue, 1 PVU) are shown instead of theta-e contours. Bottom left panel shows surface pressure contours (blue, 4 hPa) at 130 UTC. Bottom right panel same as in bottom left panel except time is at 1530 UTC.

Figure 31. UWNMS simulation of hurricane Sandy initialized with GFS data and a 16 km model top showing a possible STE mechanism around the periphery of the storm and associated surface pressure at (top panels) 0000 UTC on the 304th day (middle panels) 0600 UTC on the 304th day and at (bottom panels) 12Z on the 306th day. Color shadings for all panels are: red (PV < 3 PVU) blue (PV > 3 PVU), white contours (PV), blue contours (surface pressure (contoured every 4 hPa).

Figure 32. Panel shows UWNMS simulation of Typhoon Roke with a 16 km and a 25 km model top initialized with 2.5 degree ECMWF data showing the possible relationship between inertial instability and STE locally within the storm and around the periphery of the storm. Both panels are an east-west cross section through Roke on the southernmost coast of Japan. Left panel shows Roke with a 16 km model top. Right panel shows Roke with a 25 km model top. Color shading for left panel: dark blue shading (negative EPV, -2 PVU), dark red shading (EPV, < 0 PVU) dark blue contours, (EPV, contoured every 1 PVU). Color shading for right panel: same as in left except black contours (EPV contoured every 1 PVU).

Figure 33. Schematic of the overall dynamics of an idealized tropical cyclone as negative EPV interacts with the base of the stratosphere.

Abstract

A new dynamical relationship is found between regions of inertial instability (negative equivalent potential vorticity, EPV) and stratosphere – troposphere exchange (STE) near midlatitude westerly jets. Convection along a cold front can lead to enhancement of inertial instability on the anticyclonic shear side of the jet in the upper troposphere and lower stratosphere (UTLS). Inertial acceleration leads to an enhanced meridional circulation around the jet, featuring ascent into the negative EPV region over the precipitation maximum, and a mixed UTLS layer circulating poleward and downward back into the troposphere. This 50 km mesoscale enhancement creates a distinctive mixing and transport mechanism for STE, as well as quasi-stationary banded precipitation.

The focal region is the upper Midwest of the United States during winter and spring. Three banded snow events were selected for diagnosis, using analyses from the National Centers for Environmental Prediction Eta model, together with higher resolution simulations with the University of Wisconsin Nonhydrostatic Modeling System (UWNMS). In these cases the surface low was located poleward of a jet exit or equatorward of a jet entrance. A shallow mixed layer with low EPV, high turbulent kinetic energy, and low Richardson number typically emanates from the region of inertial instability in the UTLS on the upward and equatorward side of the jet. Trajectories illustrate the connection between negative EPV in convection upstream and negative EPV near the jet. It is shown that negative EPV anomalies lead to local jet accelerations or "inertial flare-ups". These cases depict a unique relationship between STE transport pathways and inertial instability. Additional analysis includes relating this idea to tropical storms. Initial analysis of typhoons Roke and Talas (2011) and Hurricane Sandy (2012)

suggest that inertial instability within these tropical systems plays a role in local and peripheral STE.

1. Introduction

1.1. Motivation

Mixing of stratospheric and tropospheric air is poorly understood in terms of the meteorological processes that cause the mixing (e.g., Stohl et. al. 2003). In examining simulations of quasi-stationary, banded precipitation events in the upper Midwest with the UWNMS, unexpected regions of negative equivalent potential vorticity (EPV) were found near the tropopause on the anticyclonic shear side of the jet. Further exploration led to the serendipitous discovery of inertially unstable regions in the upper troposphere / lower stratosphere (UTLS) that are intimately related to accelerated meridional circulations around the jet, where thin layers of turbulently mixed air in UTLS spiral eastward and downward back into the troposphere (i.e., with negative vorticity in the x-direction), contributing to stratosphere – troposphere exchange (STE).

This mesoscale STE concept in midlatitudes can be visualized on a global scale as the cumulative effect of deep tropical convection penetrating the stratosphere and large scale ascent. The extratropical "pump" (McIntyre et. al., 1990) driven by large scale waves, blocking anticyclones, tropopause folds, and local midlatitude areas of inertial instability transports this air toward the poles, where large scale subsidence and STE occurs. Figure 1 summarizes the dynamics associated with this global scale view of STE. In this work, however, the main focus will be on the local mesoscale STE manifestations within developing midlatitude cyclones.

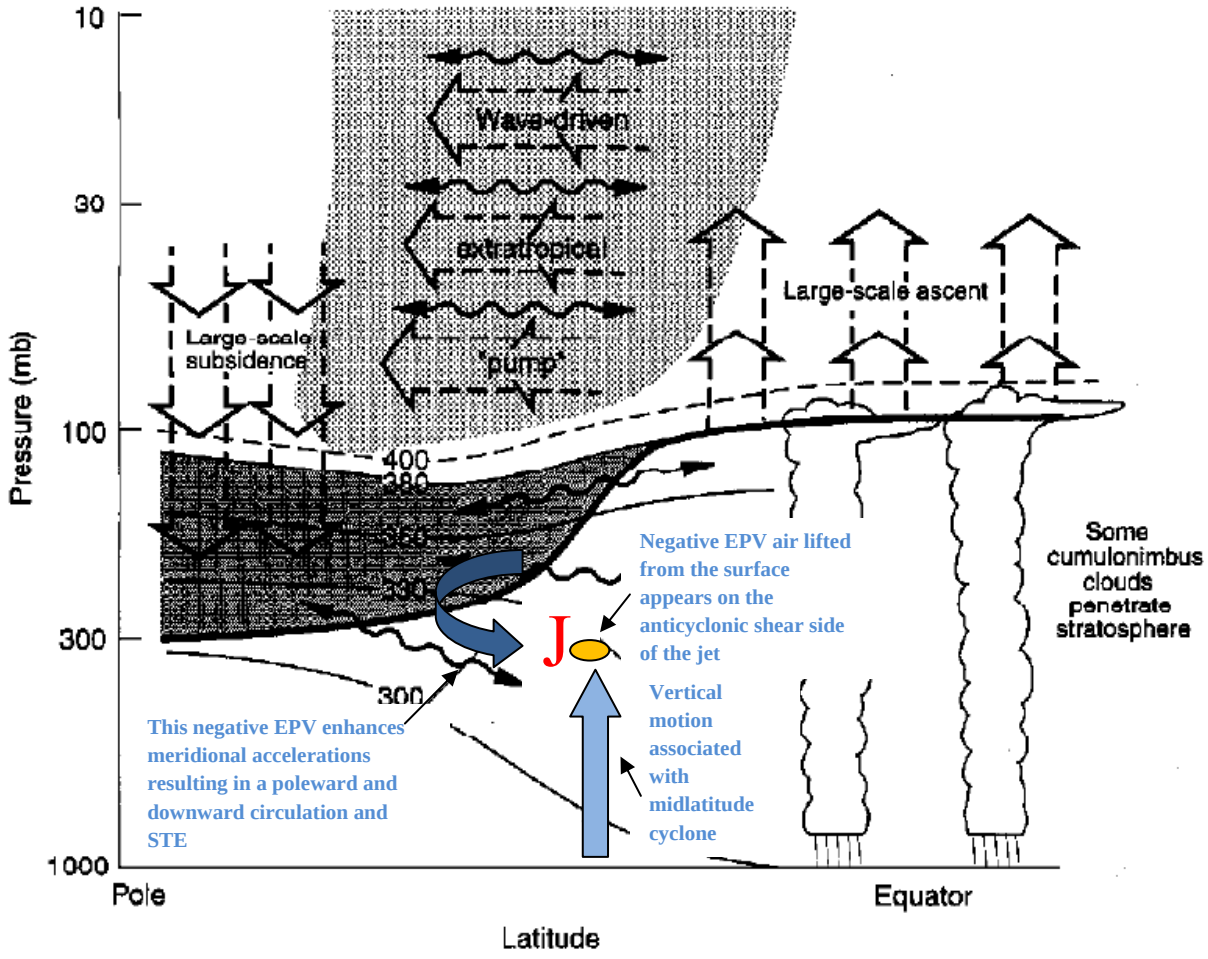

Figure 1. Global dynamical aspects of STE. The tropopause is shown with a thick black line. The heavily shaded region is the lowermost stratosphere. Light shading shows area of wave induced forcing. The wavy double headed arrows show meridional transport by eddy motions. The blue filled arrow shows vertical motion associated with midlatitude cyclones. The orange filled circle shows negative EPV air on the anticyclonic shear side of the jet that was lifted in the vertical through latent heat release. The red J shows an idealized position of the midlatitude westerly jet. The dark blue curved arrow shows a subsequent poleward and downward STE mechanism brought about by enhanced meridional circulations due to this anomalous area of inertial instability on the anticyclonic shear side of the westerly jet.

1.2. Connection with previous work

This section relates inertial instability to negative EPV and introduces the PV tendency equation. Inertial instability occurs when angular momentum decreases radially outward, such as in flow between two rotating cylinders (Rayleigh, 1916; Taylor, 1923). When this criterion for instability is met, parcels accelerate and rearrange themselves, tending to stabilize the angular momentum profile. Consideration of radial parcel displacement δs in an axisymmetric vortex yields the oscillator equation

$$\frac{\partial^2}{\partial t^2}\delta s = -f\,(f + \zeta)\,\delta s \qquad (1a)$$

with acceleration occurring (inertial instability) if the coefficient is negative:

$$f\,(f + \zeta) < 0\,, \qquad (1b)$$

where $f = 2\,\Omega \sin\varphi$ and $\zeta = \partial v/\partial x - \partial u/\partial y$ is relative vorticity (Eliassen and Kleinschmidt, 1957; Holton, 2006). In the case of rotation about the earth's axis, angular momentum per unit mass may be taken as $M = r\,u + r^2\,\Omega$, where $r = a \cos\varphi$, a is earth radius, u is zonal flow, and Ω is the angular frequency of the earth's rotation. Inviscid inertial instability will occur in sufficiently strong anticyclonic relative vorticity, which can occur on the equatorward flank of a westerly jet Inertial instability implies a divergence / convergence pattern associated with parcel acceleration and deceleration at the edges of inertially unstable regions, which in turn implies 3D circulations at smaller scales and enhanced turbulence and mixing (O'Sullivan and Hitchman, 1992).

This criterion can be related to Ertel's potential vorticity (PV) and the gradient of angular momentum on an isentropic surface

$$f\ PV = \frac{1}{\rho}\frac{\partial \theta}{\partial z} f\,(f + \zeta) = -\frac{1}{r}\nabla_{\theta} M < 0 \quad , \qquad (2)$$

(e.g., Hoskins et al., 1985; Hitchman and Leovy, 1986). Inertial instability occurs when there is anomalously-signed PV for a given hemisphere, or anomalous absolute vorticity (first relation in (2)). It occurs when angular momentum increases toward the rotation axis (second relation in (2)). This criterion for instability is easier to satisfy near the equator where f is small and angular momentum surfaces are parallel to the surface of the earth. In the Northern Hemisphere, where f > 0, the flow is inertially unstable if the absolute vorticity of the basic flow is negative: $f + \zeta < 0$.

Inertial or symmetric instability is important for tropical boundary layer flows (e.g., Krishnamurti and Wong 1979; Reverdin and Sommeria 1983; Stout and Young 1983; Tomas and Webster 1997), planetary scale "pancake structures" in the subtropical middle atmosphere (Hitchman et al. 1987; Hayashi et al, 2002), midlatitude cyclogenesis and jet streams (Sawyer 1949), precipitation bands in midlatitude cyclones (Bennetts and Hoskins 1979; Knox 2003), and on the edges of anticyclones (Stevens and Ciesielski 1986; Knox 1997).

Let us examine the implications of negative equivalent potential vorticity (EPV) in the Northern Hemisphere:

$$EPV = \frac{1}{\rho}\frac{\partial \theta_e}{\partial z}(f + \zeta) < 0 \quad , \qquad (3a)$$

where

$$\theta_e = \theta\ exp\left(\frac{Lw_s}{c_p T}\right) \quad , \qquad (3b)$$

$L = 2.5 \times 10^{-6}$ J kg^{-1} is the latent heat of condensation, w_s is saturation water vapor mixing ratio, $C_p = 1005$ J kg^{-1} K^{-1} is specific heat at constant pressure, and T is temperature. θ_e allows for energy conservation between vapor phase change and internal energy. A reduction of 12 g/kg

due to precipitation in an updraft can cause θ to increase by ~32 K. Moisture modifies the static stability, especially in the boundary layer, therefore the criterion $\partial\theta_e/\partial z < 0$ is the most useful for evaluating static instability. One may see that EPV is negative if the atmosphere is either moist statically unstable or if it is inertially unstable. Air that is moist statically unstable that is brought by convection to the base of the stratosphere will be statically stable but it may still have negative EPV, implying that upstream convective instability can lead to downstream inertial instability.

In order to understand the origin of the negative EPV anomalies it is important to consider the PV tendency equation. Following Pomroy and Thorpe (2000) and considering the dominant vertical component and ignoring frictional effects:

$$\frac{d\,PV}{dt} = \frac{1}{\rho}\left(\zeta\ \frac{\partial}{\partial z}\left(\frac{d\theta}{dt}\right)\right) \quad . \tag{4}$$

In warm conveyor belts and thunderstorms latent heating dominates. Due to turbulent mixing and mechanical processes PV will not be conserved. Equation (4) allows us to understand how PV can change along the path. In the UTLS there is not much moisture, so EPV is quantitatively nearly the same as PV.

It has been shown that STE is highly episodic, and associated with strong mesoscale perturbations of the tropopause (Appenzeller and Davies, 1992). Exchange occurs when the tropopause is distorted by latitudinal displacements. These distortions are characterized by sheets of high PV air which extend equatorward. Past studies have concluded that strong baroclinic folding events are a major cause of STE in the midlatitudes (Price and Vaughan, 1993). Quantities such as static stability and transience made irreversible by Rossby wave breaking are

vital in determining the amount of stratospheric air that enters the troposphere. Ucellini et al. (1985) showed through modeling and observations that rapidly growing events play a particularly important role in STE in the midlatitudes.

Knox (2003) postulated that intense extratropical cyclones may exhibit inertial instability. While studying an elevated convection event which occurred in the upper Midwest during 14 July 1995 he discovered that elongated bands of light rain coincided with a narrow region of negative PV. UWNMS simulations of the event indicated a quadrapole checkerboard pattern in the vertical motion field, signifying inertial instability. It was found that the rising motions caused by the instability were large enough to cause condensation and elevated convection, thus producing the banded radar echoes.

Schumacher et al. (2010) simulated quasi-stationary precipitation bands and found that they occurred in an environment with a well-mixed baroclinic boundary layer, positive convective available potential energy, and widespread negative PV. It was shown that ascent caused by frontogenesis and banded moist convection produced narrow regions of negative absolute vorticity caused by the upward transport of low momentum air. This thesis revisits this mechanism as a cause of negative PV. Convective bands initiated within the ascending branch of the secondary circulation were associated with elevated and near-surface frontogenesis. Their work is explicit about the presence of negative PV, and inertial instabilities on the poleward side of the surface cyclone and anticyclonic side of the jet. Their primary focus, however, was on the cause of the precipitation maximum and to compare simulated versus observed convective bands in and around complex terrain over Colorado and Utah.

Lang (2011) discovered that the interaction of surface-based convection and the static stability of the upper troposphere influences the development of lower stratospheric fronts. The intensification of the upper level front takes place as convectively generated latent heat release associated with a surface frontal zone reconfigures the potential temperature field in the upper troposphere, causing the stability near the base of the stratosphere to decrease. Most similarly to the research presented here, Lang (2011) showed that convective ascent leads to diabatically reduced PV and reduced static stability near the tropopause on the anticyclonic shear side of the jet.

Most recently, work by Schemm et al. (2013), studied negative EPV anomalies in warm conveyor belts (WCB) in idealized moist baroclinic wave simulations. They found that if the WCB air parcels are above the level of maximum latent heating along the vertical path, then lower PV values result. Due to these low PV values in the WCB outflow, the WCBs create negative PV anomalies in their outflow at upper tropospheric levels. Reduced PV in the upper level ridge of the moist baroclinic wave produces an amplified upper level ridge and intensified anticyclonic circulation, contributing to enhanced downstream cyclogenesis.

In this thesis a dynamical mechanism for STE near midlatitude cyclones involving inertial instability at the base of the stratosphere is the focal point of discussion. Observational data and simulations with the UWNMS are presented for three selected cases of pronounced snowbands: quasi-stationary elongated and protracted precipitation features common in the upper Midwest during winter and spring (sections 2 and 3). There is a relationship among negative EPV, meridional circulation around the jet, upstream convection, and synoptic storm features. A previously undiscovered STE mechanism is diagnosed in which local inertial instability is intrinsically involved in the poleward and downward circulation around midlatitude

westerly jets (section 4). Additional model diagnosis shows acceleration of the jet core wind speeds (which will be referred to as "inertial flare-ups"), as low EPV ascends through the troposphere, becomes increasingly negative, and travels to the anticyclonic shear side of the jet (section 5). A unique Eulerian and Lagrangian point of view will analyze cross sections of streamfunction, negative EPV, and isotachs to better understand inertial instability induced STE around jets (section 6). Additional analysis will include applying inertial instability induced STE concepts to Typhoons Talas and Roke (2011) and Hurricane Sandy (2012) to better understand how the stratosphere interacts with the troposphere in tropical-subtropical environments (section 7).

2. Methods and Analysis

The following dynamical quantities were particularly useful in diagnosing STE associated with inertial instability: moist potential vorticity (MPV), moist static stability, relative vorticity, turbulent kinetic energy, Richardson number, and horizontal divergence.

2.1. Dynamical diagnostic variables

It will be seen that air found on the equatorward side of the westerly jet often originates in the moist boundary layer of a subtropical air mass. In considering how this air facilitates STE it is important to include water vapor phase changes in defining potential temperature used in calculating PV. Equivalent potential temperature, θ_e (Holton 2004), is used in evaluating PV in (2), defining moist PV (MPV). Since convective updrafts occur where $\partial\theta_e/\partial z < 0$, air with negative MPV can be created and transported into the upper troposphere, where dehydration causes MPV to asymptote to PV, preserving its negative value, and implying the possibility of

inertial instability. MPV dynamics are a vital contributor in assessing conditions conducive to conditional symmetric stability (CSI). The concept of MPV has been widely used in studies of CSI in baroclinic systems since CSI was first introduced as a potential mechanism for the generation of frontal rainbands (Bennetts and Hoskins, 1979; Emannuel, 1979; Montgomery and Farrell, 1991; Schumacher and Schultz, 2001; Schultz and Knox, 2007). MPV has proven useful in diagnosing squall lines (Zhang and Cho, 1991), extratropical cyclones (Cao and Cho, 1995; Cao and Zhang, 2004; Brennan et al., 2007), convective snowstorms (Halcomb and Market, 2003), and enhancing our understanding the dynamics of the UTLS (Hoskins et al., 1985; Morgan et al., 1998).

Turbulent kinetic energy per unit mass ($\varepsilon \sim m^2/s^2$) is a measure of the intensity of turbulence and is defined as

$$\varepsilon = \frac{1}{2}\left(\overline{u'^2} + \overline{v'^2} + \overline{w'^2}\right), \tag{5}$$

where the overbar indicates time and space averaging of the turbulent eddy variances. The UWNMS contains a prognostic equation for TKE, including advection, buoyancy generation, shear generation, and turbulent dissipation.

TKE and Ri are related by the mechanical generation of turbulence by wind shear and the buoyant generation of turbulence that can occur for small Ri. The ratio of the mechanical generation by wind shear to the buoyancy production or inhibition by static stability defines the dimensionless Richardson number. Ri can be approximated by the vertical gradients of wind and virtual potential temperature

$$\mathrm{Ri} = \frac{\frac{g}{\theta}\frac{\partial \theta}{\partial z}}{\left(\frac{\partial u}{\partial z}\right)^2 + \left(\frac{\partial v}{\partial z}\right)^2}, \tag{6}$$

where the term in the numerator is equivalent to the square of the Brunt V*äisälä* frequency. Turbulent flows usually stay turbulent, even for Ri numbers as large as 1.0 (inertial instability). The flow is dynamically unstable for flows with Ri < 0.25 (Kelvin-Helmholz instability). It will be shown that low Ri coincides with a shallow layer of notable TKE in the UTLS. It will be argued that inertial instability facilitates poleward acceleration of a shallow, turbulent layer of air that is composed of mixed stratospheric and tropospheric air, which wraps poleward and downward back into the troposphere

2.2 Case Selection

The following three cases were initially chosen for similarities in banded precipitation. However, as our investigation progressed, inertial instability and STE became a primary focus. During the events of 6 February 2008 and 22 April 2005, phenomena of interest were located over south-central Wisconsin and northern Illinois. During the event of 20-21 February 2011 inertially-accelerated STE occurred over south-central Minnesota. Each of the three cases have clear similarities with respect to their jet dynamics and STE mechanisms. The first case exhibits a stronger, more well-defined inertial flare-up, while cases two and three feature complex arrays of inertial flare-ups that evolve and dissipate over time, with the passing of each negative EPV anomaly. Each of the simulations was initialized ~24 hours before the phenomena of interest began. Vis5D was used to illuminate 3D flow features and trajectories which connect upstream surface instabilities with negative EPV anomalies in the UTLS equatorward of the jet.

The selected case studies represent a range of midlatitude systems in which the existence of STE and quasi-stationary banded precipitation during winter and spring is the dynamical focal point. In all three cases the surface low is to the east of a stratospheric PV maximum. The cases

illustrate that inertial instability-facilitated STE can occur when the surface low is equatorward of the jet entrance region (Case 1), between two jets, i.e., equatorward of one jet entrance and poleward of the other jet exit (Case 2), or when the surface low is poleward of the jet exit region (Case 3). The details of each case exhibit an interesting range of variation, with the positioning of jets and diverse convective initiation.

The most destructive of the three cases is a mid-winter scenario with a digging trough aloft that trapped 2000 vehicles in deep snow on I-90 in southern Wisconsin and spawned deadly tornadoes along the cold front during 6-8 February 2008. An impressive tropopause jet with winds in excess of 70 m/s, with equatorward-flanking EPV values of less than -3 PVU, dominated the UTLS over the Midwest. In sharp contrast, the early spring storm of 22 April 2005 that invaded central Wisconsin occurred between moderate subpolar and subtropical jets, ahead of an isolated PV streamer. Even though this case featured a 30 m/s jet core wind speed maxima, the negative EPV values still exceeded -2 PVU near 13 km. Another interesting case occurred over southern Minnesota during 22 February 2011, similarly between two jets, but with the upstream jet being stronger. In this event, the jet formed and strengthened as it interacted with convectively-injected negative EPV anomalies that ascended on the anticyclonic shear side of the westerly jet. Several inertial flare-ups developed and expanded after exposure to negative EPV anomalies. The value of EPV was less than -2 PVU on the equatorward side of the jet in the multiple flare-ups of case three.

2.3. The University of Wisconsin Non-Hydrostatic Model (UWNMS)

Each of the cases is modeled with the UWNMS (Tripoli 1992a; 1992b; Pokrandt et al. 1996; Jascourt 1997; Mecikalski and Tripoli 1997; Avissar et al. 1998), initialized with 2.5° European Centre for Medium-range Weather Forecasts (ECMWF) data. The specified UWNMS resolution for all cases is 20 km x 20 km x 300 m, with a grid volume of 152 x 152 x 60 points. The top of the model is set to 18 km. We use Vis5D to view the 3D structure of each midlatitude cyclone and the associated dynamics in the UWNMS. Supplemental synoptic scale diagnostics were made using 80 km resolution Eta model reanalysis from the National Centers for Environmental Prediction (NCEP) using the GEneral Meteorological PAcKage (GEMPAK).

The horizontal length scale of the model domain for each midlatitude case spans 3020 km. The center point of the model domain is 95°W, 40°N. The bottom left corner is at 26.4°N, 112.8°W. The bottom right corner is at 26.4°N, 77.15°W. The top right corner is at 53.6°N, 77.15°W. The top left corner is at 53.6°N, 112.8°W.

3. UWNMS Case Studies of Inertial Instability and STE

3.1. Case 1, 6 February 2008 – Surface Low Near Strong Jet Entrance Region

An interesting synoptic situation developed over the Central Plains of the United States during 6-8 February 2008, as a severe weather outbreak spawned intense tornadoes throughout the Mississippi and Ohio Valleys. Heavy snow bands stranded approximately 2000 vehicles for 24 hours on I-90 in southwestern Wisconsin. Figure 2 shows an Eta model overview of the

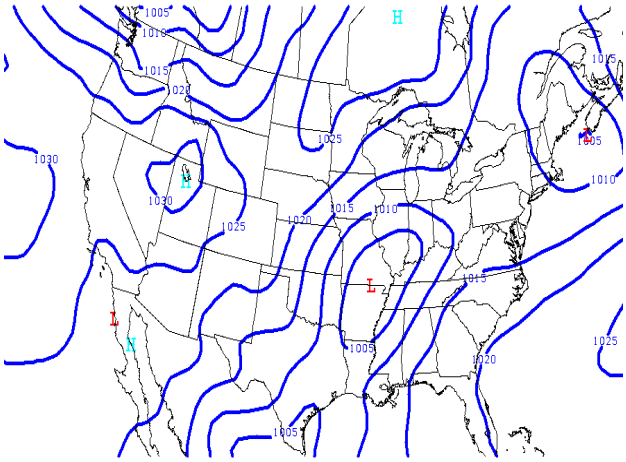
H
L
L
1005
1010
1015
1020
1025
1030

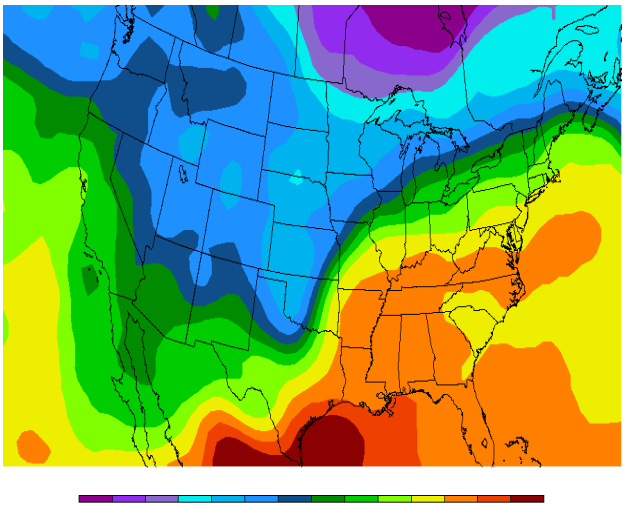
-18 -15 -12 -9 -6 -3 0 3 6 9 12 15 18

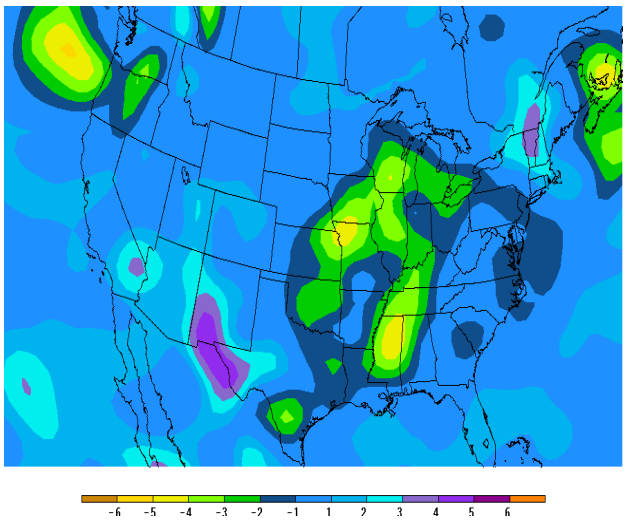
-6 -5 -4 -3 -2 -1 1 2 3 4 5 6

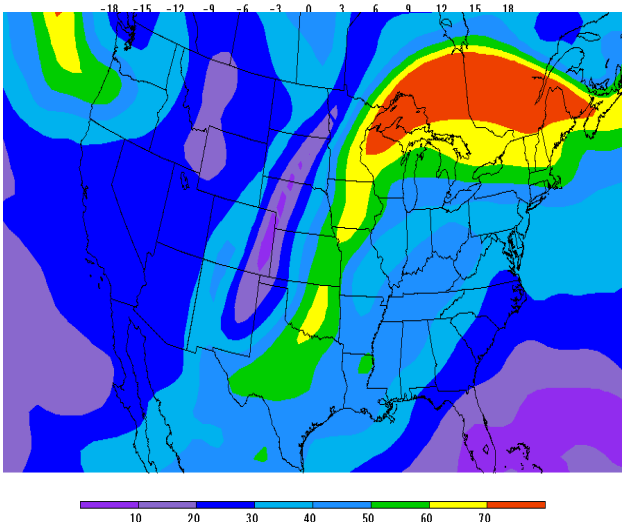
10 20 30 40 50 60 70

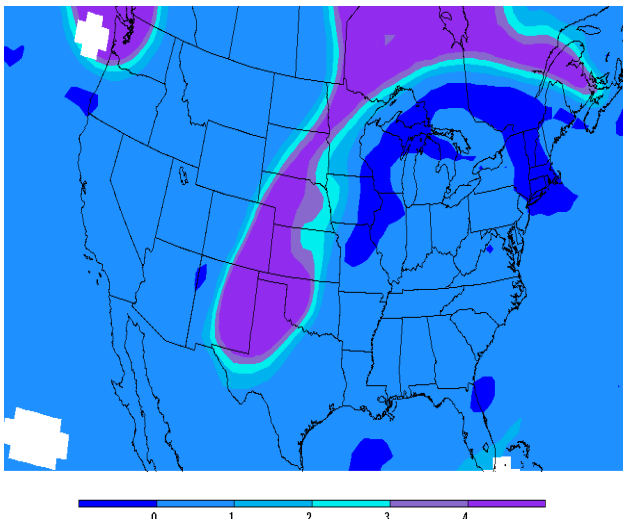
0 1 2 3 4

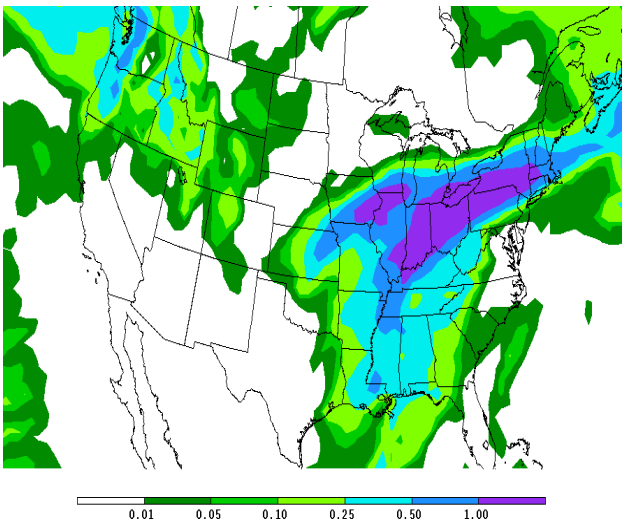
0.01 0.05 0.10 0.25 0.50 1.00

Figure 2. Synoptic setting for Case 1, as seen in the NCEP eta model analysis for 0000 UT 6 February 2008: top left panel) sea level pressure (blue contours, interval 4 hPa), top right panel) 850 hPa temperature (color bar, interval 3^{o}C), middle left panel) 700 hPa vertical pressure velocity (color bar, interval 1 Pa/s), middle right panel) 300 hPa wind (color bar, interval 10 m/s), bottom left panel) 300-250 hPa EPV (color bar, interval 1 PVU), and bottom right panel) 24-hr accumulated precipitation during 0000 UT 6 February – 0000 UT 7 February 2008 (in inches, color bar). Note the region of rising motion equatorward of the jet over Illinois.

synoptic scale dynamics associated with the storm at 0000 UT 6 February 2008. Figure 2 (top left panel) shows the surface low pressure system which strengthened while progressing through central Illinois and northern Ohio. During its migration northeastward over Ohio, quasi-stationary snowbands matured and persisted in southwestern Wisconsin and northern Illinois, with a characteristic east-west arc-shaped linear configuration, and snowfall in the range 12-18" (exceeding 1" water equivalent in Fig. 2 (bottom right panel)). During this time quasi-stationary features lingered, dissipated and redeveloped over the same domain into the afternoon and overnight hours of 6-7 February. In concert with this, areas of convective ascent (green region over Missouri and Indiana in Fig. 3 (top left and top right panel)) lifted air with negative EPV from the surface to the base of the stratosphere, inducing a distinctive STE mechanism.

A sharp, digging trough associated with a pronounced southward extension of high polar PV toward Texas (Fig. 2 (bottom left panel)) was accompanied by a strong jet with speeds in excess of 70 m/s from Wisconsin arching into Eastern Canada (Fig. 2 (middle right panel)). On the equatorward side of this jet an area of strong inertial instability is apparent, as evidenced by the negative EPV anomalies (dark blue) over Illinois at the base of the stratosphere in the 300-250 hPa layer (Fig. 2 (bottom left panel)).

A higher-resolution view is seen in the UWNMS simulation in Fig. 3, which emphasizes a northwest-southeast section from central Minnesota to central Ohio. Figure 3 (top left, top

right, and middle left panels) show how strong updrafts transport inertially unstable air from the surface to the anticyclonic shear side of the jet.

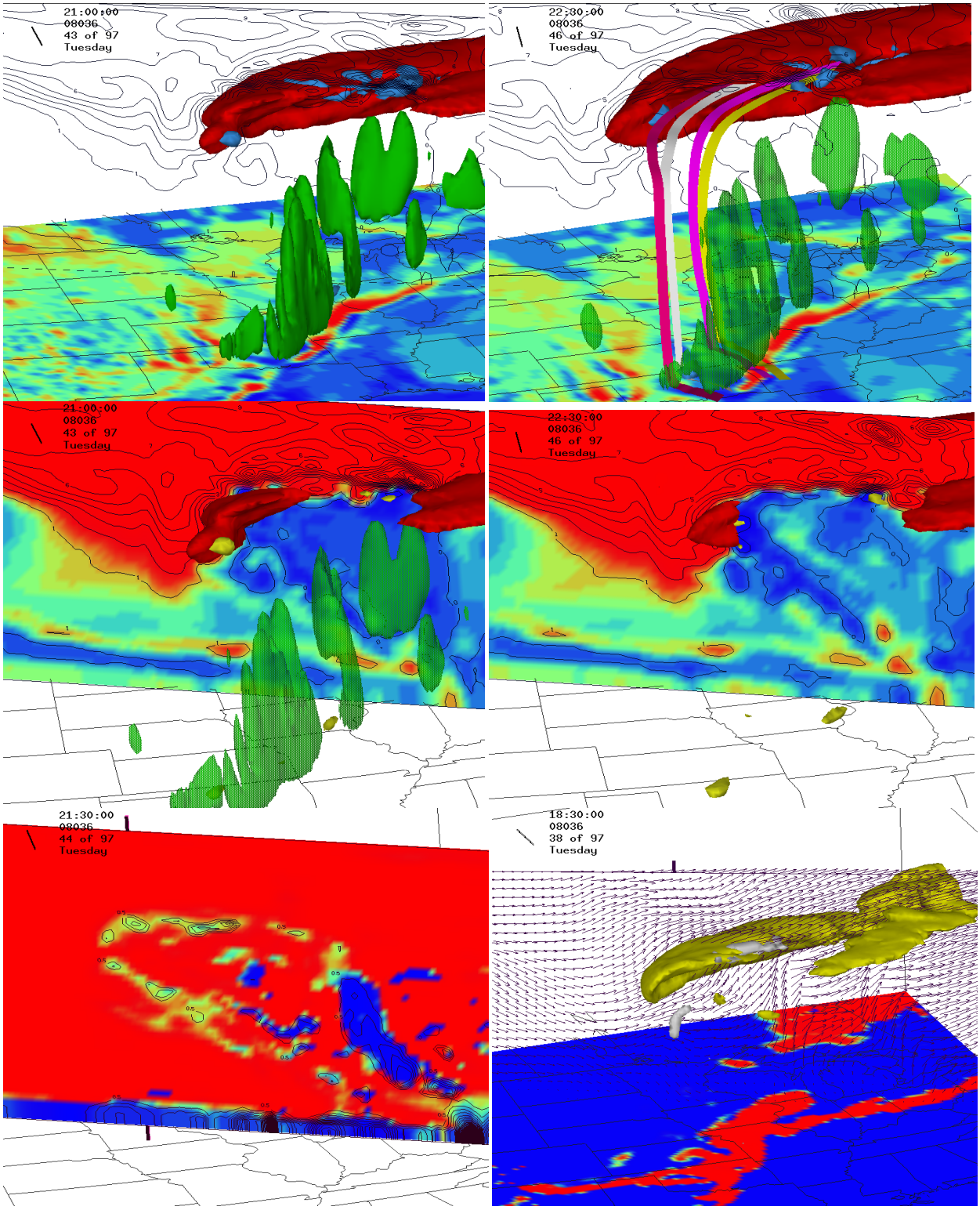

Figure 3. UWNMS simulation of Case 1, initialized with ECWMF data on 0000 UTC 5 February 2008, at 2100 UTC (left panels) and 2230 UT 6 February 2008 (right panels), showing the relationship among convection along the cold front, negative EPV, and jet location. Top left and top right panels show sections of EPV (black contours, interval 1 PVU), a blue inertial instability isosurface of -2 PVU, a red jet isosurface of 60 m/s, and a green updraft isosurface of 4 cm/s. Top left and top right panels also show EPV at the surface, where red shows negative EPV and blue shows EPV larger than 1 PVU. The ribbons in top right panel show trajectories arriving at the region of anomalous EPV in the upper troposphere originating 14 hours earlier. Middle right and left panels also show the red speed isosurface of 60 m/s, while details of EPV (black contours, interval 1 PVU) are highlighted in color, ranging from low values in blue to high values in red. Bottom left panel shows the distribution of TKE (black contours, interval 0.5 m^2/s^2) and Ri in color (blue < 0.25, red > 1). Bottom right panel shows the meridional circulation in the section (arrows), regions of negative EPV (white), a green jet isosurface of 30 m/s, and 24 hr average precipitable water (red exceeds 0.8 kg/m^2).

These regions of extremely negative EPV, which are observed at the base of the stratosphere over south-central Wisconsin, are conducive to slantwise convection, symmetric instability, and banded precipitation. Schumacher and Schultz (2001) found that inertially unstable conditions are common in the subtropical troposphere near 250 hPa. Figure 3 (top left and top right panels) highlight regions of negative EPV values exceeding -3 PVU at heights near 11 km on the anticyclonic shear side of the jet. Anomalous areas of negative EPV are embedded on the equatorward side of the jet. In animations of this structure (not shown) it is apparent that the jet strengthens locally immediately poleward of the negative EPV regions.

The negative EPV air found equatorward of the jet initially resided near the surface and was quickly accelerated through the depth of the troposphere as it was transported to the base of the stratosphere via updrafts exceeding 4 cm/s. Back trajectories in Fig. 3 (top right panel) reveal the origin of the negative EPV anomalies as they commenced near the 900 hPa level and became increasingly more negative while being lifted to the tropopause. As Fig. 3 (top left, top

right and middle left panels) reveals, the vertical motion plumes deposited negative EPV air near 11-13 km on the anticyclonic shear side of the jet. These negative moist PV structures owe their existence to diabatic heating in the boundary layer of the cold front to the southeast of the region of interest. When negative moist PV is brought upward from low levels by the vertical motion fields, inertial flare-ups occur (section 5). As the negative EPV sections appear on the upward and equatorward side of the jet, a distinctive tightening of the isotachs occurs. This tightening is indicative of an increase in wind speeds and suggests a possible strengthening mechanism involving negative moist PV air embedding itself in the upward and equatorward quadrant of midlatitude jets.

Inertial flare-ups are closely related to STE. As the surface frontal zone associated with the mid-latitude cyclone forms over the affected area, PV anomalies can form due to diabatic processes associated with surface cooling or latent heat release in regions of ascent (Morgan et. al. 1997). In convection embedded in the warm upglide sector, a latent heating maximum can generate negative PV through vortex shrinking (Joos and Wernli 2012). These negative PV extrema are dispersed vertically and create inertial flare-ups. As an inertial flare-up intensifies, air wraps poleward then downward and equatorward around the newly formed wind speed maximum. This circulation pulls air that had previously resided in the stratosphere equatorward into the troposphere. Fig. 3 (top left, middle left and middle right panels) reveal this circulation through contours of PV. The PV contours wrap themselves equatorward around the inertial flare-up, pushing high PV air deep in the troposphere. Air that was once stratospheric in origin is now mixed into the troposphere, highlighting a previously unrealized STE mechanism.

Inertial flare-ups can be analyzed using back trajectories to simulate the origin and path of the moist PV structures (Fig. 3 (top right panel)). The negative EPV originally begins near the surface with values around 0 PVU. As the moist PV rises in the vertical it becomes increasing more negative as values reach as low as -3 PVU on the upward and equatorward side of the polar jet. As this inertially unstable air interacts with the jet, an increase in wind speed occurs. Note that the jet maximum which intersects the section in Fig. 3 (middle left and middle right panels) lies poleward of low EPV in the uppermost troposphere. From 2100 to 2230 UT the region of low EPV expands poleward over the jet maximum, deforming PV contours poleward and downward in a counter-clockwise pattern, i.e., with negative zonal relative vorticity, $\left(\frac{\partial w}{\partial y} - \frac{\partial v}{\partial z}\right)$ (Fig. 3 (middle left and middle right panels)). The trajectory ribbons highlight the vertical motion fields which lift moist PV anomalies to the base of the stratosphere. Once the ribbons reach the anticyclonic shear side of the jet, the isotachs tighten, strengthening the jet core wind speeds. This jet strengthening mechanism reveals an important contributing factor to quasi-stationary precipitation segments and the STE mechanism associated with midlatitude storms.

Another important consequence of this inertial instability at the base of the stratosphere is the STE which occurs as inertially stable air accelerates poleward and downward around the westerly jet. Typically, low PV air surges poleward over the westerly jet, attaches itself to the westerly jet through turbulence, and becomes a mixed boundary layer for the jet. This turbulently mixed air is then directed in a downward and eastward spiral around the jet, re-entering the troposphere. Support for this concept may be seen in Fig. 3 (bottom left panel), which shows that high TKE and low values of Ri emanate from the region of negative EPV, accompanying this overturning meridional circulation around the jet in a shallow layer of mixed stratospheric and tropospheric air.

Turbulence and gravity waves are noticeably enhanced in the UTLS on the poleward side of westerly jets, and play an important role in mixing (Lindzen and Tung 1976; Uccellini et al. 1987; Pavelin et al. 2002; Whiteway et al. 2003; Duck and Whiteway 2005; Koch et al. 2005). Mixing near the jet stream at the tropopause and internal waves breaking in the vicinity of the tropopause are potentially important in the exchange of trace gases such as ozone between the troposphere and the stratosphere (Clayson and Kantha 2007). TKE is present in areas of strong shear or in regions of convective motions. As observed in Fig. 3 (top left, top right and middle left panels), areas of intense vertical motion carry negative EPV to the anticyclonic shear side of the midlatitude westerly jet, setting the stage for production of TKE in the affected region. Fig. 3 (bottom left panel) reveals TKE on the anticyclonic shear side of the jet with values of 0.5 m^2/s^2, indicating turbulent motions. This layer of air with significant TKE spirals poleward and downward around the jet, facilitating STE triggered by anomalous negative EPV on the anticyclonic shear side of the jet. The TKE contours suggest a shallow layer of mixed stratospheric and tropospheric air that circulates around and down into the troposphere, as evidenced by contours of high PV down to ~4 km (Fig. 3 (middle left and middle right panels)).

The Richardson number is a useful measure of the likelihood of generating TKE, with values less than 0.25 implying instability (Markowski and Richardson 2010). Fig. 3 (bottom left panel) shows that $Ri < 0.25$ and high TKE spatially and temporally coincide in the poleward and downward circulation region. A turbulent mixed boundary layer is produced within this region, where stratospheric air combines with tropospheric air. Once again, the STE circulation patterns are revealed through the Ri and TKE turbulent mixing patterns in the poleward and downward circulation around the midlatitude westerly jet.

Additional analysis from the Eta model provides conclusive results regarding the inertially unstable conditions in the UTLS and its connection with banded precipitation and STE. Figure 2 (bottom left panel) unveils a large inertially unstable area in a 300-250 hPa layer over Wisconsin at 0000 UT, spatially similar to the ECMWF analysis from Fig. 3 (top left panel). The origin of this 300-250 hPa inertial instability is evident in Fig. 3 (top left and top right panels). The low EPV which resides at the surface has ascended throughout the depth of the troposphere via intense areas of vertical motion, as seen in Fig. 2 (top left and top right panels). The Eta 24-hr accumulated precipitation showing the resulting banded precipitation at 0600 UT on 6 February is displayed in Fig. 2 (bottom right panel), which shows the spatial superposition of inertially unstable air at the base of the stratosphere lying over the updraft and the precipitation maximum. This reveals the intimate relationship between the inertially unstable regions and a deep intrusion of high PV air originating from the stratosphere and wrapping poleward and downward around the westerly jet (Fig. 2 (bottom left panel) and Fig. 3 (middle left and middle right panels)). The Eta model also indicates a correlation between the negative EPV region on the equatorward side of the jet and 24-hr accumulated precipitation during 0000 UT 6 February to 0000 UT on 7 February, which is shown in Fig. 3 (bottom right panel). The regions of negative EPV correspond spatially and temporally to the areas of intense precipitation.

3.2. Case 2, 22 April 2005 – Surface Low Between Two Weak Jets

Another case that illustrates inertial instability facilitated STE is a stationary precipitation and STE event that occurred throughout southern Wisconsin on 22 April 2005. Figure 4 shows the Eta model overview of the dynamics associated with the storm on 1200 UT 22 April 2005. A weak low pressure system (Fig. 4 (top left panel)) advanced through the mid-section of the nation and, once again, banded precipitation erupted repeatedly forming and dissipating on the

northwest side of the low pressure center (Fig. 4 (bottom right panel)). The banded structures were embedded in a southeasterly flow while the main flow of the system was to the east. These elongated bands of precipitation lingered into the early morning and late evening hours of 22 April 2005.

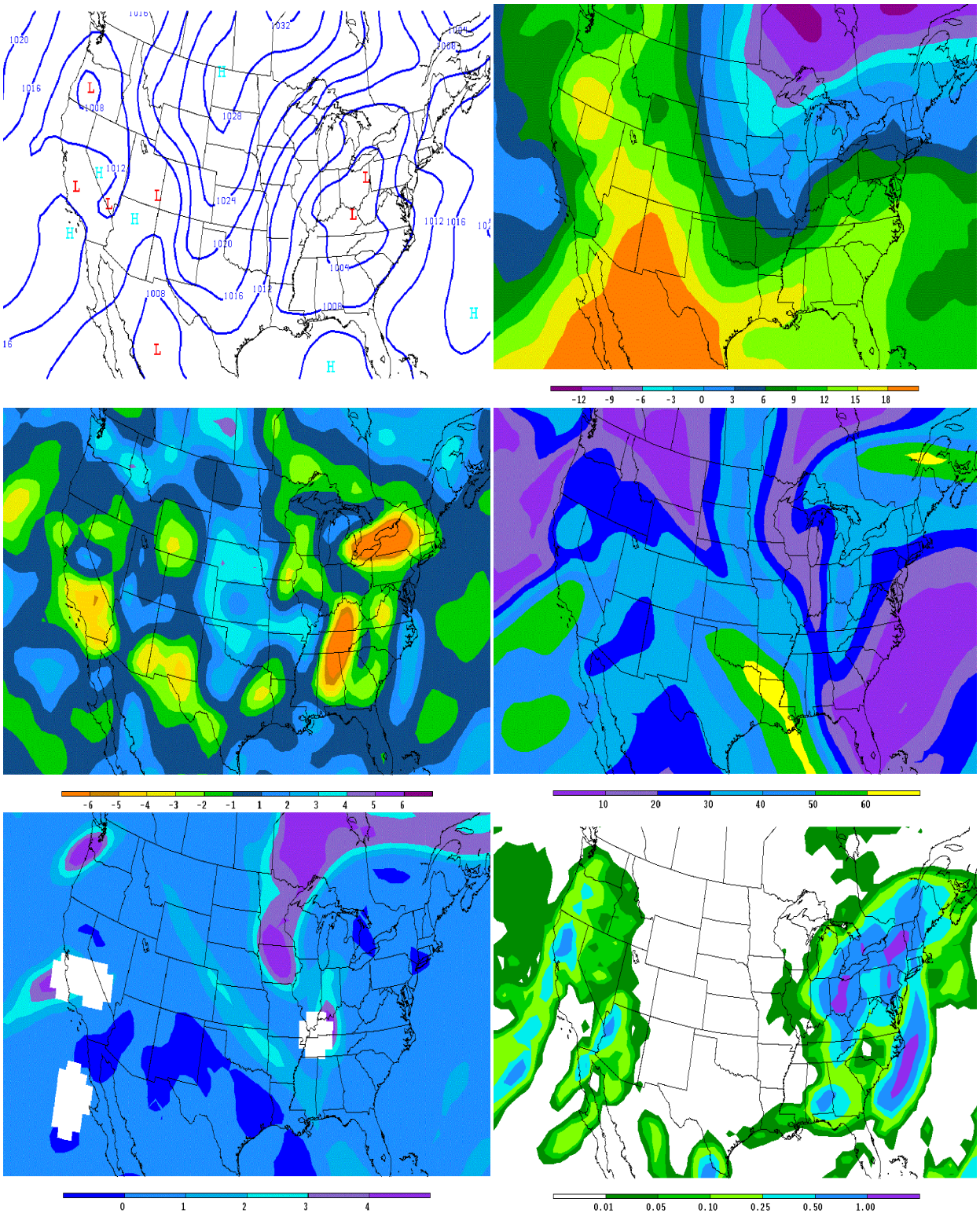

Figure 4. Synoptic setting for Case 2, using NCEP eta analysis for 0000 UT 23 April 2005: top left panel) sea level pressure (blue contours, interval 4 hPa); top right panel) 850 hPa temperature (color bar, interval 3°C); middle left panel) 700 hPa vertical pressure velocity (color bar, interval

1 Pa/s); (middle right panel) 300 hPa wind speed (color bar, interval 10 m/s); bottom left panel) 300-250 hPa EPV (color bar, interval 1 PVU); and bottom right panel) 24-hr accumulated precipitation during 0000 UT 22 April – 0000 UT 23 April 2005 (color bar, in inches).

During the time of the most intense precipitation, a distinct patch of negative EPV is found on the anticyclonic shear side of the jet (compare Fig. 4 (middle right and bottom right panels)). This negative EPV then induces STE as air flows poleward then downward and equatorward around the jet.

During this time an intricate set of circumstances was materializing in the upper levels of the atmosphere. Fig. 4 (middle right panel) shows a moderate jet stream with maximum wind speeds near 50 m/s, and a subtropical westerly jet arcing anticyclonically through Southern California into Texas. A region of negative EPV is seen over Ontario, just to the northeast of a PV maximum over Iowa and to the east of the jet entrance region (Fig. 4 (bottom left panel)).

Fig. 5 (top left and top right panels) display an impressive packet of negative EPV on the anticyclonic shear side of the jet, possessing negative values exceeding -2 at 250 hPa (~11 km). Similar to Case 1, inertial flare-ups formed and dissipated through the 250 hPa level due to this negative EPV at the base of the stratosphere. This low PV air ascended poleward and adhered to the surface of the jet, participating in a turbulent mixed boundary layer. This is an entry point for stratospheric-tropospheric air to become interweaved, resulting in a previously unrealized mechanism for STE. Fig. 5 (middle left and middle right panels) illustrates this point, as high PV air ascends poleward and downward around the jet, pushing stratospheric air deep into the troposphere, due to the existence of this inertial instability at the base of the stratosphere. This represents a distinct mechanism for producing tropopause folds, which transport air with high PV, low water vapor, and high ozone deep into the troposphere.

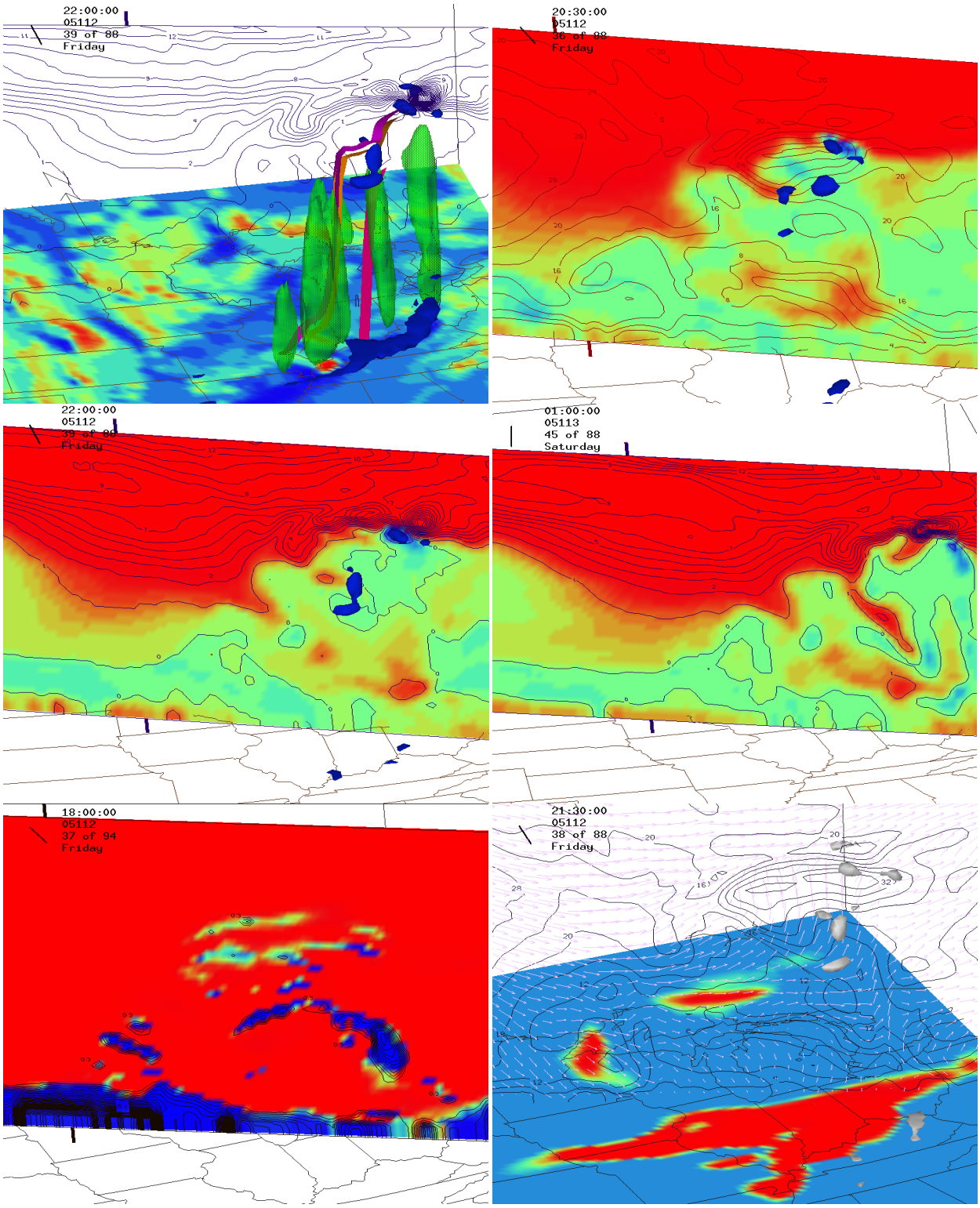

Figure 5. UWNMS simulation of Case 2, initialized with ECWMF data on 22 April 2005 showing the relationship among convection along the cold front, negative EPV, and jet location. Top left panel shows a section of EPV (black contours, interval 1 PVU), an isosurface of -2 PVU

(dark blue), and thunderstorm updrafts (green isosurfaces of 4 cm/s). Top left panel also shows EPV at the surface (red for EPV < 0 and blue > 1 PVU). The colored ribbons in the top left panel show trajectories arriving at the region of anomalous EPV in the upper troposphere originating 14 hr earlier. Top right panel 2030 UT 22 April, middle left panel 2200 UT 22 April, and middle right panel 0100 23 April show the evolution of anomalous PV (dark blue isosurface of -2 PVU) and EPV (low in blue, high in red). Contours in top right panel show wind speed every 10 m/s, while those in the middle left and the middle right show PV every 0.1 PVU. Bottom left panel shows the distribution of TKE (contour interval 0.5) and Ri (blue < 0.25, red > 1.0) at 1800 UT 22 April. Bottom right panel shows the meridional circulation around the jet (arrows), regions of negative EPV (white), wind speed contours every 10 m/s, and 24 hr average precipitable water (red exceeds 0.8 kg/m^2) at 2130 UT 22 April.

A synoptic maximum in ascent near 700 hPa occurs to the north of the surface low, inbetween the jets (Fig. 4 (middle left and middle right panels)). In direct relation to the previously discussed negative EPV air, a distinct region of upward vertical motion exists just upstream of the negative EPV anomaly near 250 hPa. This upward vertical motion owes its existence to a warm moist upglide pathway which emanates from the surface and is evident in the back trajectories shown in Fig. 5 (top left panel). Note how the contours of stratospheric PV are bent poleward and downward from the location of the negative EPV anomaly.

When low PV air surges poleward over the polar westerly jet it adheres to the jet via turbulence, through the mixing of stratospheric and tropospheric air. This flow layer appears to attach to the jet through entrainment, perhaps similar to the Coanda effect. The fluid motion is then directed downward and finally equatorward as the flow detaches itself from the jet. Fig. 5 (top right, middle left and middle right panels) illustrates repeated events whereby mixed stratospheric-tropospheric air pushes downward and equatorward into the troposphere.

The entrainment of stratospheric air is suggested by the contours of high TKE and low Ri (Fig. 5 (bottom left and bottom right panels)), which wrap around the jet in a meridional overturning circulation. TKE and Ri patterns reveal mixing on the anticyclonic shear side of the

jet, followed by mixed air wrapping poleward, downward, and then equatorward, deep into the troposphere. Turbulent mixing of stratospheric air deep into the troposphere is revealed through this circulation pattern.

An east-west band of precipitation during the 24 hr prior to 0000 UTC 23 April is seen in the Eta analysis to the north of the surface low over Northern Illinois (Fig. 4 (top left panel), (bottom right panel)), spatially coincident with negative PV in the 300-250 hPa layer (Fig. 4 (bottom left panel)) and rising motion (Fig. 4 (middle right panel)) ahead of the rolled-up PV streamer (Fig. 4 (bottom left panel)). Fig. 5 (bottom right panel) shows that the updraft and negative EPV anomalies lie over the precipitation maximum on the equatorward side of the jet in the UWNMS simulation.

The region of negative EPV in the Eta analysis (Fig. 4 (middle right panel)) correlates fairly well spatially and temporally with higher-resolution anomalies of negative EPV seen in the UWNMS (Fig. 5 (top left, top right, middle left and middle right panels), although the whole system is slightly farther south in the UWNMS simulation. Due to the 12 km inertial instability on the anticyclonic shear side of the jet, "inertial flare-ups" ensue, creating a localized wind speed maximum (Fig. 5 (top right panel)), and deformation of PV contours poleward and downward (Fig. 5 (top right and middle left panels)), and then equatorward below the jet into the troposphere in thin sheets (Fig. 5 (middle right panel)).

3.3 Case 2 and GEOS Ozone data

Case 2 also reveals important implications for the prediction of global climate change associated with ozone transport from the stratosphere into the troposphere. Downward transport

from the stratosphere not only constitutes the primary removal mechanism for many stratospheric species, including those involved in ozone depletion, but also represents a major input of ozone into the tropospheric chemical system (Levy et al., 1980). To explore this transport, GEOS Ozone data was implemented into the UWNMS model and reveals similarly conclusive evidence regarding the nature of STE associated with inertial instability in midlatitude cyclones.

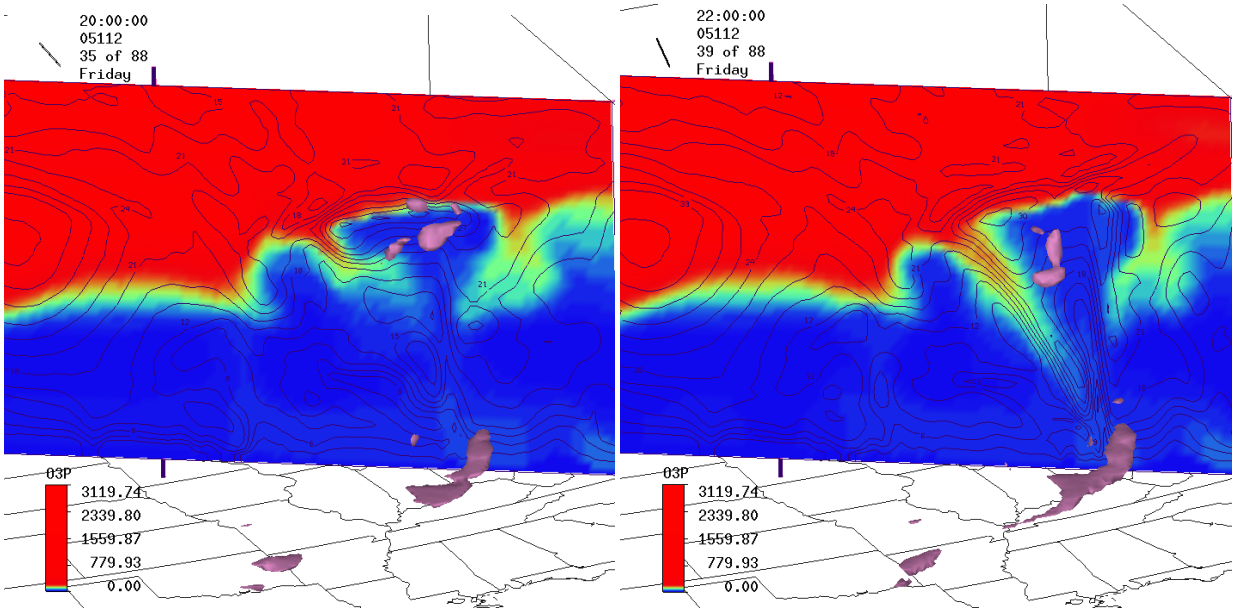

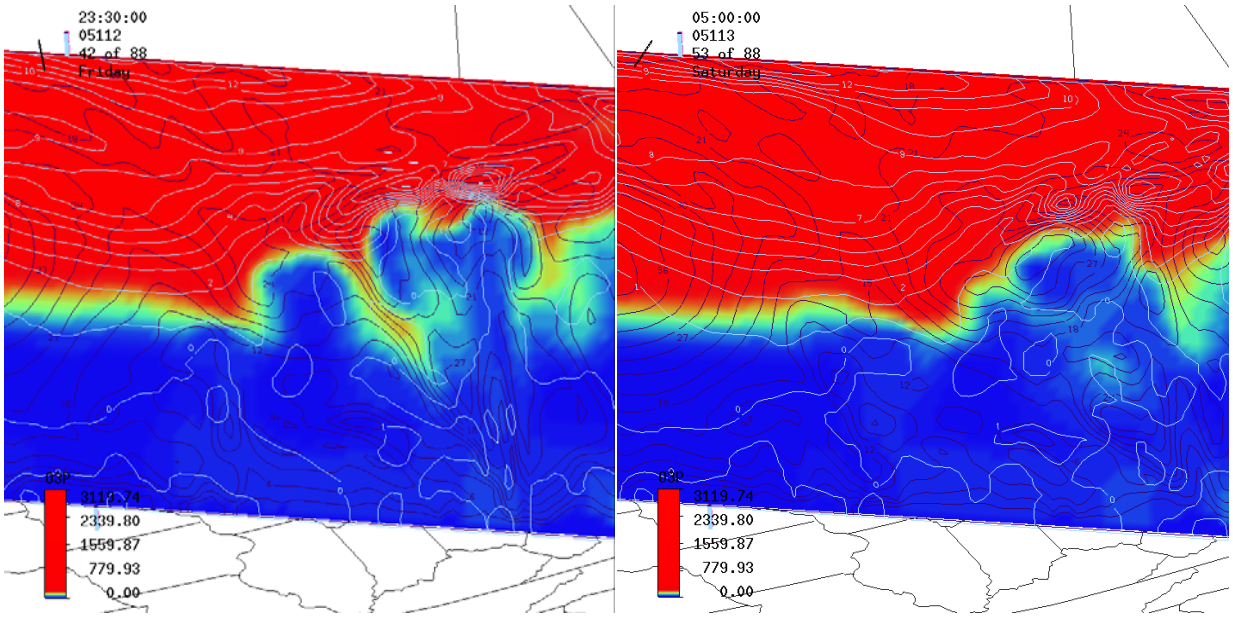

Figure 6. UWNMS simulation of Case 2 using GOES Ozone showing the relationship between STE, ozone and negative EPV. All panels show jet wind speeds (black contours, every 4 m/s), EPV (light blue contours, every 1 PVU), and red shading (high ozone levels), yellow shading (moderate ozone levels), and blue shading (low ozone levels). Top row (left panel) is at 2000 UTC on 22 April 2005. Top row (right panel) is at 2200 UTC on 22 April 2005. Bottom row (left panel) is at 2330 UTC on 22 April 2005. Bottom row (right panel) is at 0500 UTC 23 April 2005.

This circulation, which is similar to the pattern of high PV stratospheric air wrapping poleward and downward as shown in Fig. 5 (top left, top right, middle left and middle right panels), is perhaps even more striking in its overall appearance and magnitude in the ozone field.

Fig. 6 (top left panel) shows the situation as inertially unstable air appears on the anticyclonic shear side of the jet: a localized inertial flare-up with a minor core wind speed of 30 m/s is evident. At 2000 UTC this inertially unstable region, with values near -2 PVU once again coincides with enhanced meridional circulations, resulting in a surge of high ozone air

equatorward and into the troposphere. Just two hours later at 2200 UTC, this process is enhanced, as Fig. 6 (top right panel) shows a surge of ozone rich air digging deeper into the troposphere. At 2330 UTC as shown in Fig. 6 (bottom left panel) two inertial flare-ups are evident, as more negative EPV air interacts with the anticyclonic shear side of the jet. Around these inertial flare-ups more ozone rich air sinks poleward and downward, as stratospheric fingers are evident sinking into the troposphere. Five and one half hours later, at 0500 UTC the next day, more inertially unstable air interacts with the anticyclonic shear side of the jet, resulting in another surge of high ozone air penetrating the troposphere (Fig. 6, bottom right panel).

The ozone dynamics in Fig. 6, coupled with the high PV dynamics in Fig. 5 overlap with one another, compliment one another and fill in critical time gaps. The evidence is clear surrounding Case 2. Negative EPV from the surface cold front becomes increasing more negative with increasing altitude due to latent heat processes along the vertical path (Grams et. al., 2011). When this inertially unstable air affixes itself to the anticyclonic shear side of the jet, meridional circulations are enhanced. These inertial instability induced circulations yield an STE mechanism whereby ozone rich air sinks poleward and equatorward around the jet. This proves that the vertical transport of air through the depth of the troposphere can occur on time scales as short as a few hours via moist convection in the middle latitudes (Holton et. al., 1995).

3.4. Case 3, 20-21 February 2011 – Surface Low Between Two Weak Jets

Another distinctive mid-latitude storm which highlights negative EPV on the anticyclonic shear side of the polar jet in relation to banded quasi-stationary precipitation and STE took place on 20-21 February 2011. Figure 7 shows an Eta model overview of the dynamics associated

with the storm at 1200 UT on 20 February 2011. A strong low pressure system developed over Iowa (Fig. 7 (top left panel)) at the head of the large stratospheric PV streamer angling from Arizona toward Wisconsin (Fig. 7 (bottom left panel)), with maximum ascent at 700 hPa (Fig. 7 (middle left panel) over Wisconsin on the poleward side of the western jet's exit region, but on the equatorward side of the eastern jet's entrance region over Lake Superior (Fig. 7 (middle right panel)).

Once again, an intense low pressure system (Fig. 7 (top left panel)) moved eastward into the upper Mississippi Valley and strengthened over central Iowa and Illinois, yielding strong bands of precipitation to the north and west of the low pressure center. As the low progressed eastward, the elongated precipitation structure remained fairly stationary, extending across North Dakota, Minnesota, and Wisconsin (Fig. 7 (bottom right panel)). Before departing the area Madison, Minnesota received nearly 19" of snow in 24 hr. A distinct swath of negative EPV in the 300-250 hPa layer over the upper Mississippi valley (Fig. 7 (bottom left panel)) is once again identified as leading to STE and an eruption of inertial flare-ups.

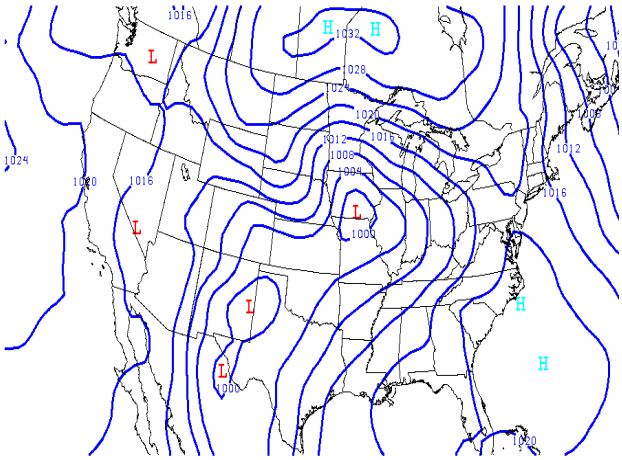
1016
1032
1028
1024
1020
1012
1008
1004
1000
1024
1020
1016
1012
L
H

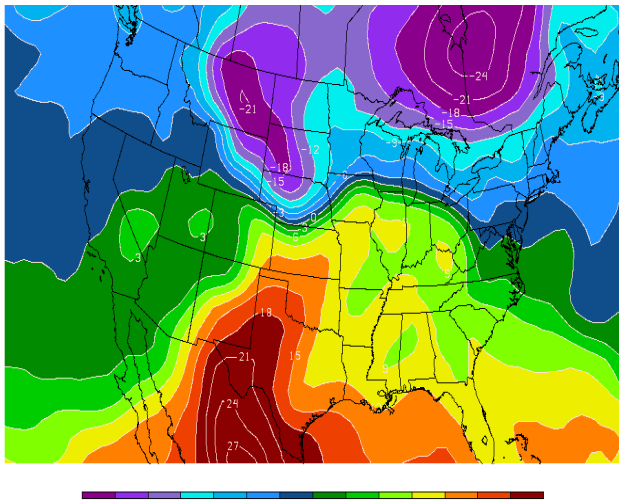
-24
-21
-18
-15
-12
-9
-6
-3
0
3
6
9
12
15
18
27

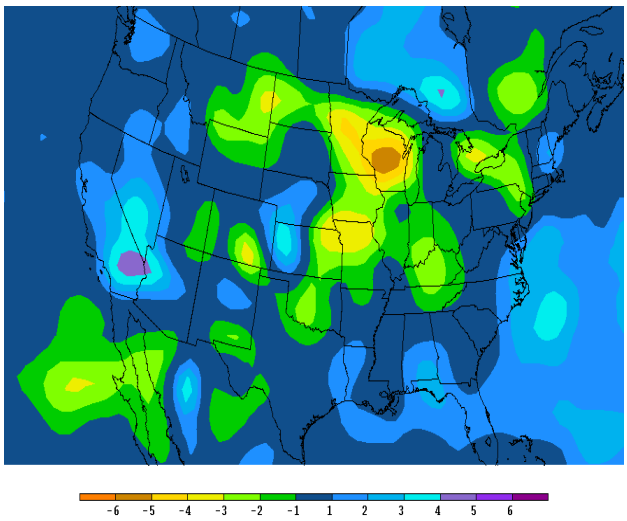

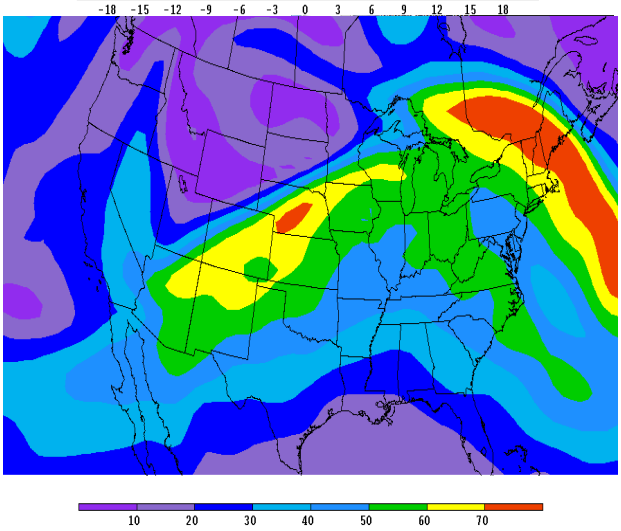

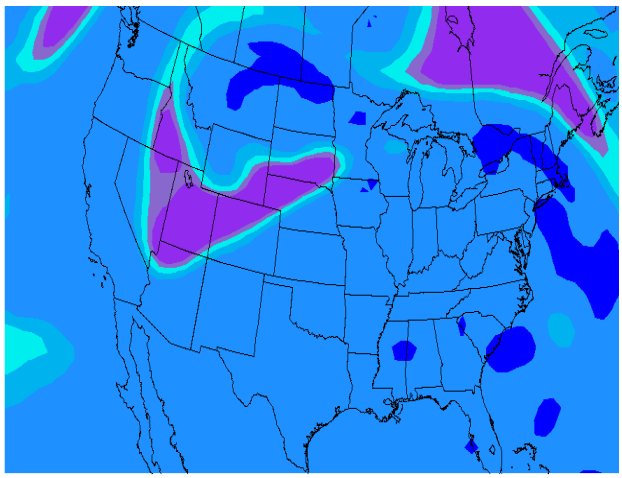

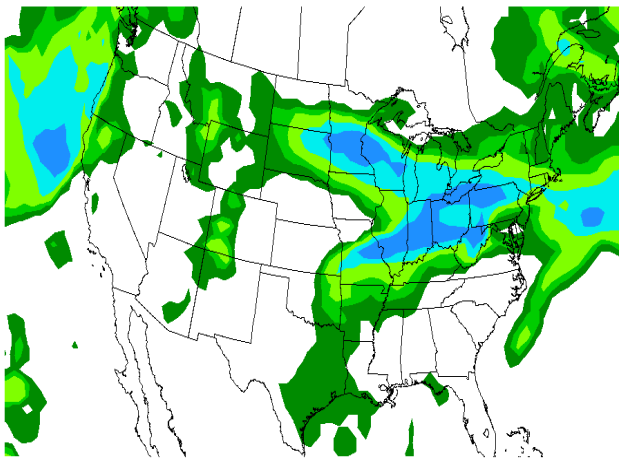

Figure 7. Synoptic setting for Case 3, using NCEP eta analysis for 0000 UT 21 February 2011: Top left panel) sea level pressure (blue contours, interval 4 hPa), Top right panel) 850 hPa temperature (color bar, interval 3^{o}C), Middle left panel) 700 hPa vertical pressure velocity (color bar, interval 1 Pa/s), Middle right panel) 300 hPa wind (color bar, interval 10 m/s), Bottom left panel) 300-250 hPa EPV (color bar, interval 1 PVU), and Bottom right panel) 24-hr accumulated precipitation during 0000Z 20 February – 0000Z 21 February 2011 (color bar, in inches).

As the cold front associated with the surface low pressure system intensified, pronounced areas of upward vertical motion erupted near the low EPV region at the surface (Fig. 8 (top left and top right panels)). As these updrafts formed they lifted the low EPV air through the atmosphere, which is visualized with the use of back trajectories in Fig. 8 (top left panel). During their vertical journey this low EPV air became increasingly more negative and more organized, as values reached -1 PVU. Note how the PV contours in Fig. 8 (top left panel) show an upward bulge around the negative EPV anomaly, which lies immediately equatorward of a jet speed maximum (Fig. 7 (middle right panel)).

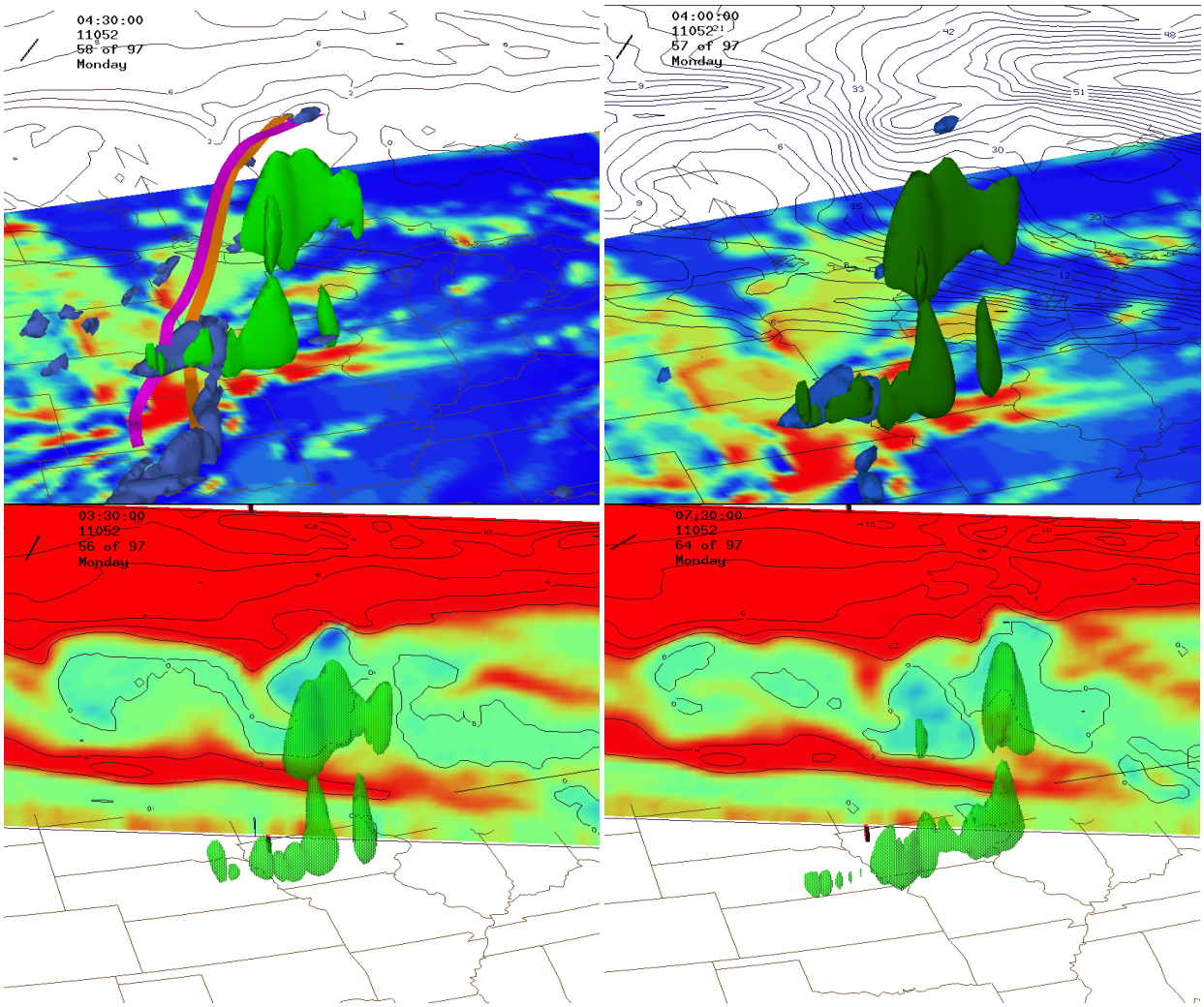
04:30:00
11052
58 of 97
Monday
04:00:00
11052
57 of 97
Monday
03:30:00
11052
56 of 97
Monday
07:30:00
11052
64 of 97
Monday

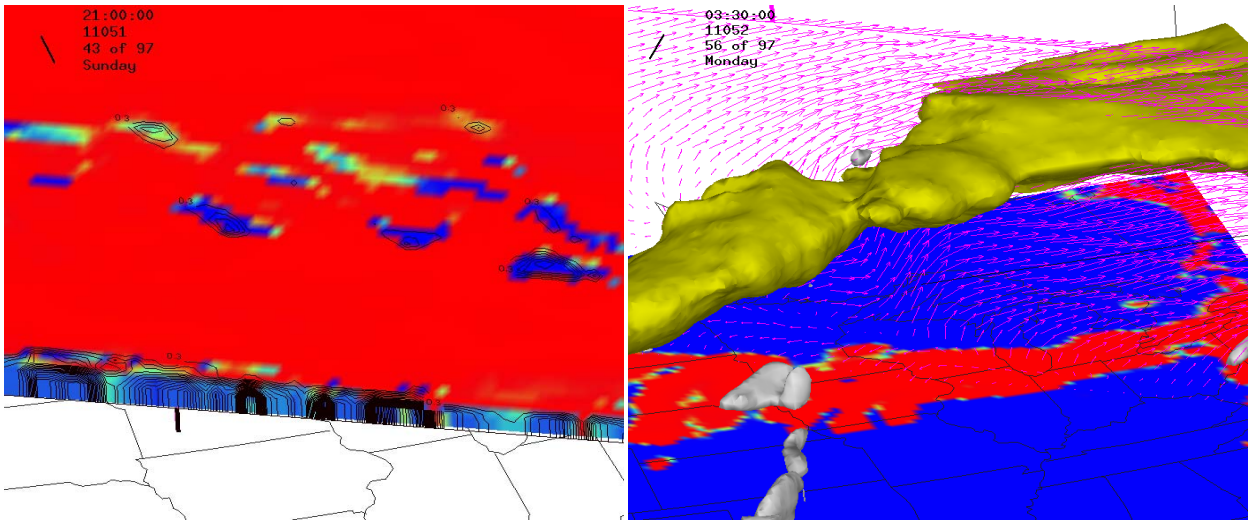

Figure 8. UWNMS simulation of Case 3, initialized with ECWMF data on 1200 UT 20 February 2011, showing the relationship between convection along the cold front, negative EPV, and jet location. A green updraft isosurface of 4 cm/s is shown in Top left panel) 0430 UT, Top right panel) 0400 UT, Middle left panel) 0330 UT, and Middle right panel) 0720 UT on 20 February. Top left and top right panels show an isosurface of -2 PVU (dark blue) and EPV at the surface (red EPV < 0, blue EPV > 1 PVU). The section in the top left panel has contours every 0.1 PVU, while the top right panel shows speed contours every 5 m/s. The colored ribbons in the top left panel show trajectories arriving at the region of anomalous EPV in the upper troposphere originating 14 hr earlier. Middle left and middle right panels show the evolution of EPV, ranging from low (blue) to high (red) values. Bottom left panel shows the distribution of TKE (contours every 0.5 m^2/s^2) and Ri (blue < 0.25, red > 1.0) at 2100 UT 20 February. Bottom right panel shows the meridional circulation around the jet (arrows), regions of negative EPV (white), an isosurface of 30 m/s wind speed (green), and 24 hr average precipitable water (red exceeds 0.8 kg/m^2).

Areas of negative EPV air were repeatedly deposited on the anticyclonic shear side of the polar jet and as the EPV anomalies merged with the polar jet, a notable strengthening of the jet occurred, erupting into inertial flare-ups. This unusual situation continually transpired along the entire horizontal length of the mid-latitude storm. Inertial flare-ups perpetually formed and dissipated through the constant feed of negative EPV air via updrafts exceeding 4 cm/s. As each negative EPV section positioned itself on the anticyclonic shear side of the jet it created an organized inertial flare-up maximum. These anomalous inertial flare-ups correspond with the

horizontal extent of the banded quasi-stationary precipitation outbreak over the northern tier of states.

Figure 8 (top left panel) illustrates that low PV air, initially at the surface, ascends through the troposphere and attaches itself to the upward and equatorward side of the newly developed inertial flare-up (local speed maximum in Fig. 8 (top right panel). These trajectories reveal where the low EPV air originates and traces its path through the troposphere. As each trajectory ribbon ascends vertically it represents the low and eventually negative EPV. The colored ribbons immediately flow to the anticyclonic shear side of the jet, causing an instant tightening of the isotachs, revealing a strengthening in wind speeds. This inertial flare-up formation occurs along the horizontal extent of the midlatitude storm as the negative EPV ribbons are continually pushed upward to the base of the stratosphere by vertical motion fields. These back trajectories demonstrate the importance of vertical motion, low EPV and jet dynamics in midlatitude cyclones that produce quasi-stationary banded precipitation.

Wind shear and convective instability are the two primary sources of TKE. Fig. 8 (bottom left panel) supports the fact that convective instability is widespread throughout the tropospheric boundary layer. Turbulence is generated throughout these regions of convective instability. Convective TKE tends to spread into the stable stratospheric region by entrainment. Inertial instability generates further turbulence on the upward and equatorward side of the jet. It is through entrainment that a poleward and downward pattern emerges, bringing mixed stratospheric air into the mid- to lower troposphere. Fig. 8 (bottom right panel) shows that this mixed air wraps around the inertial flare-up, with high PV air from the stratosphere entering the troposphere.

Intense vertical wind shears in the UTLS associated with this poleward surge are sufficient to keep Ri quite small. Fig. 8 (bottom left panel) also shows that the pattern of Ri < 0.25 aligns perfectly with that of enhanced TKE. The low Ri numbers are consistent with maintenance of turbulence as the mixed stratospheric/tropospheric air moves poleward and downward around the mid latitude westerly jet. A turbulent boundary layer is produced in the UTLS, bringing stratospheric poleward and downward into the troposphere. A new STE mechanism is revealed through this process of entrainment and turbulence induced by the inertial instability at the base of the stratosphere.

Supporting evidence regarding inertial instability at the base of the stratosphere and its correlation with precipitation maxima and STE is shown in Fig. 7 (bottom right panel). With the aid of the Eta model, a swath of inertial instability is evident in the 300-250 mb layer at 1200 UT on 21 February (Fig 7 (bottom left panel)). This agrees very well with the 12 km inertially unstable region shown in Fig. 8 (top left and top right panel). This STE mechanism is also apparent in Fig. 7 (bottom left panel), as stratospheric high PV air wraps poleward and downward around the inertial flare-ups. This unequivocally supplements the UWNMS higher resolution Fig. 8 (middle left and middle right panels), in which contours of PV sink poleward and downward around multiple inertial flare-ups into the mid-troposphere. There is an unambiguous connection between the patterns in the negative EPV anomalies at 300-250 hPa and the precipitation maxima in the 24 hour accumulated precipitation in Fig. 7 (bottom right panel). The 24 hr rainfall maximum in Fig. 8 (bottom right panel) agrees fairly well with NCEP Eta 24 hr rainfall, and supports the relationship among negative EPV anomalies near 11-12 km, STE, inertial flare-ups, and precipitation maxima over the inertial instability-facilitated upwelling maximum in midlatitude cyclones.

It is also important to note how the UWNMS and the Eta model visualized in GEMPAK displays mesoscale EPV < 0. In this research the UWNMS identifies individual anomalies at a 20 km resolution as seen in various cross sections. This EPV > 0 air can be viewed as an individual packet at a very specific altitude in a cross section and possesses an exact value. However in the Eta model with an 80 km resolution visualized in GEMPAK a more spread out EPV > 0 is identified only in a specific layer. In this work the 300-250 hPa layer was used and this revealed a larger less specific region on negative EPV without exact values.

4. Discussion of STE and Inertial Instability

It is the interactions between each of the aforementioned dynamical parameters that induces the precipitation structures that are at the focal point of investigation. Each factor in this case provides a positive feedback, acting together to increase the magnitude of the circulation anomaly. Strong vertical motion fields push the moist PV globules to the base of the stratosphere, where they create an STE mechanism instigated by low static and inertial stability, with a poleward and downward circulation of mixed UTLS air re-entering the troposphere in thin sheets. The TKE and Ri patterns support this mixing process, highlighting the pathway of poleward and downward circulation around the jet. This offers new insight into circulation patterns around midlatitude westerly jets. Each of these ingredients plays a vital role in the existence of quasi-stationary banded precipitation events in the upper Midwest.

Each of the aforementioned cases includes a distinct strengthening of the polar westerly jet, characterized as an "inertial flare-up". The strength of the jet in each case varies, however the same dynamical mechanisms provide a tightening of the isotachs and an overall increase of the jet core wind speed. Case 1 offers an already existing, well defined polar jet with a substantial wind speed maximum that strengthens even further after interaction with negative EPV. Case 2 shows multiple weak jets that are supplemented and enhanced after interacting with anomalous inertial instability. Similarly, Case 3 depicts several mini jets that are once again intensified through the deposition of negative EPV on the anticyclonic shear side of each micro jet. The nature of these "inertial flare-ups will be discussed in the next section, along with possible mechanisms regarding their existence and influence on the overall intensification and enhancement of the polar westerly jet.

5. Jet Intensification

5.1. History and Inertial Flare-ups

It is well known that midlatitude convective storm systems act to exchange properties vertically between the lower and upper troposphere and are important in maintaining the large-scale balance of angular momentum and energy (Palmen and Newton, 1969). Eliassen (1959) studied the role of diabatic heating in altering mass circulations. He found that such diabatic heating can strengthen a pre-existing circulation. Ninomiya (1971) concluded that thunderstorm outflow associated with intense convection aloft was a key dynamical parameter in changing the pre-existing upper level flow in the vicinity of intense storm development. Fritsch and Maddox (1980) analyzed the effects of Mesoscale Convective Complexes (MCCs) on synoptic scale flow. Through this work they found that convective warming as a result of diabatic latent heating intensified mass circulations in the mid troposphere. Maddox et al. (1980) inferred that a diabatic component of the isallobaric wind may be significant in areas of intense convection and may act to intensify the transverse mass circulations associated with a jet streak.

More closely related to the work presented here, Cahir (1971) showed that for a changing momentum field in upper tropospheric jet streaks, the mass field adjusts accordingly as the atmosphere attempts to maintain geostrophic and thermal wind balance. Keyser and Johnson (1984) investigated a similar phenomenon as they found a connection between jet intensifications and latent heating in an early springtime midlatitude MCC. In their study they analyzed a 15 m/s maximum wind speed increase within a jet streak over a three to six hour time span. Using isentropic coordinates, they found that latent heating in the MCC modified the direct mass circulation in the jet entrance region through the forcing of diabatic components of agostrophic motion. In the cases presented here, a transfer of momentum through the

conservation of angular momentum and the geostrophic adjustment process will be presented to further expand on the idea of jet intensification through the process of inertial instability.

Several dynamical processes are contributing to an increase in the overall jet intensification in these specific cases in which negative EPV is a dynamical focal point on the anticyclonic shear side of the jet. The first concept is the conservation of angular momentum. As negative EPV is moved upward and poleward from the surface it is transporting air from a lower latitude with higher angular momentum into the jet. The original speed of the air must increase as it moves poleward to conserve angular momentum. This sudden momentum surge, that often has negative EPV air on the anticyclonic shear side of the jet, adds a rotational speed increase to the jet core, producing an inertial flare-up. It can be calculated that if a parcel is displaced frictionlessly from 40° N to 41° N, a wind speed increase of 11 m/s would be evident.

Fig. 9 shows an idealized jet streak illustrating this convergence-divergence process. The divergence patterns in an idealized 300 mb jet streak can be enhanced in the presence of inertial instability. More specifically, inertial instability on the anticyclonic shear side of the jet (point 1 in Figure 9) creates a local acceleration of the jet by enhancing divergence in this region. By definition, inertial instability is a large departure from geostrophic balance, as the PGF greatly exceeds the Coriolis force. If these forces are out of balance a convergence of air at the left entrance region and divergence in the right entrance region occurs. Air in the middle portion of a jet streak is nearly geostrophic again. Additionally, a convergence of air in the right exit region and a divergence near the left exit region occurs. Therefore these two areas of divergence, one in the right entrance region and one near the left exit region, are associated with jet streaks. However, in a classical dynamical sense, these typical divergence patterns in an idealized jet streak are not due to inertial instability. In this work it is hypothesized that a region of inertial

instability on the anticyclonic shear side of the jet can enhance this area of divergence particularly in the left exit region, resulting in a locally enhanced jet wind speed increase called an “inertial flare-up”. The focal point of this chapter will be to investigate how the divergence (point 1 in Fig. 9) in a midlatitude westerly jet is amplified in the presence of inertial instability.

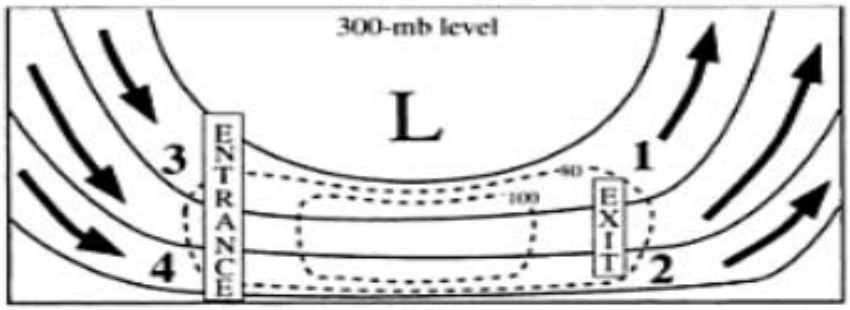

Figure 9. Idealized 300 mb jet streak. Imbalances between the Coriolis force and the pressure gradient force as air flows through a jet streak create areas of upper air convergence (shown in points 2 and 3) and areas of upper air divergence (shown in points 1 and 4). It is these areas of upper air divergence that cause enhanced jet accelerations. (A world of Weather: Fundamentals of Meteorology: a Text Laboratory Manual)

5.2. Case 1

Case 1 features an already well-developed midlatitude westerly jet. As regions of inertial instability adhere themselves to the anticyclonic shear side of the jet, a distinct tightening of the isotachs occurs as core wind speeds increase rapidly. Figure 10 (top left panel) shows a 60 m/s jet core wind speed at 1400 UT with an area of inertial instability not yet in the plane of the cross section. In three hours the regions of anomalous inertial instability have interacted with the anticyclonic shear side of the westerly jet and have increased core wind speeds by 15 m/s as shown in Fig. 10 (top right panel).

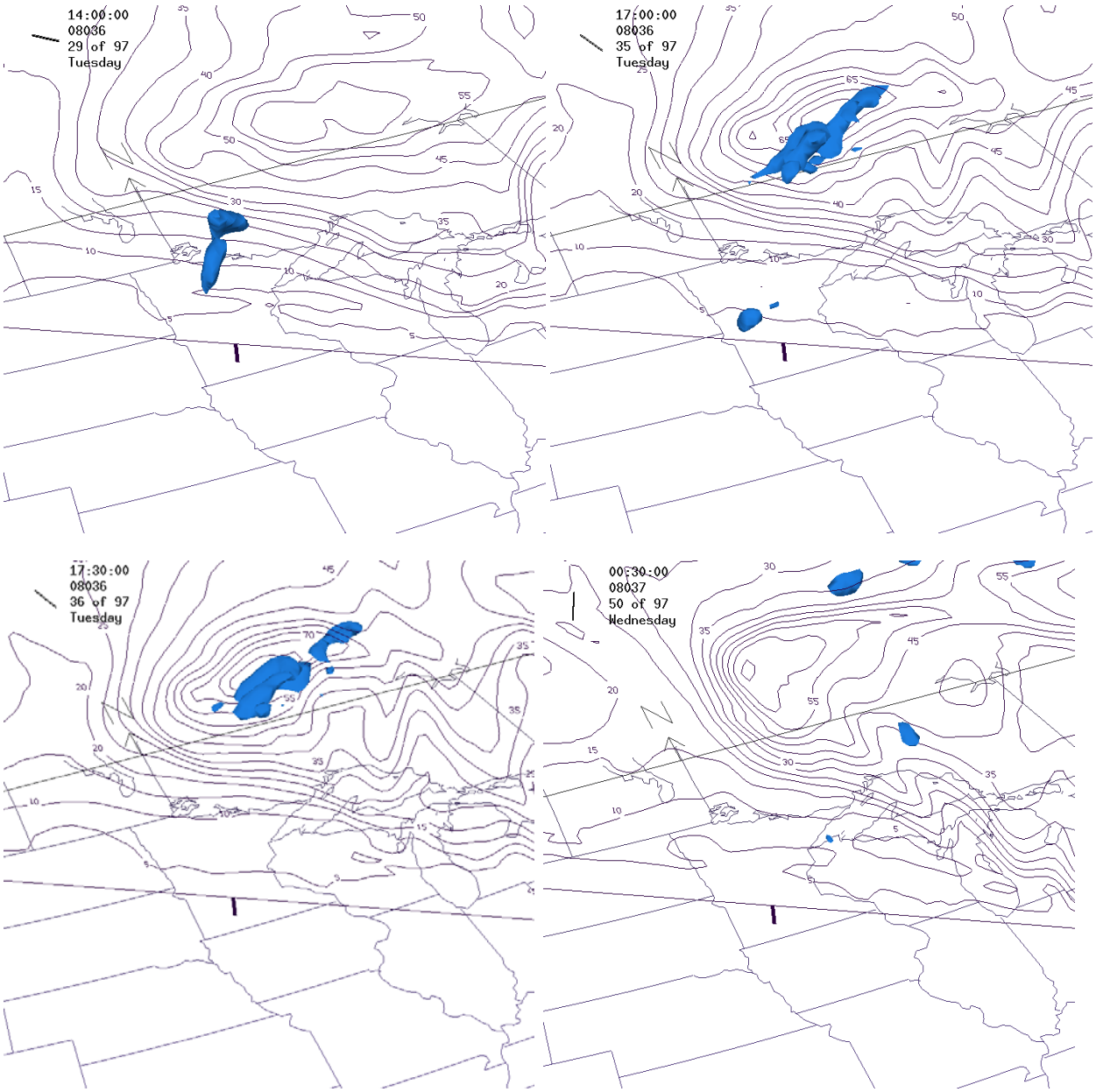

Figure 10. UWNMS simulation of Case 1 initialized with ECMWF data on 0000 UTC 6 February 2008 showing the relationship between inertial instability and jet speed increase. Top left panel shows a cross section of total wind speed (black contours, interval 5 m/s) and an isosurface of EPV (dark blue, -3 PVU) at 1400 UTC on 6 January 2008. At this time a 60 m/s jet core wind speed is evident. Top right panel (same as in top left) except 1700 UTC on 6 January 2008 is shown. As inertially unstable air (blue shading) interacts with the anticyclonic shear side of the jet, wind speed increases to 75 m/s. Bottom left panel (same as in top left and top right) except 0030 UTC on 7 February 2008 is shown.) Inertially unstable air leaves the plane of the cross section and jet core wind speed reduces to 65 m/s.

As shown in Figure 3 a, b, and c, these areas of negative EPV develop along the surface cold front and are lifted vertically and poleward to the UTLS via vertical motion. This negative EPV is being displaced about 3 degrees toward the pole. As this negative EPV air originates at a lower latitude, it is displaced several degrees poleward. This momentum then contributes to the jet, resulting in a continual increase in jet wind speeds. Fig. 10 (bottom left panel) portrays the same process, as a 5 m/s wind speed increase is seen just a half an hour later due to the negative EPV transferring momentum into the jet. Fig. 10 (bottom right panel) shows a relaxation of the jet core wind speeds after the negative EPV is no longer interacting with the jet.

Areas of inertial instability, as seen in Case 1, represent a large departure from geostrophic balance and add momentum to the jet streak by enhancing divergence, most specifically on the anticyclonic shear side of the jet. Imbalances between the PGF and the Coriolis force as air flows through the jet, creates upper air divergence in the right entrance and left exit region. Figure 10 shows that as an area of anomalous inertial instability moves through the anticyclonic shear side of the jet, a wind speed increase occurs. An increase of 20 m/s occurs in a three and a half hour time span, which can be seen in Fig. 10 (top right panel and bottom left panel). These areas of inertial instability at about -3 PVU, accelerate upper air divergence in the left exit region which is consistent with geostrophic imbalance. As the inertially unstable air moves northeastward and out of the plane of the cross section, as seen in Fig. 10 (bottom right panel), the divergence in the left exit region relaxes and the jet core wind speeds decrease by 15 m/s in a six and a half hour time span.

This upper air divergence in the right entrance and left exit region is enhanced as areas of inertial instability are lifted vertically to the anticyclonic shear side of the jet due to strong vertical motion. This can be seen in Figure 11 as the jet is shaded dark blue to correspond to

areas of strong and enhanced divergence. Areas of inertial instability with values of -2 PVU, which are shown in green in Fig. 11, create strong divergence on the anticyclonic shear side of the jet, thus increasing total wind speeds. Fig. 11 (top left panel) shows strong divergence and inertial instability on the

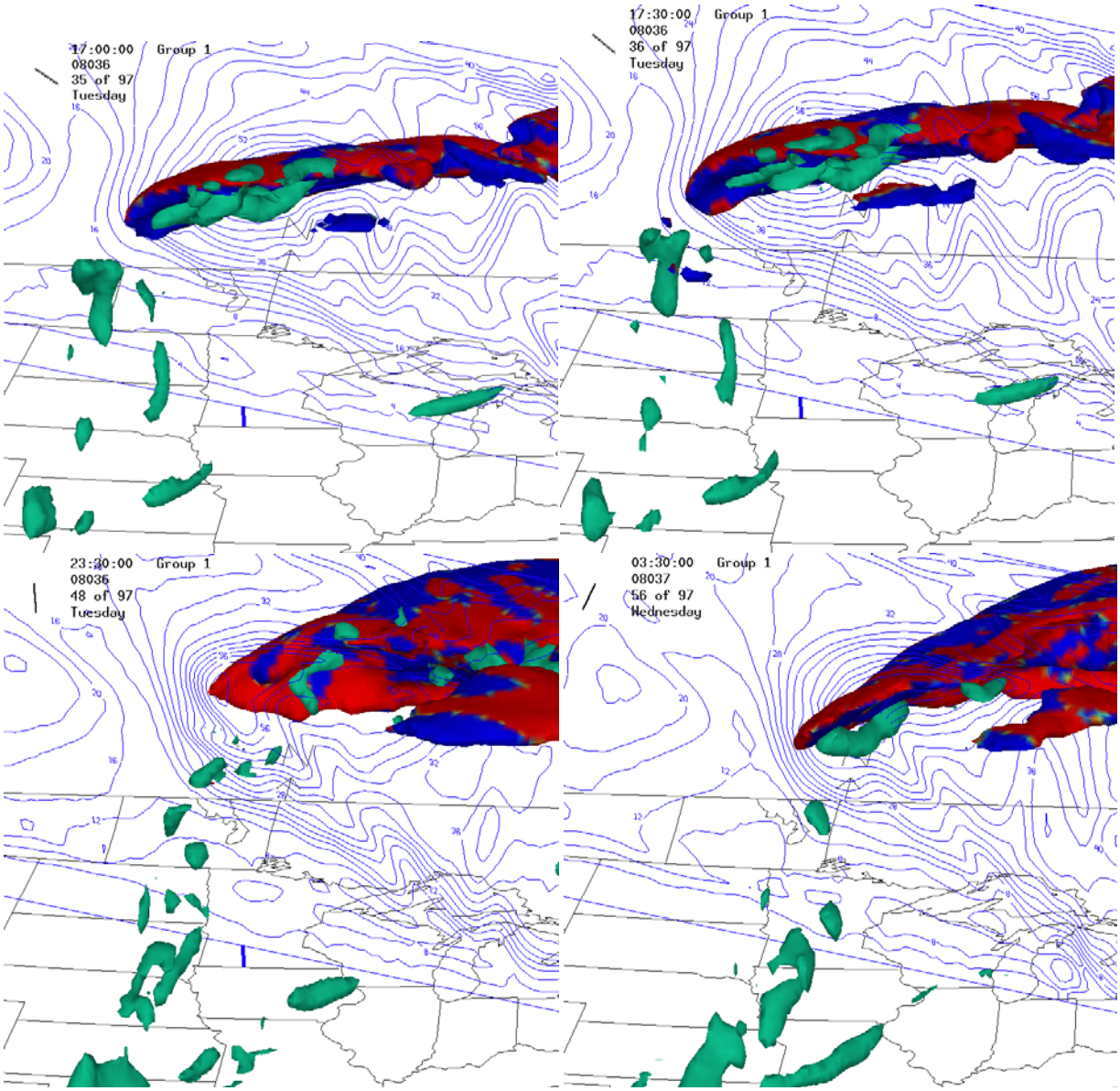

Figure 11. UWNMS simulation of Case 1 initialized with ECMWF data on 00 UTC 6 February 2008 showing the relationship between inertial instability and enhanced divergence associated with jet wind speed increase. The top left panel shows a cross section of wind speed (blue contours, 4 m/s), isosurface of jet (65 m/s), (shaded in blue) divergence and (red) convergence and the -3 PVU isosurface indicating inertial instability (green shading,) at 1700 UTC on 6 February 2008. As inertially unstable air enhances the divergence in the jet,

a distinctive tightening of the isotachs occurs. At 1700 UTC a 75 m/s jet core is identified. At 1730 UTC (top right panel) an 80 m/s jet core wind speed is evident as divergence is enhanced through inertial instability. Bottom left panel (same as in top left and top right) shows 2330 UTC and a relaxation of the jet core as inertially unstable air is less intense. Bottom right (same as in top left and top right and bottom left) only at 0330 UTC on 7 February 2008, shows more enhanced divergence due to the presence of inertial instability and once again a tightening of the isotachs.

anticyclonic shear side of the jet. Wind speeds increase from 75 m/s at 1700 UTC in Fig. 11 (top left panel), to 80 m/s at 1730 UTC in Fig 11 (top right panel). This enhanced divergence occurs in the presence of a wind speed increase of 5 m/s in a half an hour. As the areas of inertial instability and subsequent enhanced divergence begin to decrease on the anticyclonic shear side of the jet the total wind speeds tend to weaken. Fig. 11 (bottom left panel) shows this weakening as six hours later at 2230 UTC winds speeds have diminished to 60 m/s. As more areas of inertial instability begin to make their way to the anticyclonic shear side of the jet, another distinct strengthening due to increased divergence can be seen in Fig. 11 (bottom right panel) as four hours later at 330 UTC a 5 m/s increase is once again evident. In this case it is clear that a geostrophic imbalance from an inertially unstable state creates an area of strong divergence on the anticyclonic shear side of the jet causing an immediate and sudden increase in jet core wind speeds. When the anomalous inertially unstable region moves through the plane of the cross section an immediate cessation of the enhanced divergence occurs, temporarily weakening the wind speeds. This strengthening-weakening process occurs for the duration of the storm through south central Wisconsin.

To further exemplify the aforementioned inertial instability induced divergence and the subsequent jet speed intensification theory, absolute vorticity and divergence will be analyzed and compared with negative EPV and jet wind speed as the storm moves towards the eastern part of the United States. Figure 12 shows that as the absolute vorticity decreases, upper level

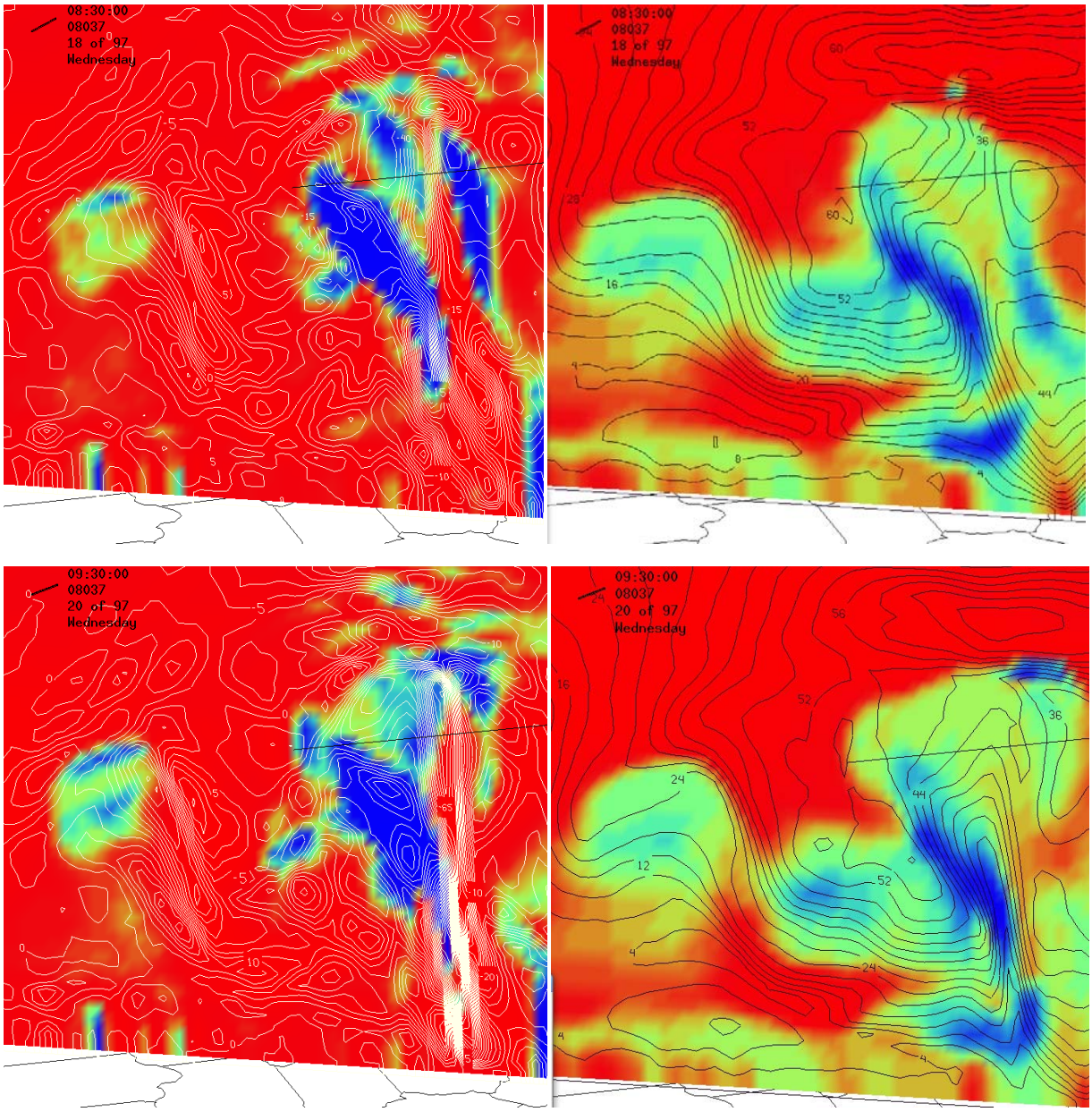

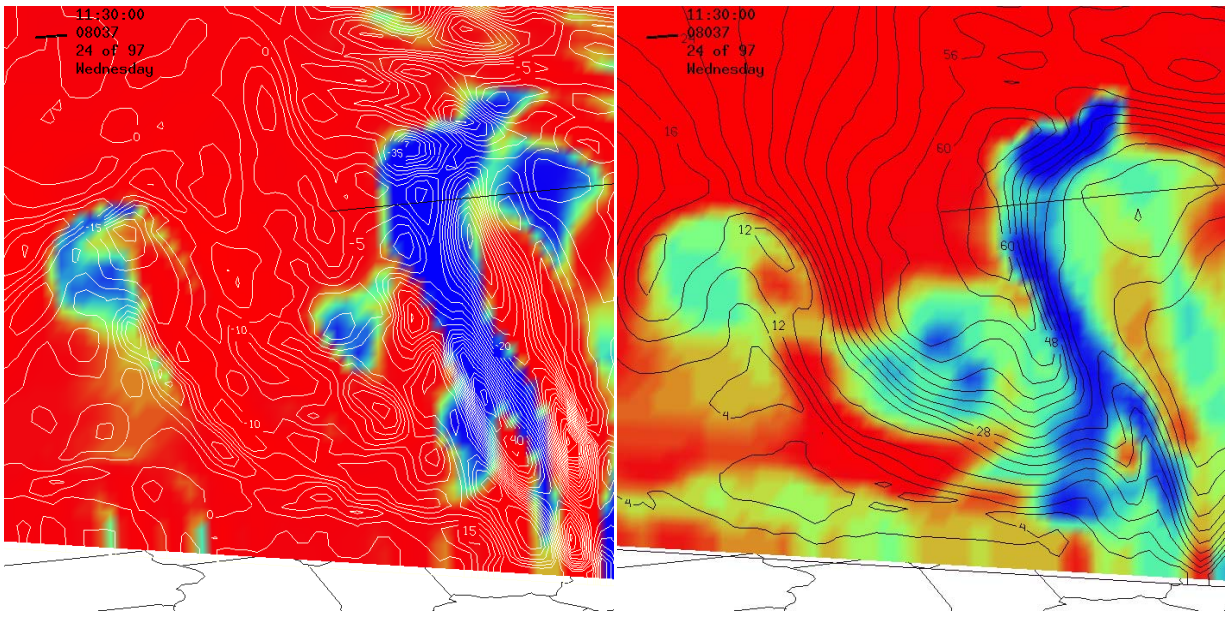

Figure 12. UWNMS simulation of Case 1 initialized with ECMWF data on 00 UTC 6 February 2008 showing the relationship between negative absolute vorticity, divergence, negative EPV and a tightening of the isotachs. Left panels show absolute vorticity, (blue shading is negative, red shading is positive), and divergence (white contours, interval 5 x 10^{-5} s^{-1}). Right panels show EPV (blue shading is negative, red shading is positive) and jet wind speeds (black contours, every 4 m/s). Top panels are at 0830 UTC on 7 February 2008. Middle panels are at 0930 UTC 7 February 2008. Bottom panels are at 1130 UTC 7 February 2008.

divergence, most specifically on the anticyclonic shear side of the jet (left panels), is intensified resulting in a jet wind speed increase (right panels). This analysis can be compared to negative EPV and jet wind speeds. Fig. 12 (right panels) shows that negative EPV on the anticyclonic shear side of the jet and an increase in wind speed is highly correlated with a decrease in absolute vorticity and upper level divergence (left panels). Fig. 12 connects negative EPV, negative absolute vorticity, and divergence to an intensified midlatitude westerly jet and a subsequent inertial flare-up.

5.3. Case 2

The jet dynamics involving Case 2 are much less intense with respect to overall jet core wind speed intensity and structure. As areas of inertial instability interact with a very low wind speed jet, a more organized jet with much greater wind speed is observed. Figure 13 shows a 16 m/s wind speed increase in a three and a half hour time span. Once again this inertially unstable air originates at the surface along the cold front associated with the storm. Similar to Case 1, this inertial instability is displaced about 2 degrees poleward. With this displacement, momentum is continually transferred into the jet, resulting in an increase in wind speed. This case,

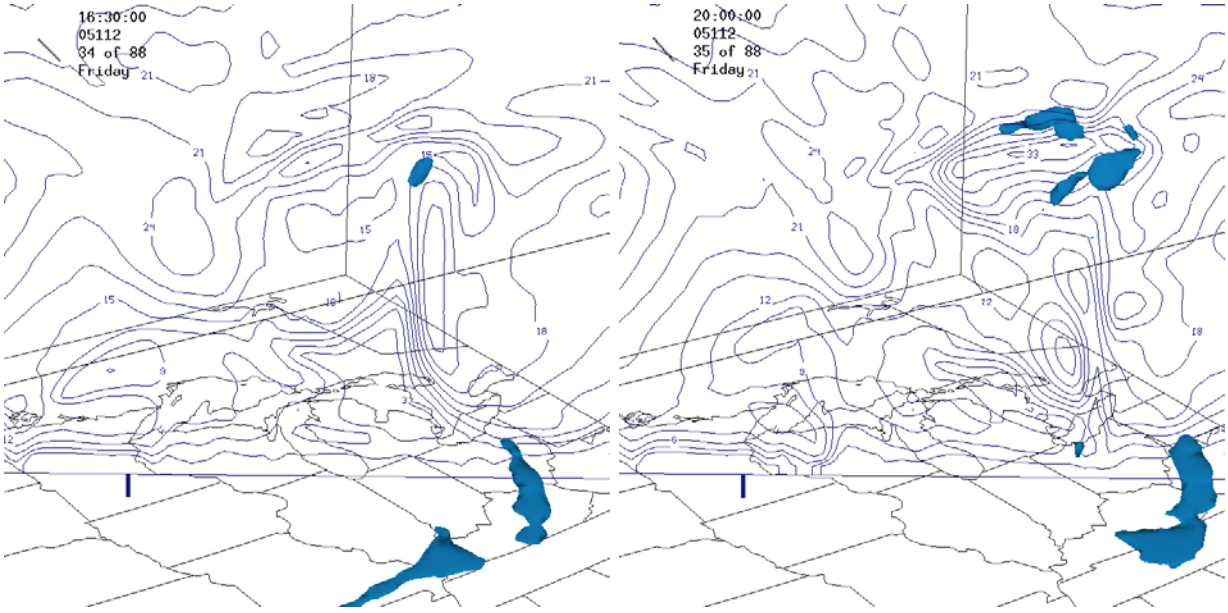

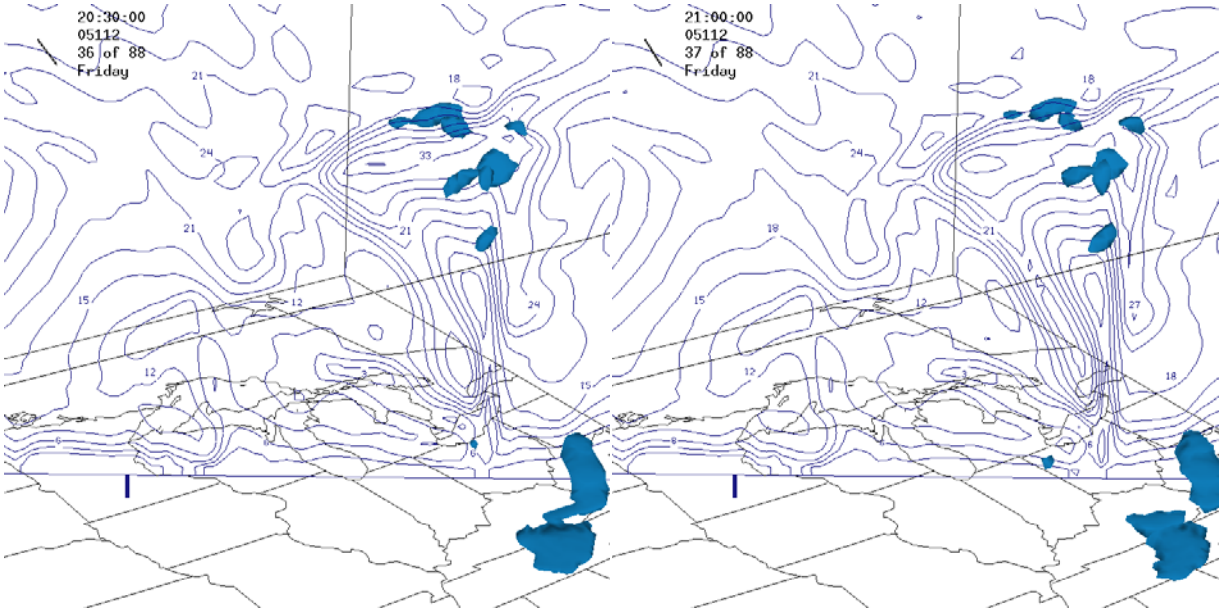

Figure 13. UWNMS simulation of Case 2 initialized at 00 UTC on 22 April 2005 showing the relationship between inertial instability and jet wind speed increase (inertial flare-up). Top left panel shows a cross section of total wind speed (dark blue contours, 3 m/s) and an isosurface of inertial instability (blue isosurface, -1.5 PVU) at 1630 UTC on 22 April 2005.

A minor inertial flare-up is evident with a jet core of 15 m/s. Top right panel (same as in top left) at 2000 UTC on 22 April 2005, a more intense inertial flare-up at 30 m/s is evident as more organized areas of inertial instability are present on the anticyclonic shear side of the jet. Bottom left (same as in top left and top right) at 2030 UTC on 22 April 2005 inertial instability continuing to affect the anticyclonic shear side of the jet maintaining a 36 m/s wind speed. Bottom left (same as in top left, top right, and bottom left) at 2100 UTC on 22 April 2005 inertial instability leaving the plane of the cross section and jet core wind speed reduced to 30 m/s.

exhibits the same intensification. Fig. 13 (bottom left and bottom right) show a continual upward flow of inertially unstable air at less than -2 PVU displaced poleward on the anticyclonic shear side of the jet. This persistent movement toward the pole subsequently increases and continues to enhance the smaller scale westerly jet. This finding can be compared to Dunkerton and Scott (2007) as they found a relation between absolute angular momentum and PV and a tendency to produce westerly jets of approximately equal magnitude extending to polar latitudes. Using a

numerical model they suggested that an upscale energy cascade triggered by small scale forcing can lead to westerly jets. Here it was found that upward vertical motion lifts and displaces inertially unstable air poleward several degrees, increasing wind speeds through conservation of angular momentum.

Similar to Case 1, a large departure from geostrophic balance is evident in Case 2 through inertial instability on the anticyclonic shear side of the jet. Once again imbalances between the PGF and the Coriolis force, which are evident as large areas of inertial instability in Fig. 14, as air flows through the jet streak creates upper air divergence in the right entrance region and left exit region. This enhanced divergence creates a localized area of increased wind speed within the jet resulting in an inertial-flare-up. The inertial flare-ups in Case 2 are unique with respect to their size and strength since there is no well defined jet as there was in Case 1. Case 2 features smaller inertial flare-ups that form and dissipate quickly (Fig. 14) as divergence is enhanced in quadrant 1 through the areas of inertial instability of -2 PVU (Fig. 14, blue shading on anticyclonic shear side of the jet). As plumes of vertical motion continue to lift these areas of inertial instability from the surface cold front to the anticyclonic shear side of the jet, a notable inertial flare-up is evident. Once the vertical motion dissipates and is no longer interacting with the inertial instability at the surface, the inertial flare-ups dissipate as well.

Once again upper air divergence is enhanced through inertial instability and geostrophic adjustment. This can be seen in Figure 14 as areas of divergence on the anticyclonic shear side of the jet are enhanced through inertial instability. Each panel of Fig. 14 shows that a 36 m/s jet core wind speed is maintained through inertial instability induced divergence. These areas of inertial instability, which represent a large departure from geostrophic balance, are the

underlying cause of enhanced divergence in the right entrance and left exit region and the main contributor to the inertial flare-ups associated with Case 2.

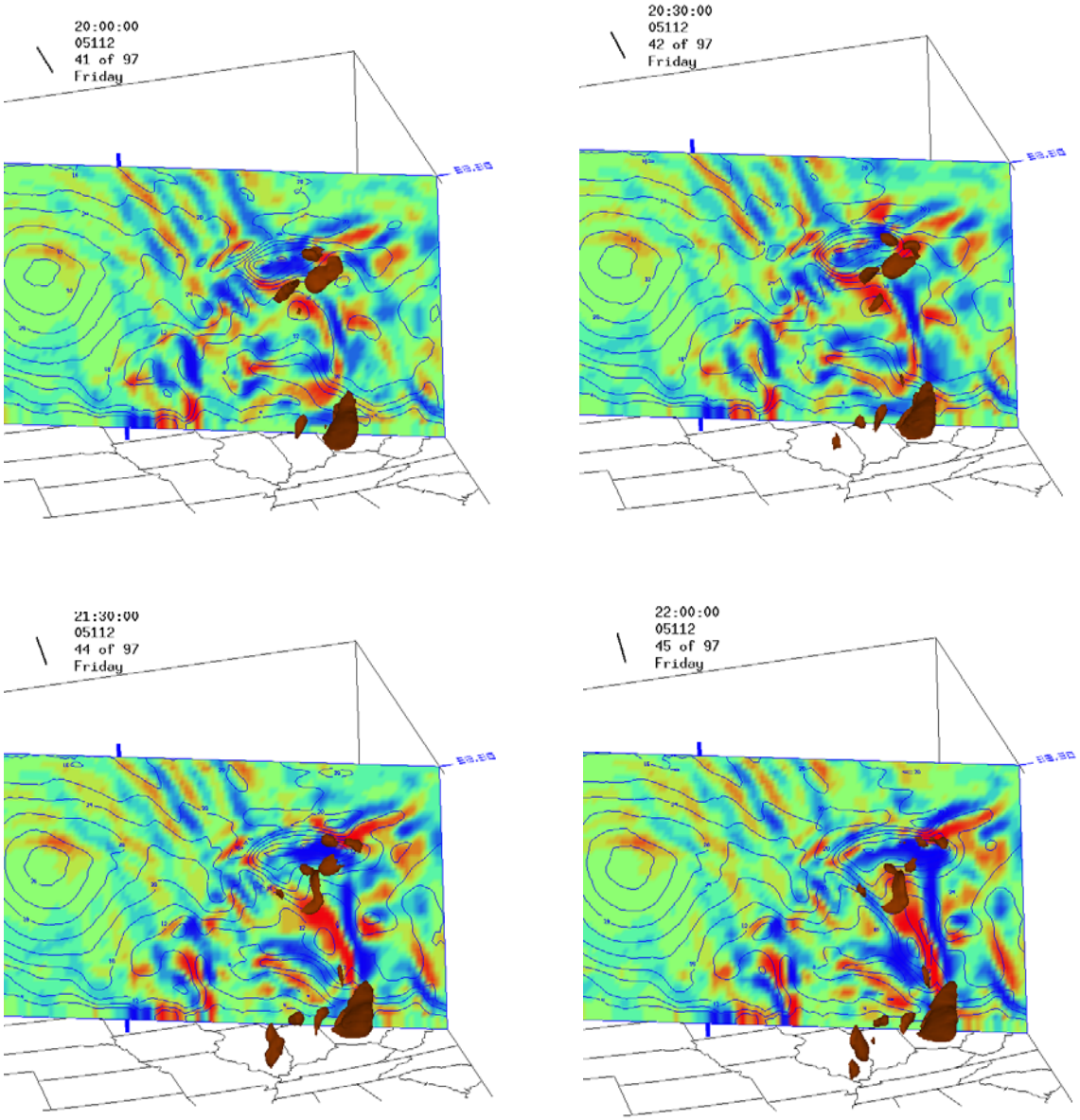

Figure 14. UWNMS simulation of Case 2 initialized with ECMWF data on 00 UTC 22 April 2005 showing the relationship between inertial instability and enhanced divergence associated with jet wind speed increase. Top left panel shows a cross section of wind speed (blue contours, 4 m/s) isosurface of inertial instability (brown shaded isosurface,-1.5 PVU) and convergence (red shading) divergence (blue shading) patterns at 2130 UTC 22 April 2005. As inertially unstable air interacts with the anticyclonic shear side of the jet, the divergence is enhanced resulting in a tightening of the isotachs and increased wind speed. At 2030 UTC (top right panel, shading the same as in top left panel) wind speed is

enhanced as inertial instability creates an area of increased divergence (blue shading). At 2130 UTC (bottom left panel, shading the same as in top left and top right panel) a continuation of enhanced divergence is evident as inertially unstable air continues to affect the anticyclonic shear side of the jet, resulting in a tightening of the isotachs. At 2200 UTC (bottom left panel, shading the same as in top left, top right, and bottom left panel) shows a continual interaction between inertial instability, enhanced divergence and a local wind speed maximum (inertial flare-up).

To better exemplify the concept that negative EPV and inertial instability are the two main contributors to the enhancement of upper level divergence and an overall increase in westerly jet speeds, an analysis of absolute vorticity is essential. Figure 15 shows a comparison of absolute vorticity, divergence, negative EPV, and jet wind speeds for Case 2. With a side

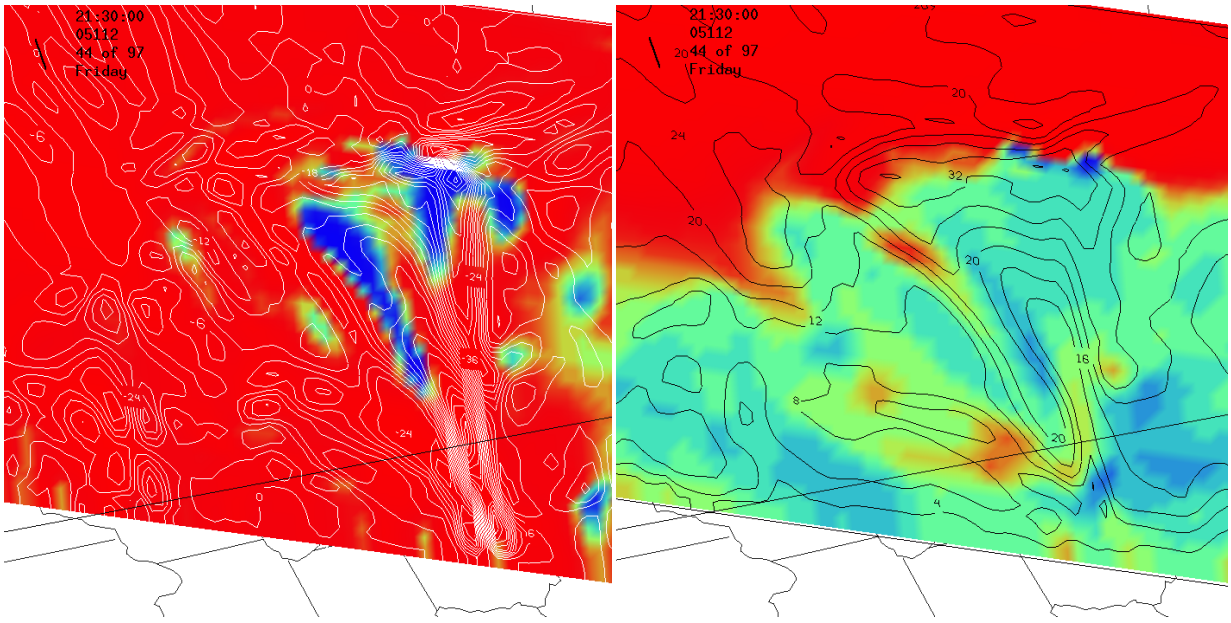

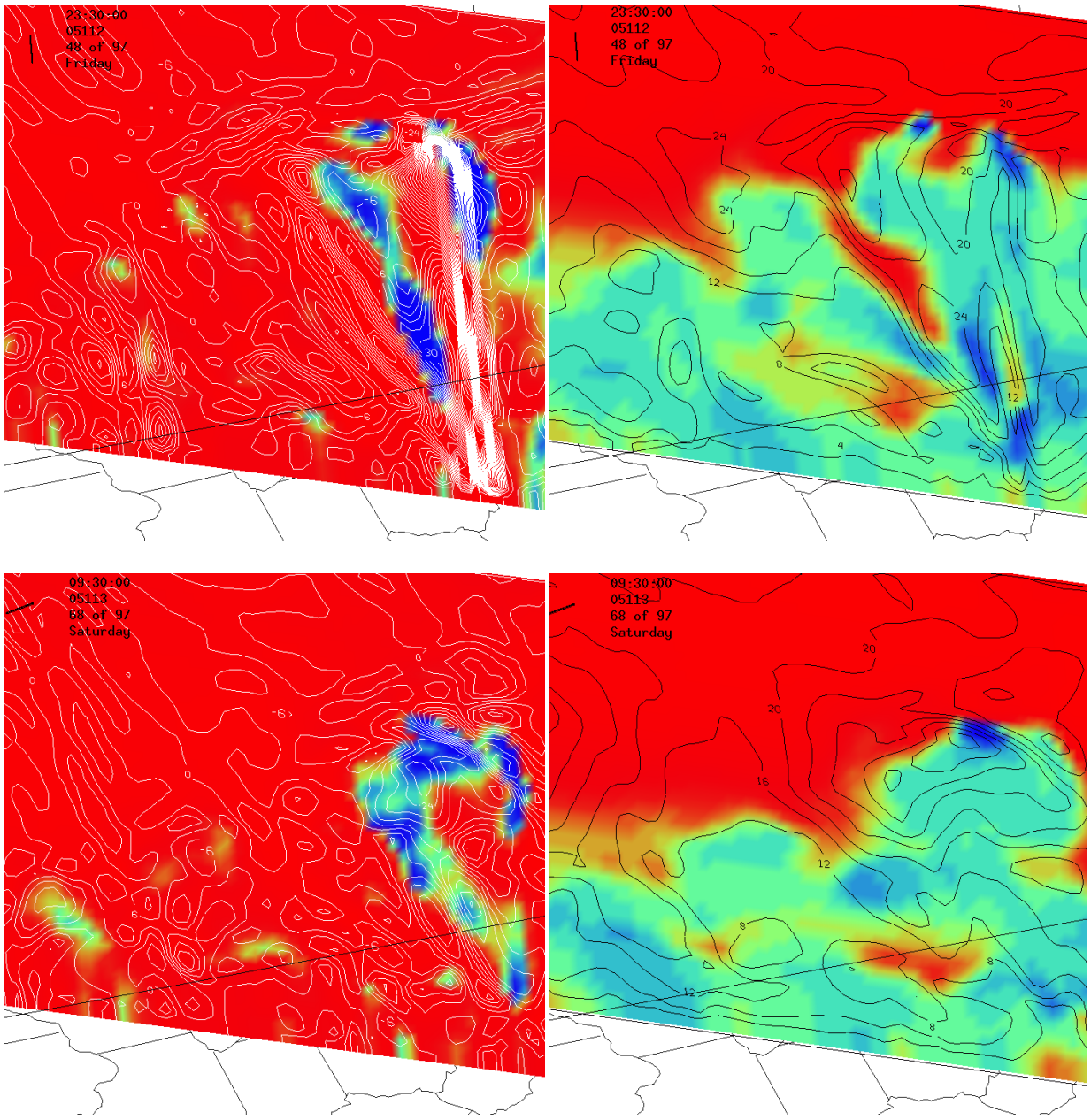

Figure 15. UWNMS simulation of Case 2 initialized with ECMWF data on 00 UTC 22 April 2005 showing the relationship between negative absolute vorticity, divergence, negative EPV and a tightening of the isotachs. Left panels show absolute vorticity, (blue shading is negative, red shading is positive), and divergence (white contours, interval 5 x 10^{-5} s^{-1}). Right panels show negative EPV (blue shading is negative, red shading is positive) and jet wind speeds (black contours, every 4 m/s). Top panels are at 2130 UTC on 22 April 2005. Middle panels are at 2330 UTC 22 April 2005. Bottom panels are at 0930 UTC 23 April 2005.

by side comparison it is clear that all of the aforementioned dynamical variables play a crucial role in midlatitude westerly jet speed enhancements. Inertial instability creates upper-air divergence in the left exit region, which leads to a decrease in absolute vorticty, which then creates a localized inertial flare-up. Figure 15 shows this process as the blue shaded regions correspond to negative absolute vorticity and are complemented by areas of divergence (left panels). Through Fig. 15 it can also be shown that these areas of negative absolute vorticity and divergence coincide perfectly with the negative EPV anomalies and the sudden inertial flare-up (right panels). Fig. 15 groups together these essential dynamical quantities to illustrate the unequivocal influence that negative EPV has on the process of producing an inertial-flare-up.

5.4. Case 3

The third and final case presented here illustrates dynamics similar to that of Cases 1 and 2 in that inertial instability is the focal point with respect to the generation and maintenance of inertial flare-ups. As air with low inertial instability along the surface cold front is displaced poleward via vertical motion and is transported to a higher latitude. With this poleward transport of about 2 degrees, momentum is once again transferred into the jet. With this momentum transfer an increase in jet core wind speed is evident. Figure 16 (top left panel) shows this process as at 0930 UTC a relaxed jet is evident in the westernmost portion of this northwest-southeast cross section. Fig. 16 (top right panel) shows that five and a half hours later at 1500 UTC an inertial flare-up is seen with a 36 m/s jet core wind speed increase. This negative EPV originating at a lower latitude is displaced about 3 degrees toward the pole. The momentum is then transferred into the jet resulting in an increase in jet wind speeds. Fig. 16 (bottom left panel) shows an inertial flare-up at 1530 UTC, maintaining a 36 m/s jet core, resulting from the

momentum transfer associated with this negative EPV anomaly. Once the negative EPV anomalies move through the plane of the cross section and before more are generated through the surface cold front and associated vertical motion, a distinct relaxation of the jet is evident. Fig. 16 (bottom right panel) shows a 21 m/s jet at 1800 UTC. No areas of inertial instability are crossing the plane of the cross section, resulting in a 15 m/s reduction in wind speed in two and a half hours.

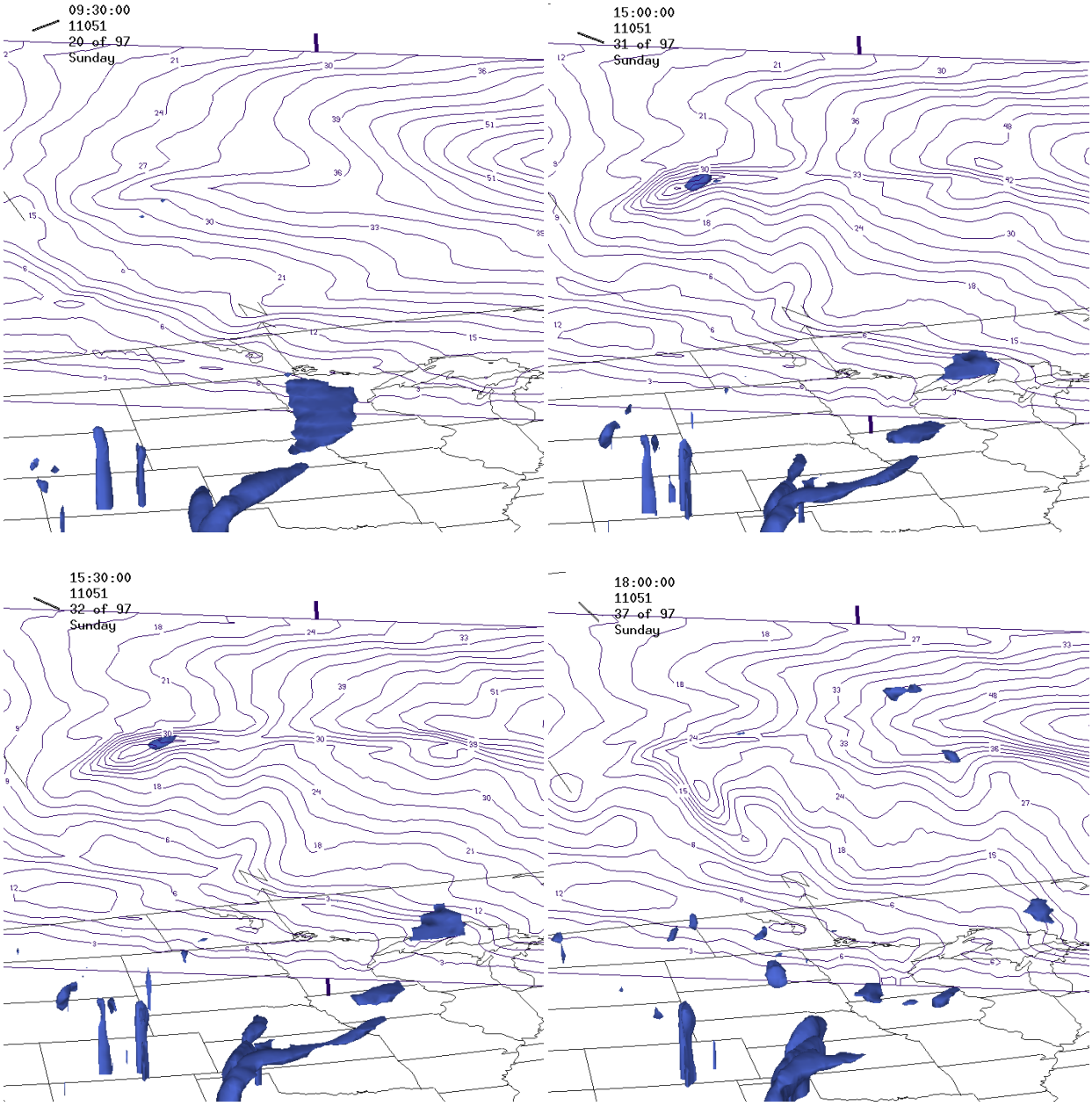

Figure 16. UWNMS simulation of Case 3 initialized at 00 UTC on 21 February 2011 showing relationship between inertial instability and jet wind speed increase (inertial flare-up). Top left panel shows a cross section of wind speed (dark blue contours, 3 m/s) and an isosurface of inertial instability (blue isosurface, -1.5 PVU) on 9300 UTC on 21 February 2011. No flare-ups are evident as inertial instability has not crossed the plane of the cross section. Top right panel (same as in top left panel) at 1500 UTC a 40 m/s jet wind speed is evident as inertial instability interacts with the anticyclonic shear side of the jet. Bottom left panel (same as in top left, top right, and bottom left panels) at 1530 UTC another jet speed maximum is evident.

Bottom right panel (same as in top left, top right, and bottom left) at 1800 UTC inertial instability no longer in the plane of the cross section and no inertial flare-ups are evident.

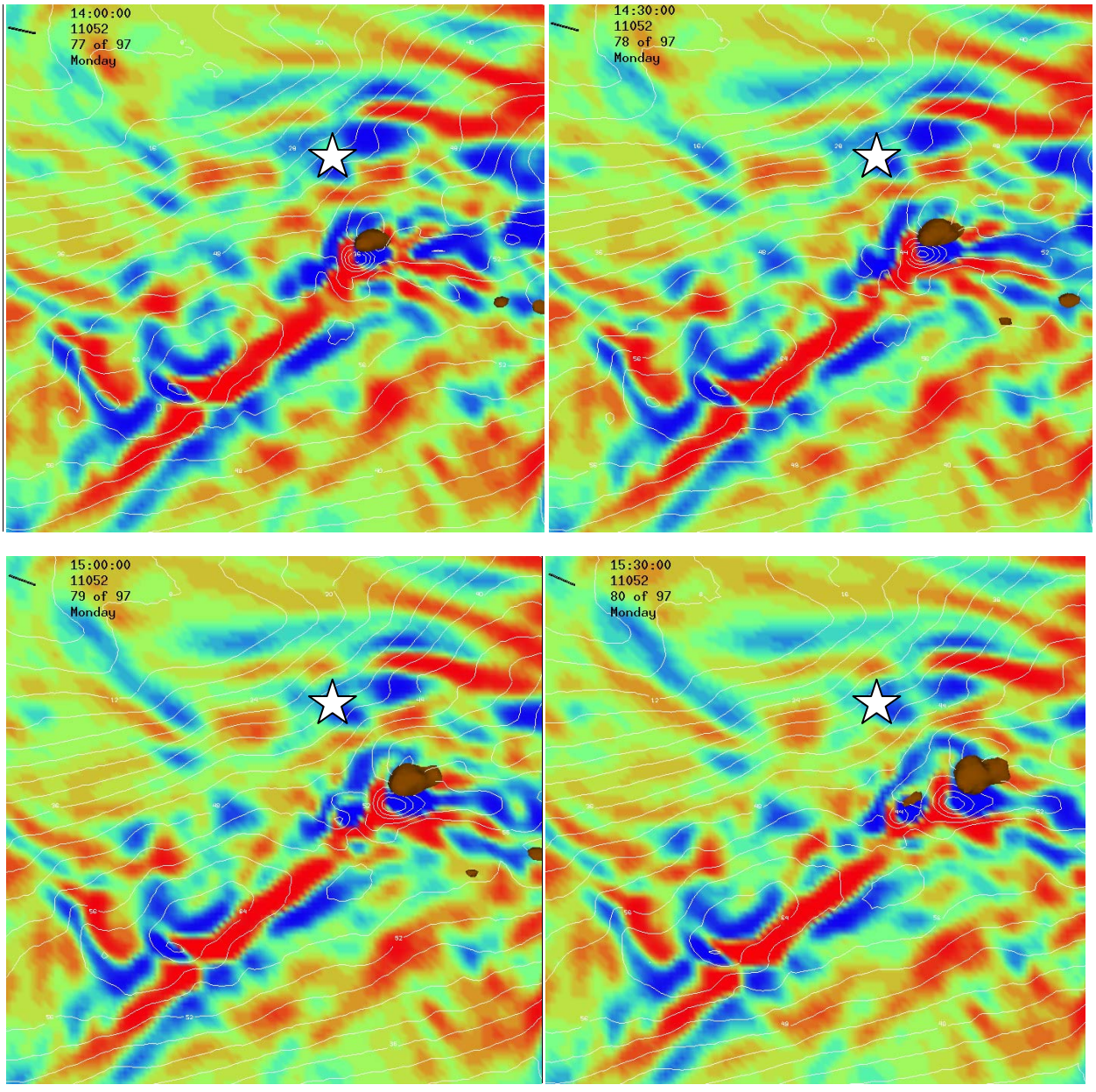

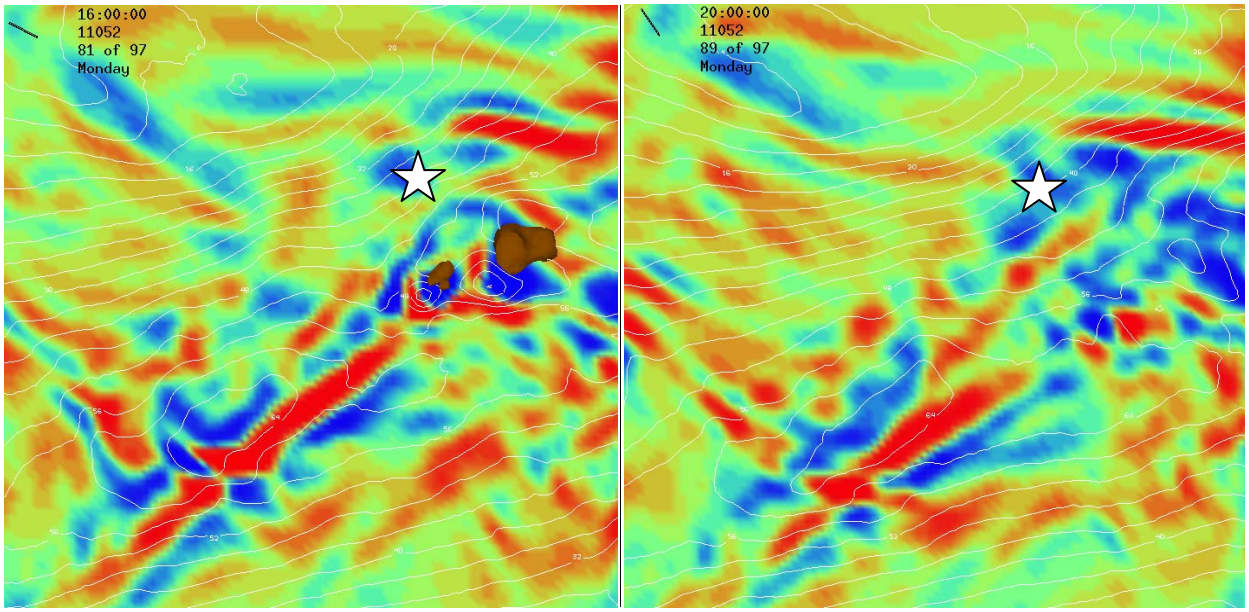

Figure 17. UWNMS simulation of Case 3 initialized with ECMWF data on 00 UTC 20 February 2011showing the relationship between inertial instability and enhanced divergence associated with jet core wind speed increase in a horizontal map view at 13 km. The star indicates the location of Madison, WI. Top left panel (and all panels in this figure) shows a horizontal map at 13 km of wind speed (white contours, 4 m/s) isosurface of inertial instability (dark brown, -1.5 PVU) convergence (shaded in red) and divergence (shaded in blue) at 1400 UTC 21 February 2011. As inertially unstable air enhances the divergence in the jet, a distinctive tightening of the isotachs occurs. At 1400 UTC (top left panel) a 40 m/s inertial flare-up is evident as divergence is enhanced through interaction with inertial instability. At 1430 UTC (top right panel) a 52 m/s inertial flare-up is shown. At 1500 UTC (middle right panel) a 64 m/s jet core wind speed is shown. At 1530 UTC (middle right panel) a 64 m/s jet core wind speed is maintained through enhanced divergence. At this time note a new inertial flare-up at 44 m/s just to the west of the 64 m/s flare-up. At 1600 UTC (bottom left panel) the new inertial flare-up now at 52 m/s due to enhanced divergence from the anomalous inertial instability. At 2000 UTC (bottom right panel) a relaxed jet is shown with no notable inertial flare-ups as anomalous inertial instability is not in the horizontal plane of this plot.

Areas of inertial instability as seen in Case 3, play an important role in jet dynamics, as divergence is enhanced through strong areas of negative EPV, especially on the anticyclonic shear side of the jet. Figure 17 shows this process in half hour time steps (except for bottom right) as inertial instability causes an imbalance between the PGF and the Coriolis force as air flows through the jet, creating upper air divergence in the left exit region. Fig. 17 (top left panel) shows a distinct inertial flare-up at 1400 UTC on 21 February 2011 with a jet core wind speed of 40 m/s. This area of negative EPV accelerates upper air divergence in the left exit region (blue shading) which is consistent with geostrophic imbalance. Fig. 17 (top right panel) at 1430 UTC shows a jet core inertial flare-up of 52 m/s, a 12 m/s increase in one half hour. Once again strong divergence enhanced by negative EPV is evident on the anticyclonic shear side of the jet and is responsible for the sudden speed increase. At 1500 UTC (Fig. 17 middle left panel) a 64 m/s inertial flare-up is shown. Another 12 m/s wind speed increase in one half hour is caused by continual upward driven negative EPV anomalies which continue to create enhanced divergence on the anticyclonic shear side of the jet. At 1530 UTC (Fig. 17 middle right panel) another region of negative EPV begins to affect the area just to the west of the initial inertial flare-up. Once again an area of enhanced divergence is evident along with a sudden 44 m/s inertial flare-up. At 1600 UTC (Fig. 17 bottom left panel) the newly formed inertial flare-up has increased wind speed to 56 m/s which is another 12 m/s wind speed increase in one half hour. Once the areas of negative EPV move out of the horizontal plane at 2000 UTC a relaxed jet is shown in Fig. 17 (bottom right panel) with no inertial flare-up regions.

Fig. 17 also reveals an important dynamical mechanism with respect to climate dynamics and the momentum budget of the stratosphere. The horizontal convergence/divergence patterns at 13 km in Fig. 17 reveal gravity waves patterns that are associated with the anomalous regions

of inertial instability. In all cases presented here, gravity waves were evident in the convergence/divergence patterns (not shown in cases 1 and 2). Although gravity waves are not the primary focus of this research, it is important to note a possible mechanism by which gravity waves may be generated. This requires in depth study and could be crucial to the global momentum transport budget.

To further exemplify the process of jet intensification through the presence of negative EPV on the anticyclonic shear side of the jet, an analysis of absolute vorticity, divergence, EPV, and jet wind speeds are necessary. Figure 18 shows these variables in three distinctive times during the eastward migration of the midlatitude storm. As in Cases 1 and 2, Case 3 shows

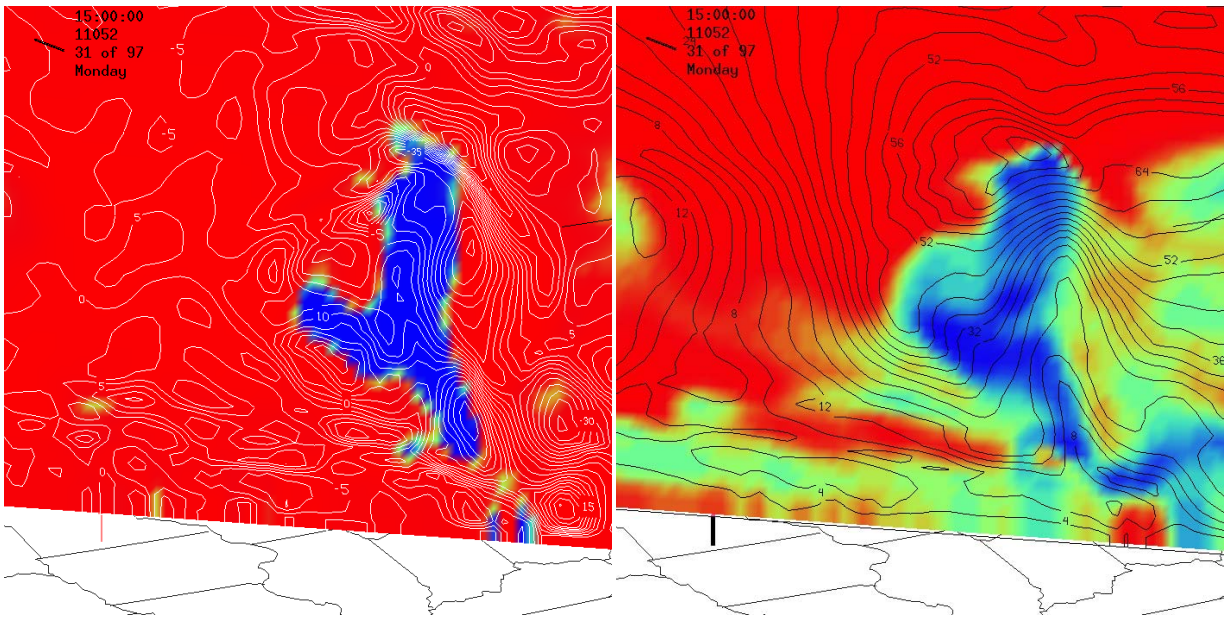

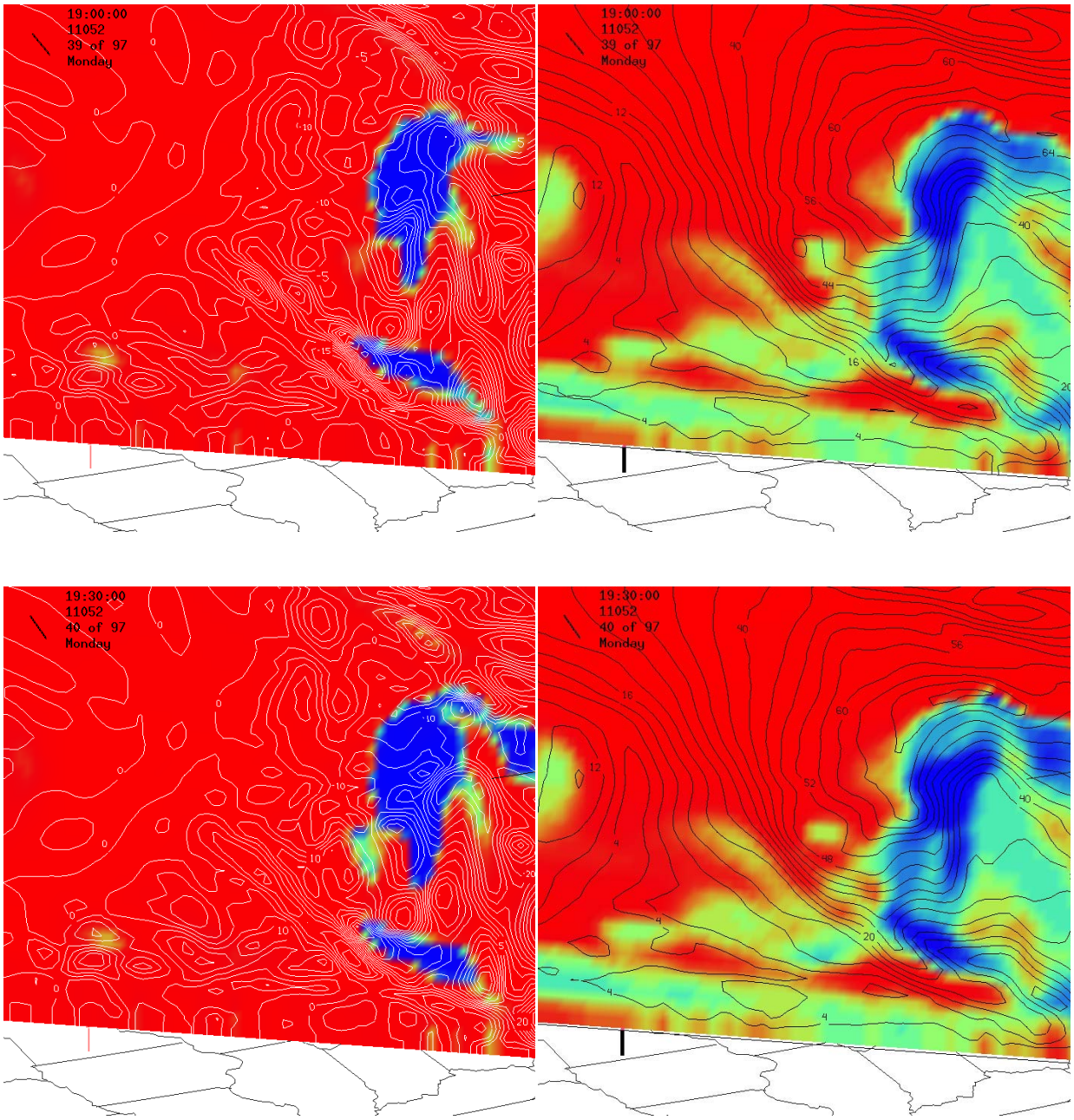

Figure 18. UWNMS simulation of Case 3 initialized with ECMWF data on 00 UTC 21 February 2011 showing the relationship between negative absolute vorticity, divergence, negative EPV and a tightening of the isotachs. Left panels show absolute vorticity, (blue shading is negative, red shading is positive), and divergence (white contours, interval 5 x 10^{-5} s^{-1}). Right panels show negative EPV (blue shading is negative, red shading is positive) and jet wind speeds (black contours, every 4 m/s). Top panels are at 1500 UTC on 21 February 2011. Middle panels are at 1900 UTC 21 February 2011. Bottom panels are at 1930 UTC 21 February 2011.

very similar results. Through Fig. 18 a complete connection of all the aforementioned variables is made as a positive feedback loop is started due to the existence of inertial instability of the anticyclonic shear side of the jet. Fig. 18 (right panels) shows negative EPV (blue shading) near the anticyclonic shear side of the jet. This corresponds very well with the negative absolute vorticity (blue shading) and divergence (white contours) in Fig. 18 (left panels). The negative EPV creates upper air divergence in the left exit region. Finally this enhanced divergence, in the left exit region, creates a distinct tightening of the isotachs, or an inertial flare-up.

6. Meridional Circulation patterns along the jet

6.1. History of circulation patterns and STE near jets

Namias and Clapp (1949) explained the formation of jet streams using quasi-geostrophic theory. They explained that in order to produce an increase in vertical wind shear, a thermally direct vertical circulation must be set up. Years later, Sawyer (1956) studied how the resulting vertical circulation can be calculated using quasi-geostrophic theory. Then Eliassen (1962) analyzed quasi-geostrophic theory and applied it to transverse circulations in fronts caused by variations temperature and geostrophic wind along the frontal zone. He also used this method to study transverse circulations in jet streams by focusing on the forcing term Q, which measures static stability, baroclinicity, and absolute vorticity, all of which are assumed to be positive. Eliassen (1962) formed a diagnostic equation for meridional streamfunction, ψ, by requiring the vertical motion field to satisfy the thermal wind law in steady state. A vital assumption is that there is static and inertial stability. Note that $f - \frac{\partial U}{\partial y}$ appears in the denominator on the right hand side.

$$\left[\frac{\partial}{\partial m}\left(\delta\frac{\partial\psi}{\partial m}\right)\right]_p + \left(\frac{\partial^2\psi}{\partial p^2}\right)_m = \frac{Q}{f-\frac{\partial U}{\partial y}} \qquad (7)$$

where p is pressure, $\delta = \gamma\left(\frac{\partial\theta}{\partial p}\frac{\partial m}{\partial y} - \frac{\partial\theta}{\partial y}\frac{\partial m}{\partial p}\right)$, m = U – fy, and $\gamma = \frac{R}{fp_o}\left(\frac{P_o}{P}\right)^{\frac{C_v}{C_p}}$, and

$$Q = -2\frac{\partial U}{\partial p}\frac{\partial U}{\partial X} - 2\frac{\partial V}{\partial p}\frac{\partial U}{\partial y} - \gamma\frac{\partial}{\partial y}\frac{D\theta}{dt} \qquad (8)$$

Eqn. (8) is elliptical when $\delta > 0$, i.e inertially and statically stable. Although this equation is generally used for areas involving frontal boundaries, Eliassen (1962) also included a dry adiabatic case:

$$Q = 2\left(\frac{\partial U}{\partial p}\frac{\partial V}{\partial y} - \frac{\partial U}{\partial y}\frac{\partial V}{\partial p}\right) = -2\gamma\left(\frac{\partial U}{\partial x}\frac{\partial\theta}{\partial y} - \frac{\partial U}{\partial y}\frac{\partial\theta}{\partial x}\right) \qquad (9)$$

The quantity Q is then integrated over a region σ in (y, p) bounded by a closed contour S to analyze transverse circulations in jet streams

$$\int_\sigma Q\,dy\,dp = -2\oint_S U dV. \qquad (10)$$

The distribution of Q in the jet stream will usually have the characteristic of a doublet. The resulting transverse circulation will possess two circulation cells with opposite rotation on the lower half and the upper half of the jet stream, an example of one possible configuration is shown in Figure 19.

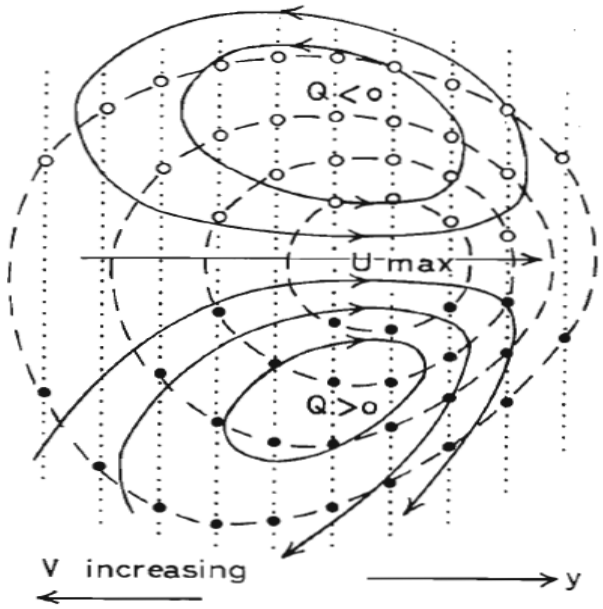

Figure 19. Transverse circulation in the vicinity of an idealized jet core. Dashed lines are U isotachs, dotted lines are V isotachs, and solid lines are streamlines of transverse circulation. Taken from Eliassen (1962).

This represents a highly idealized case as Q is positive below the jet core and negative above it. As a result, a transverse circulation forms two direct circulation cells which is shown by the solid lines in Fig. 19. This idealized case from Eliassen (1962) does explain the opposing circulation patterns in midlatitude westerly jets, however in the research presented here, latent heating, negative EPV, and negative absolute vorticity are the three major contributors to the inertial flare-ups within the jet. Eliassen (1962) removes latent heating from his forcing equation and assumes absolute vorticity to be postitive. It is proposed in this chapter that EPV alters the jet dynamics in a significant manner.

Shapiro (1981) reiterates the fact that the solution to Sawyer (1956) and Eliassen (1962) forcing equation (eqs. 7, 8, 9, and 10) requires that the potential vorticity be greater than zero.

This ensures that the equation is elliptical and solvable with suitable boundary conditions. Therefore, Shapiro (1981) used a Richardson number criterion for the onset of inertial instability:

$$\mathrm{Ri} = -f\gamma \frac{(\partial\theta/\partial p)}{(\partial m/\partial p)^2} = -f(\partial m/\partial y)^{-1} \qquad (11)$$

with the forcing term of the Sawyer - Eliassen equation Q_1 being

$$Q_1 = -2\gamma \frac{\partial U}{\partial X}\frac{\partial \theta}{\partial y} = 2\gamma \frac{\partial V}{\partial y}\frac{\partial \theta}{\partial y}. \qquad (12)$$

The geostrophic stretching deformation can be used to quantify the thin filaments or sheets of stratospheric air that reach down into the troposphere.

The work presented here analyzes jet circulation and intensification from the view that inertial instability helps to control the local circulation. Sawyer and Eliassen's equation can diagnose meridional circulations, but not necessarily poleward and downward over the jet, as seen in aircraft and data simulations.

Shapiro (1974) also diagnosed regions of STE inferred from research aircraft data and aerological soundings. Regions of stratospheric intrusions as seen in Figure 20 and 21 reveal similar features to the case studies presented in this thesis (Figs. 6, 15, 22, 25, 26, 27). Through this aircraft data it was found that upper-level jet-front systems are a preferred region of turbulent scale motions and clear air turbulence (CAT), and thus STE. Similar finding involving the existence of STE were found in Shapiro (1976, 1978). He found that the vertical gradient of diabatic temperature change resulting from vertical, shear induced, turbulent temperature flux in the layers of CAT were responsible for the large PV values that mix into the stratosphere.

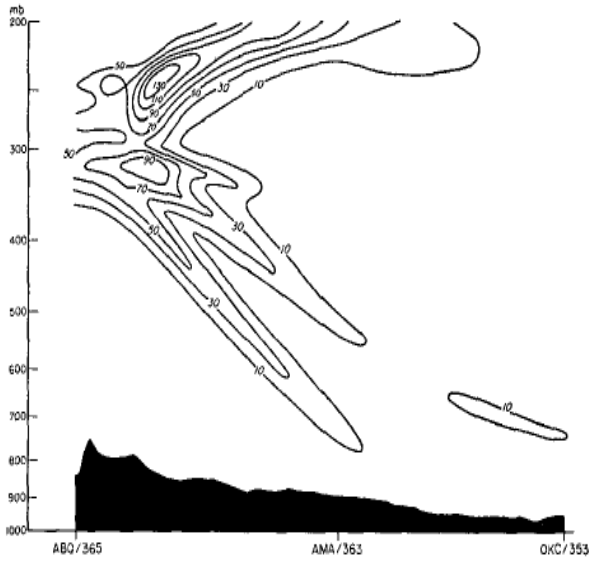

Figure 20. Cross section of potential vorticity (10^{-6} sec^{-1} °K mb^{-1}). Taken from Shapiro (1974). Potential vorticity contours are similar to that of Fig. 5 middle right panel and Fig. 15 (middle right panel).

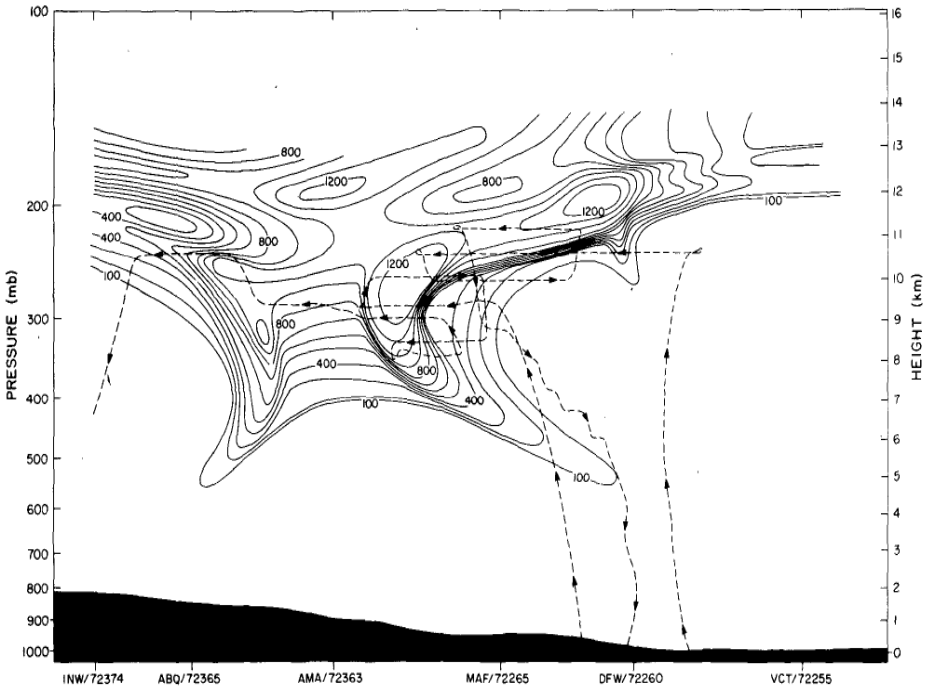

Figure 21. Cross section of potential vorticity (10^{-7} K s^{-1} mb^{-1}). Taken from Shapiro (1978). Note the potential vorticity contours are similar to Fig. 24 middle left panel.

Given the relative lack of knowledge of meridional circulation around jets, a set of "Eulerian sections" transverse to the jet are compared for the jet entrance, middle, and exit regions of an instantaneous jet for each case. Then "Lagrangian sections" are explored following the motion of the most inertially unstable regions for each case. Here, a Lagrangian and Eulerian perspective will be analyzed in all three cases to get a better understanding of the role that negative EPV has on jets and the evolution of STE in the vicinity of jets in the presence of negative EPV.

6.2. Eulerian sections

6.2.1. Case 1

To see how the meridional circulation varies along the jet a specific time was chosen when EPV is the most negative within the jet. Figure 22 shows cross sections of negative EPV and streamfunction taken along the polar and subtropical jet at 0330 UTC on 6 February 2008. It is evident that the flow is interrupted by these anomalous

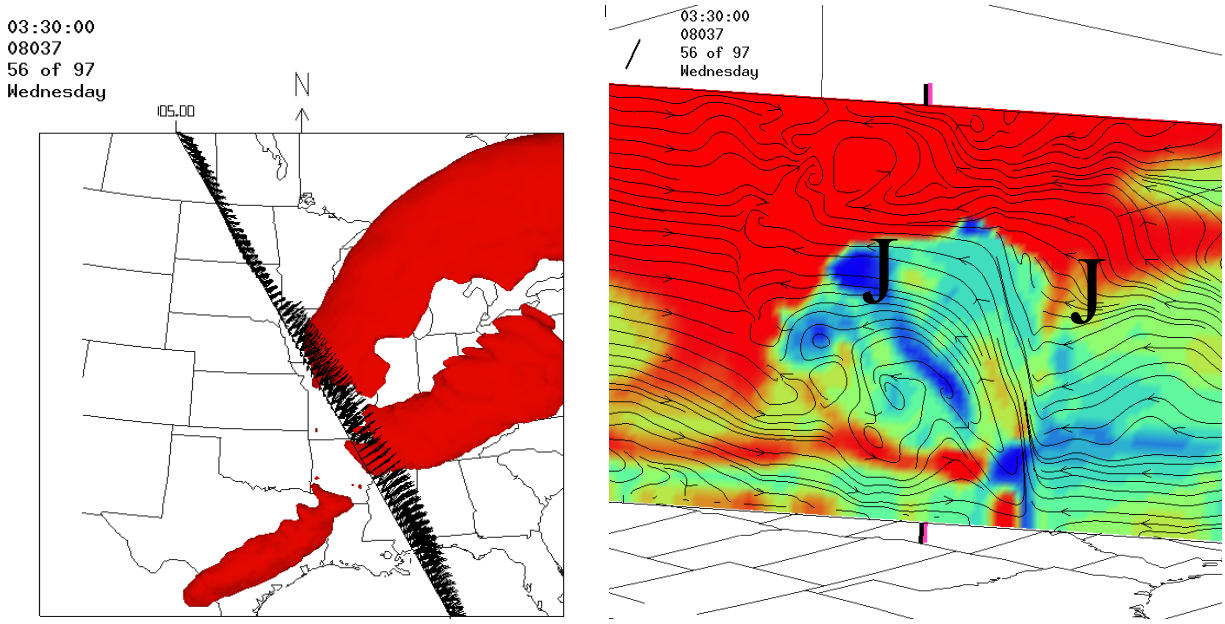

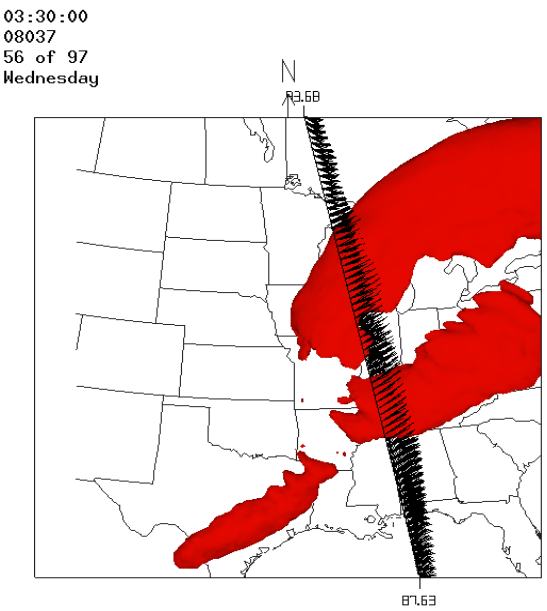
03:30:00
08037
56 of 97
Wednesday
N
83.68
87.63

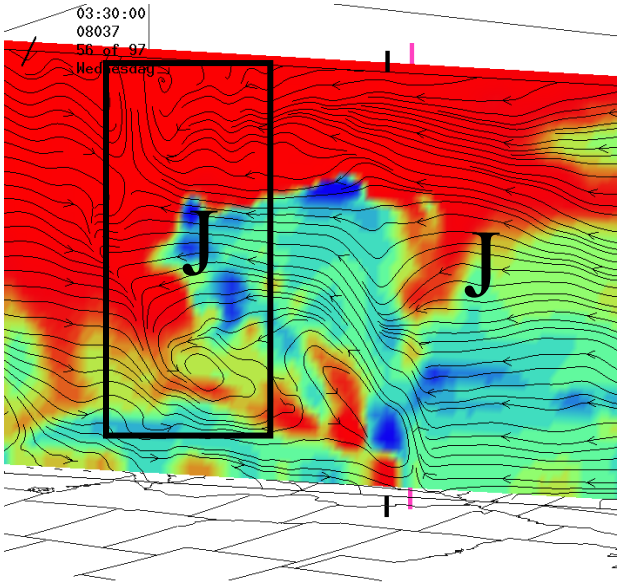
03:30:00
08037
56 of 97
Wednesday
J
J

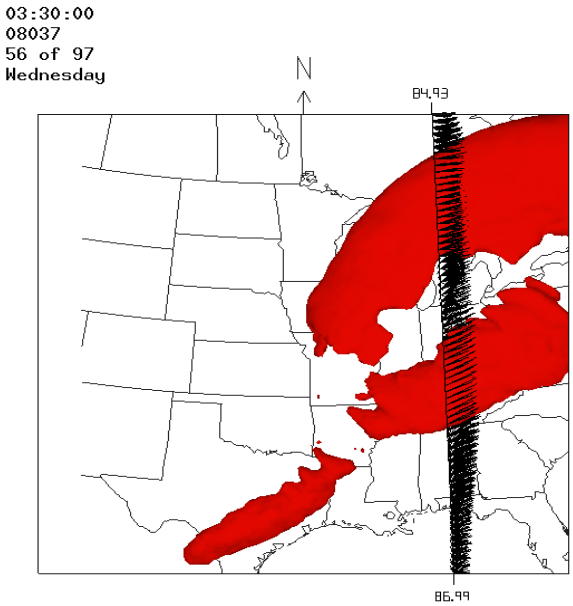
03:30:00
08037
56 of 97
Wednesday
N
84.93
86.99

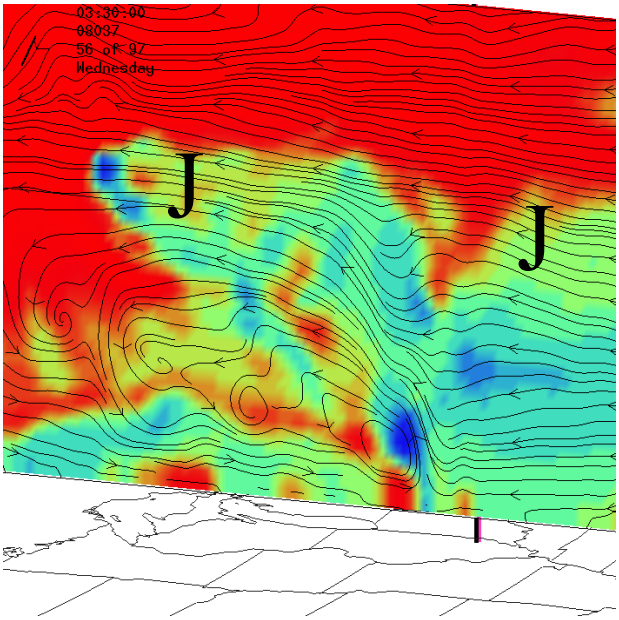
03:30:00
08037
56 of 97
Wednesday
J
J

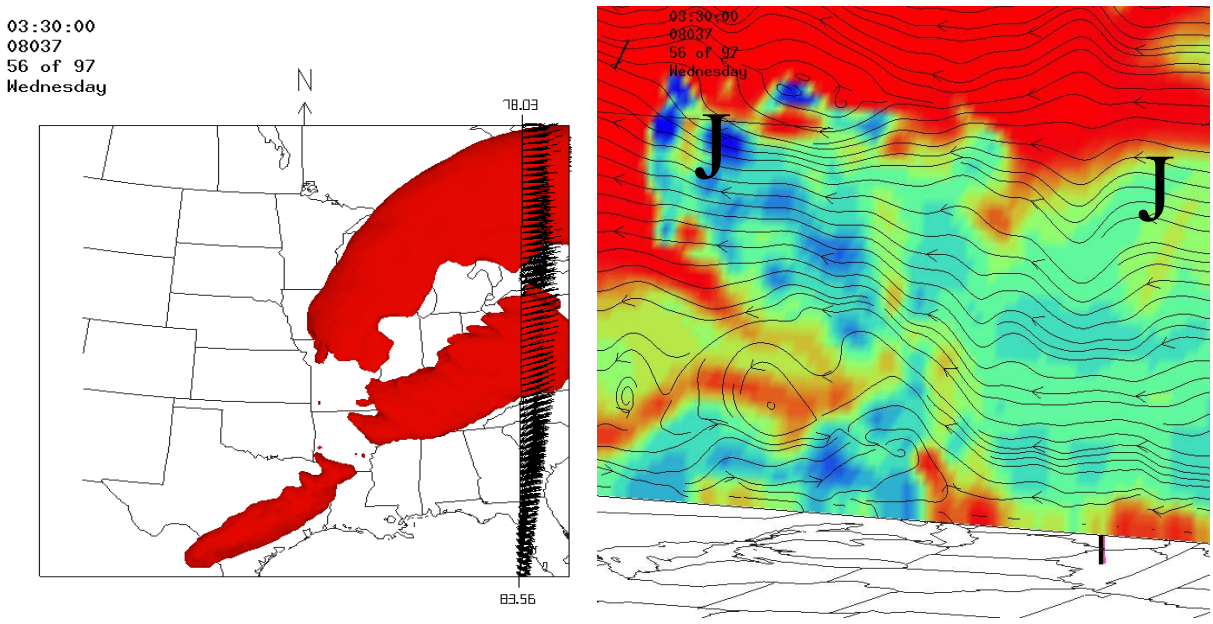

Figure 22. Eulerian cross sections for Case 1 at 0330 UTC on 6 February 2008. Left panels show an isosurface of jet at 60 m/s and the black line shows where the cross section occurs along the jet. Right panels show negative EPV (red shadings is positive EPV and blue shadings is negative) and streamfunction (black contours). Black J indicative of jet max at 60 m/s. Black box reveals Sawyer-Eliassen circulation as described in text.

areas of negative EPV (blue shadings). It is evident through analyzing the streamfunction contours (black contours) that a distinct poleward and downward circulation pattern develops associated with these regions of negative EPV. Although this circulation is revealed through analyzing the streamfunction pattern at every point along the jet in Fig. 22, it is most apparent in Fig. 22 (third row left panel) as many distinct rotors spiral poleward and downward around the jet deep into the troposphere. It is through this analysis of streamfunction that the Sawyer-Eliassen circulation is revealed as well. In Fig. 22 (second row, right panel) a black box is drawn around the opposing circulation patterns above and below the jet maximum. The Sawyer-Eliassen circulation is not evident in each image in Fig. 22 as it is inertial instability that helps to control the local circulation. It has been shown once again through Eulerian cross sections of

stream function that negative EPV alters jet circulation patterns and induces a very distinct STE mechanism in westerly jets.

6.2.2. Eulerian sections - Case 2

Using the same technique as in Case 1, Case 2 is analyzed and it is again apparent how negative EPV alters circulation patterns. Figure 23 shows cross sections of negative EPV and streamfunction at 0230 UTC on 22 April 2005 along a rather weak polar jet in comparison to Case 1. Each section of the jet uncovers a poleward and downward surge of high PV stratospheric air (red shading) wrapping around the jet as well as distinct circulation patterns discovered in the streamfunction patterns (black contours). Each section of the jet, when exposed to negative EPV values shows a

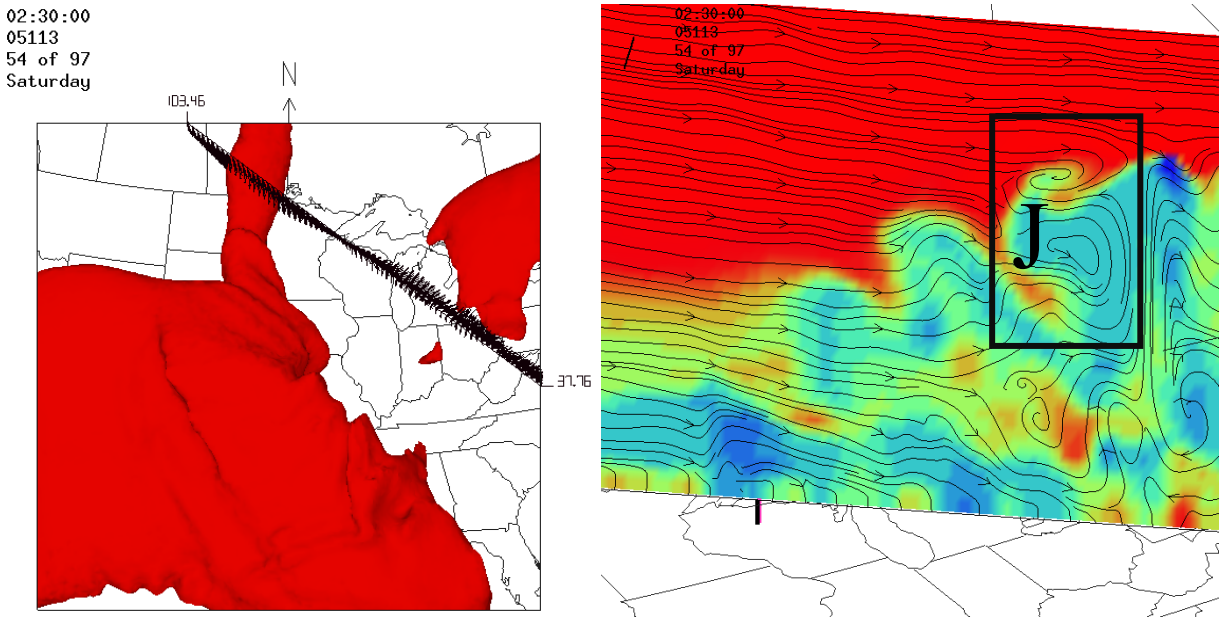

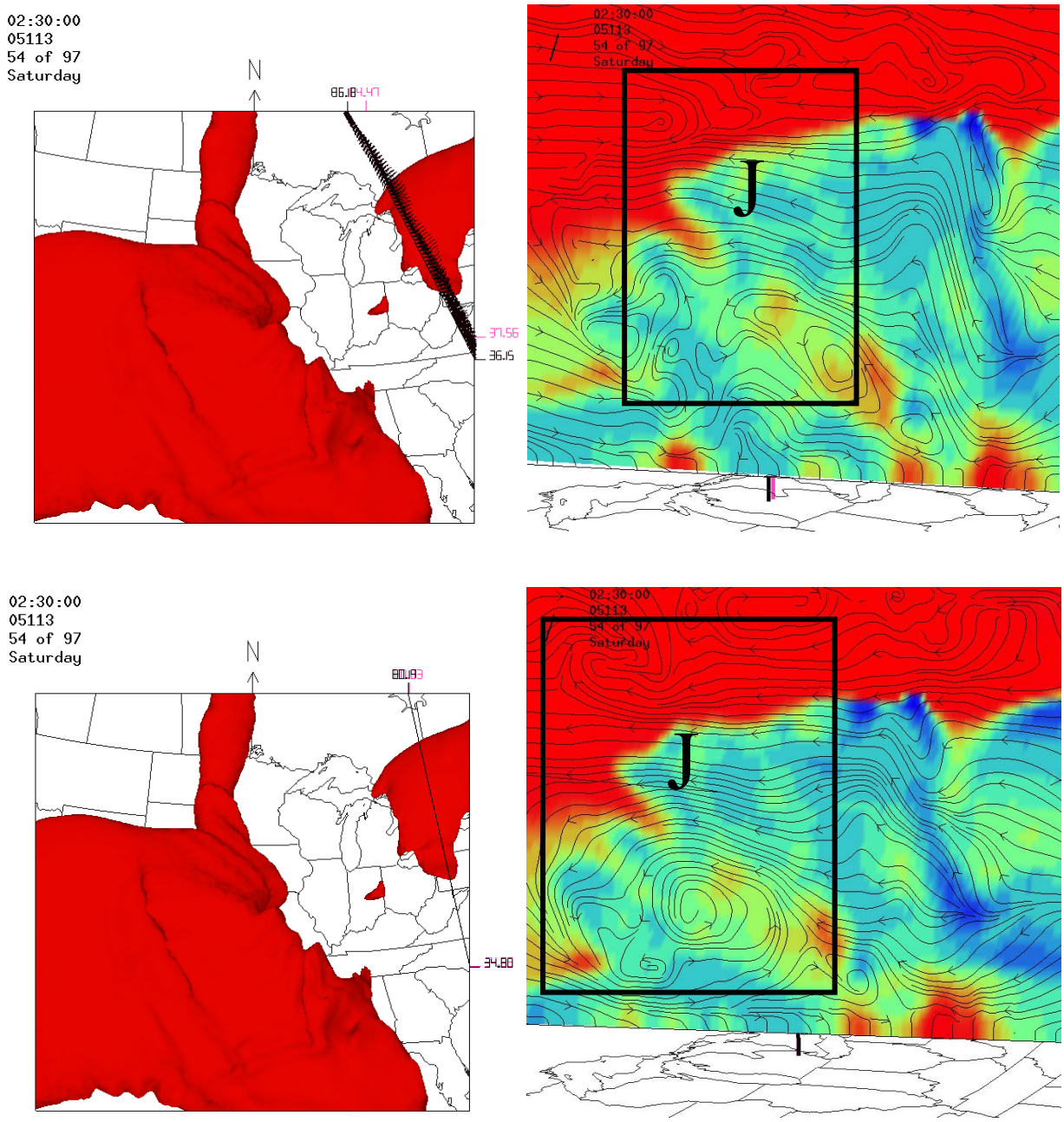

Figure 23. Eulerian cross sections for Case 2 at 0230 UTC on 22 April 2005. Left panels show an isosurface of jet at 40 m/s and the black line shows where the cross section occurs along the jet. Right panels show negative EPV (red shadings is positive EPV and blue shadings is negative) and streamfunction (black contours). Black J indicative of jet max of 40 m/s. Black box shows Sawyer-Eliassen circulation as described in text.

disruption of the flow and a counterclockwise circulation pattern. Fig. 23 (right panels) shows this circulation at different sections of the jet. The mixing of stratospheric air within the streamfunction rotors is evident in regions deep into the troposphere as seen in Fig. 23 (middle and bottom row, left panels). Just as in Case 1, Case 2 reveals the Sawyer-Eliassen opposing circulation patterns above and below the jet (Fig. 23, black box, all right panels). However, it is the inertial instability that controls the local poleward and downward circulation and subsequent STE.

6.2.3. Eulerian sections - Case 3

Case 3 is another example of how negative EPV interacts with the westerly jet and induces a poleward and downward circulation of high PV stratospheric air deep into the

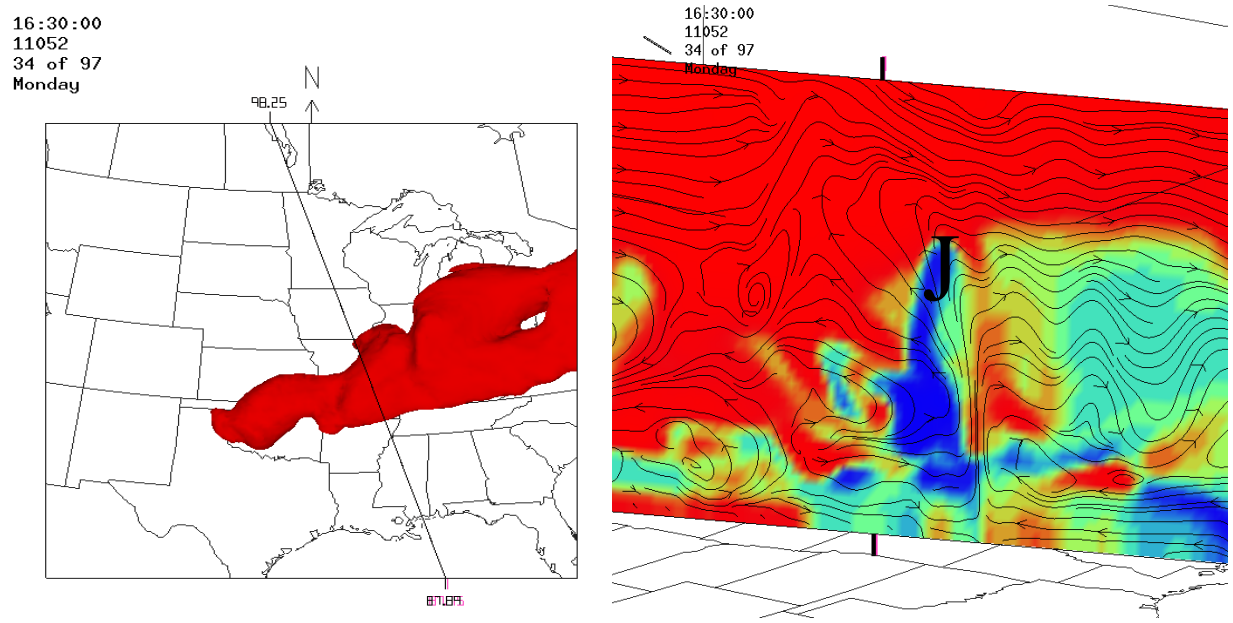

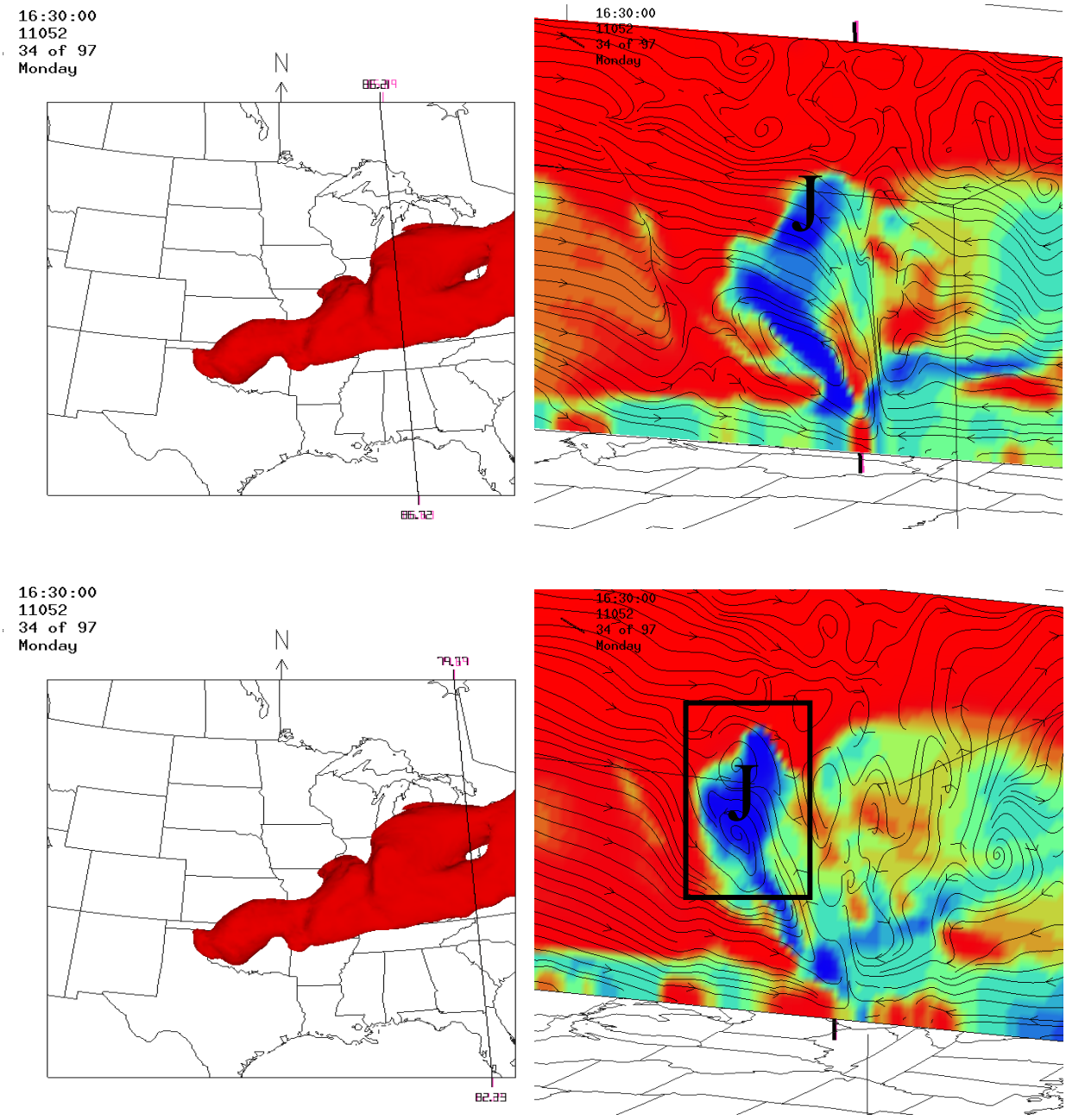

Figure 24. Eulerian cross sections for Case 3 at 1630 UTC on 21 February 2011. Left panels show an isosurface of jet at 50 m/s and the black line shows where the cross section occurs along the jet. Right panels show negative EPV (red shadings is positive EPV and blue shadings is negative) and streamfunction (black contours). Black J shows jet maximum at 50 m/s. Black box indicates Sawyer-Eliassen circulation as discussed in text.

troposphere. Once again this STE mechanism is shown in an Eulerian perspective as negative EPV affects circulations at each point along the jet. Figure 24 shows these circulation patterns by analyzing negative EPV (blue shading) and streamfunction (black contours) along the jet at 1630 UTC on 22 February 2011. As in the previous two cases, the Sawyer-Eliassen circulation opposing circulation above and below the jet is evident in Fig. 24 (bottom row, black box, right panel). The Sawyer-Eliassen circulation is not evident in each image as the circulation patterns are primarily controlled by inertial instability. At each cross section along the jet negative EPV produces a poleward and downward surge of high PV stratospheric air. This circulation pattern is most evident in Fig. 24 (middle right panel) as a rotor is revealed through the streamfunction contours. This rotor, which has a counterclockwise circulation, reveals a STE mechanism and mixing associated with negative EPV.

6.3. Lagrangian sections

6.3.1. Case 1

Figure 25 shows Case 1 in Lagrangian cross sections starting from the west coast of the United States and moving to the east coast, following the region of negative EPV activity seen near the tropopause. This longitudinal sampling of meridional cross sections (Fig. 25 (all panels)) shows a distinctive injection of stratospheric high PV air deep into the troposphere associated with negative EPV on the anticyclonic shear side of the jet. Starting the analysis in the far western part of the United States shown in Fig. 25 (top row, both panels), gravity waves just above the boundary layer are evident and finger-like structures of high PV air are beginning to intrude into the troposphere. Further analysis is needed to completely understand the role of inertial instability and their influence on gravity waves in the stratosphere and the troposphere. In

Fig. 25 (top row, both panels) the inertially unstable anomalies have not interacted with the jet at this point. Note from Fig. 25 (top row, both panels) there is no STE evident at this time. As the cross section moves into the Midwestern portion of the country (Fig. 25, second and third row) a more distinctive poleward and downward circulation develops around the polar jet. Moving to the east coast, (Fig. 25 bottom row), high PV air wraps further around the polar jet in response to the negative EPV on the anticyclonic shear side of the jet depositing high PV air deep into the troposphere and penetrating the boundary layer.

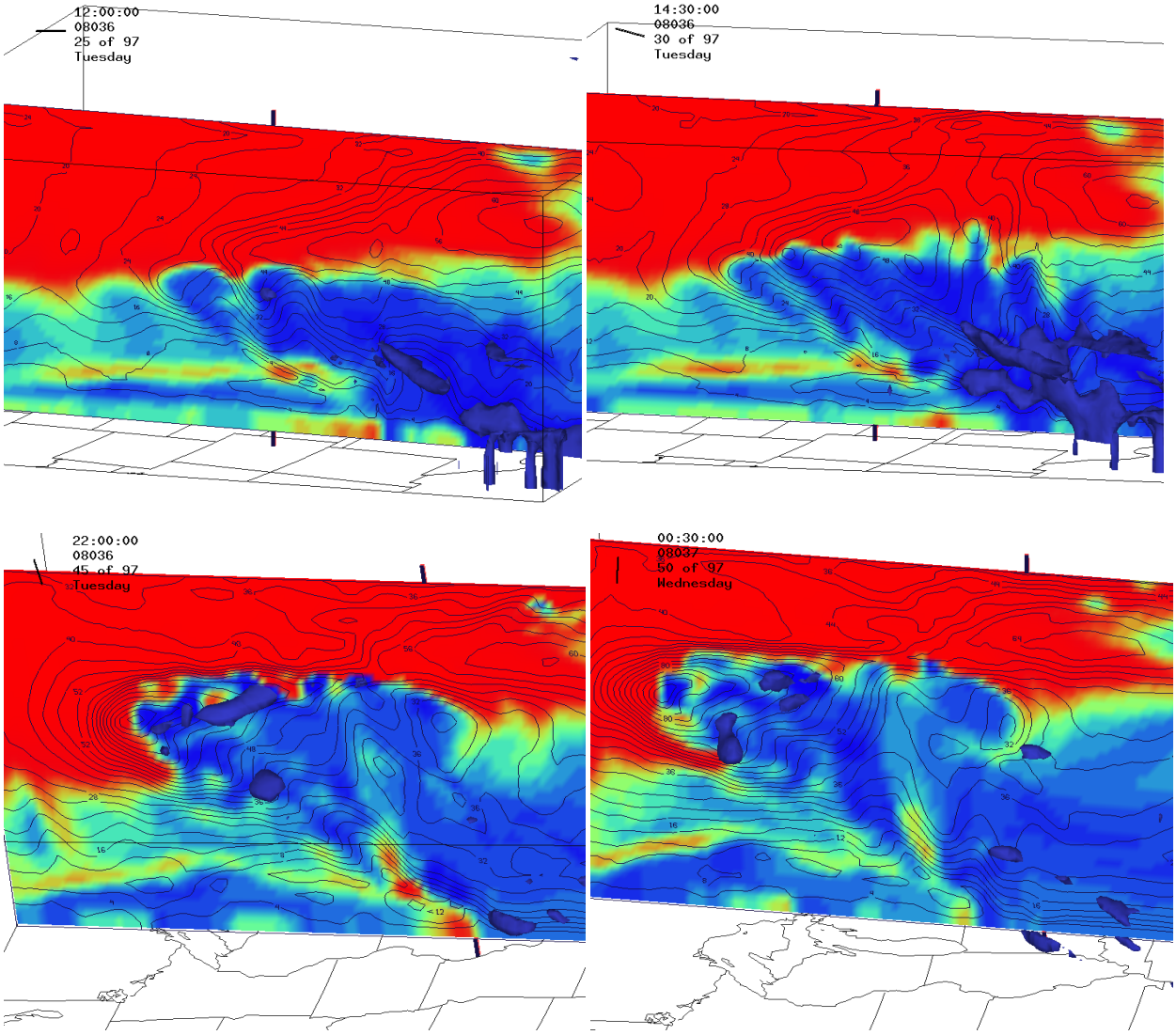

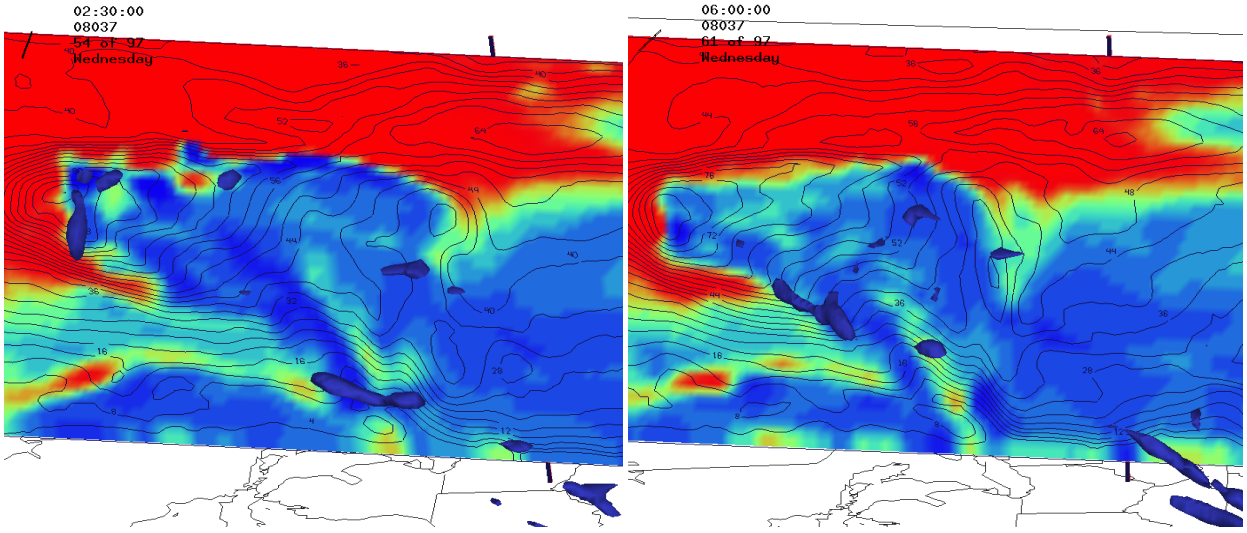

Figure 25. UWNMS longitudinal sampling of meridional cross section across the length of the westerly jet from the west coast of the United States (top panel) to the east coast of the United States (bottom panel) for 6 February 2008 Case showing connection between negative EPV and STE. All panels show jet wind speeds (black contours, every 4 m/s), PV (red shading, PV values < 0, yellow shading, PV values at 0, blue shading, PV values < 0, isosurface of EPV (dark blue isosurface, -3 PVU). Top row (left panel) is at 1200 UTC on 5 February 2008. Top row (right panel) is at 1430 UTC on 5 February 2008. Second row (left panel) is at 1500 UTC on 5 February 2008. Second row (right panel) is at 1800 UTC on 5 February 2008. Third row (left panel) is at 2200 UTC on 5 February 2008. Third row (left panel) is at 0030 UTC on 6 February 2008. Bottom row (left panel) is at 0230 UTC 6 February 2008. Bottom row (right panel) is at 0600 UTC on 6 February 2008.

6.3.2. Lagrangian sections - Case 2

Meridional Lagrangian analysis of Case 2 shows similar results to that of Case 1. It is evident that a poleward and equatorward circulation develops and maintains itself in the presence of inertial instability on the anticyclonic shear side of the jet. It is clear from Fig. 26 that ozone, which previously resided in the stratosphere, reaches deep into the troposphere through inertial instability disrupting the UTLS and enhancing meridional circulations. This poleward downward circulation is evident as long as there is sufficient negative EPV on the anticyclonic shear side of the jet.

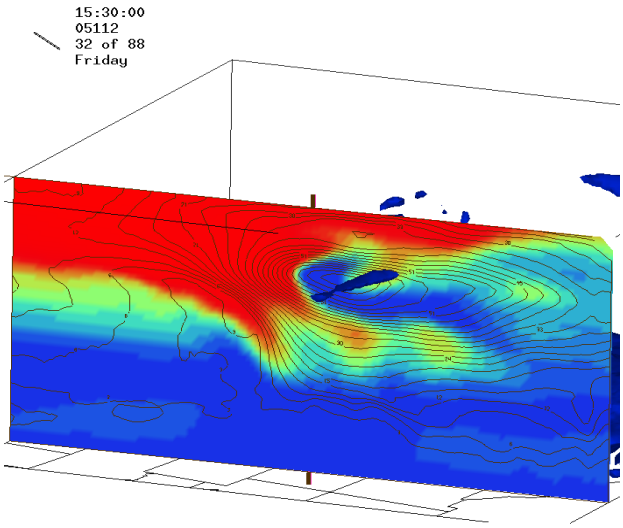
15:30:00
05112
32 of 88
Friday

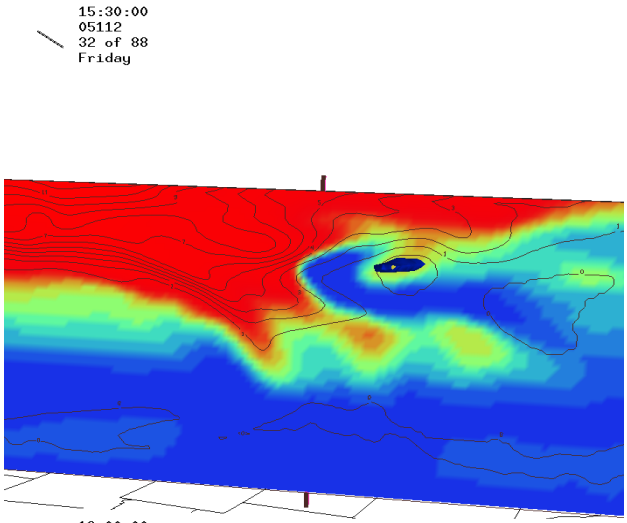
15:30:00
05112
32 of 88
Friday

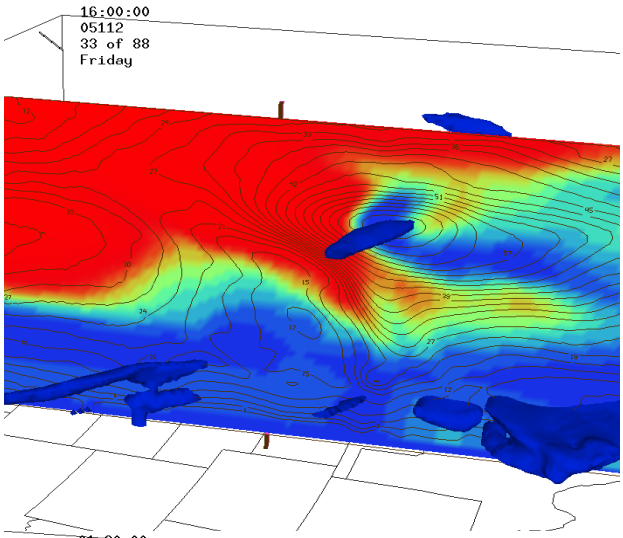
16:00:00
05112
33 of 88
Friday

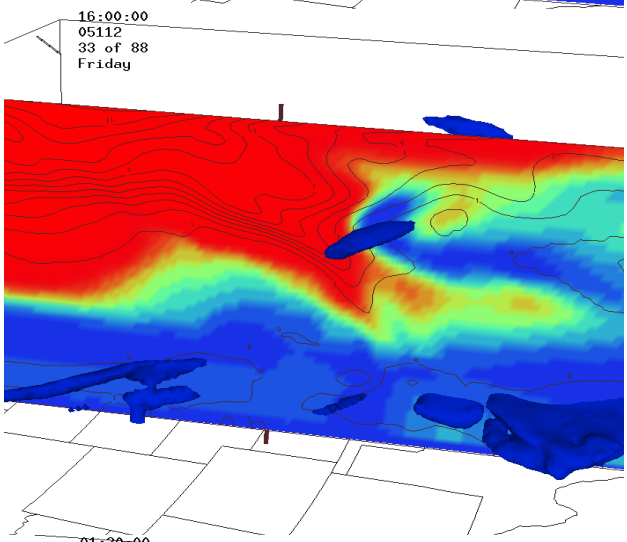
16:00:00
05112
33 of 88
Friday

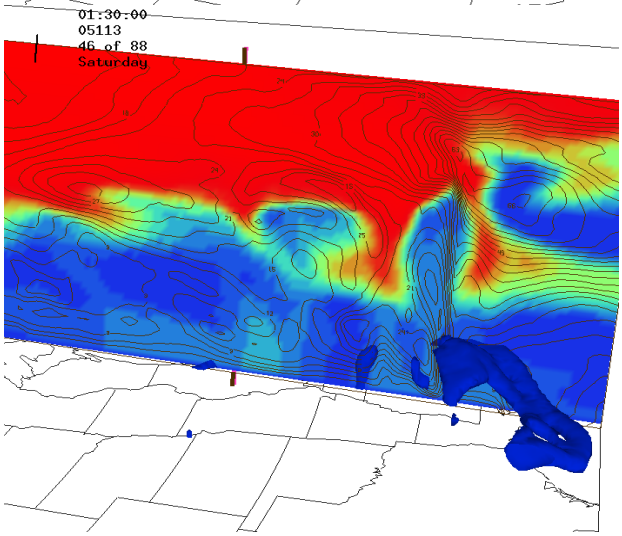
01:30:00
05113
46 of 88
Saturday

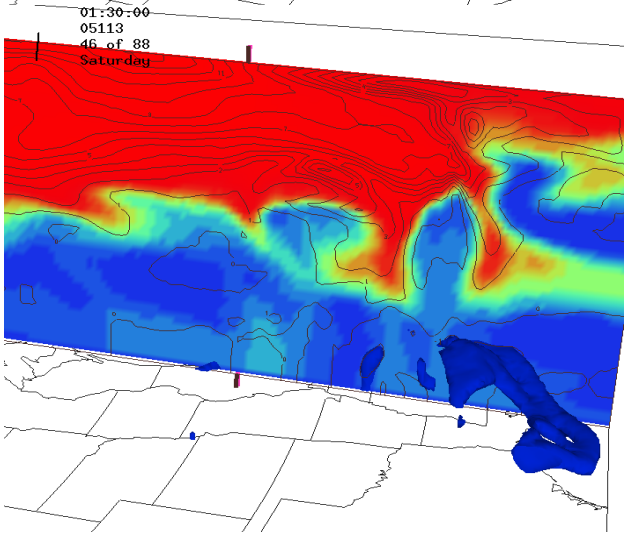
01:30:00
05113
46 of 88
Saturday

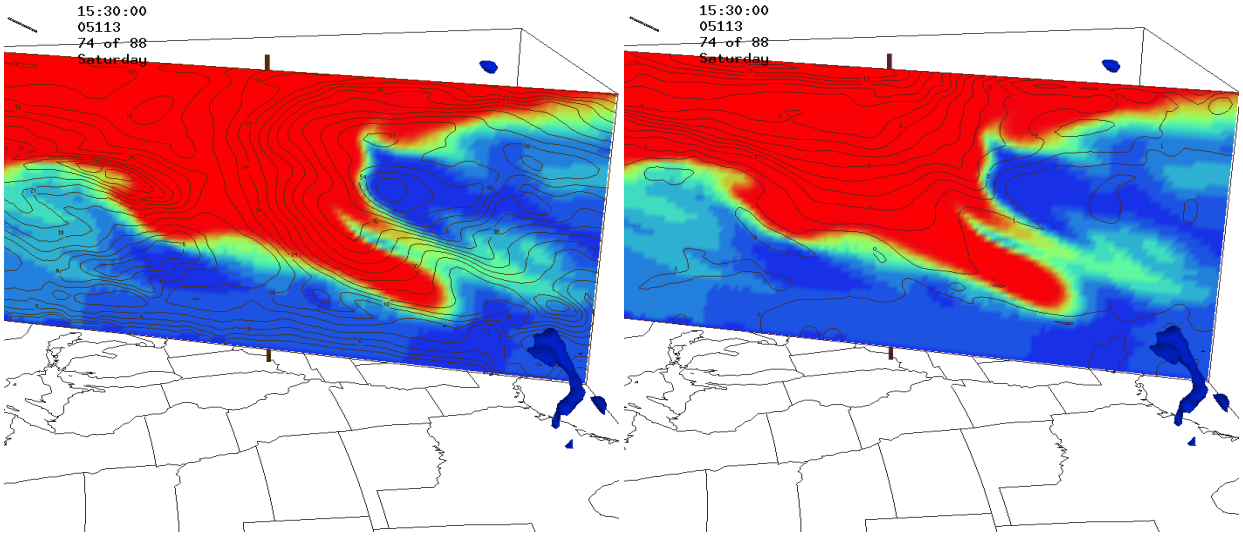

Figure 26. UWNMS longitudinal sampling of meridional cross section across the length of the westerly jet from the west coast of the United States (top panel) to the east coast of the United States (bottom panel) for 22 April 2005 Case showing connection between negative EPV and STE with the use of GEOS ozone. Top row (left panel) shows jet wind speeds (black contours, every 4 m/s), isosurface of EPV (-2 PVU), and ozone (red shading, high levels of ozone, yellow intermediate levels, and blue low levels) at 1530 UTC on 22 April 2005. Top row (right panel), same as in top row (left panel) except for PV (black contours, every 1 PVU), and no jet wind speed. Second row (left panel) same as in top row (left panel) except time is at 1600 UTC on 22 April 2005. Second row (right panel) same as in top row (right panel) except time is same as second row (left panel). Third row (left panel) same as in second row (left panel) except time is at 0130 UTC on 23 April 2005. Third row (right panel) same as in second row (right panel) except time is same as in third row (left panel). Bottom row (left panel) same as in third row (left panel) except time is at1530 UTC 23 April 2005. Bottom row (right panel) same as in third row (right panel) except time is the same as bottom row (left panel).

6.3.3 Lagrangian point of view - Case 3

Longitudinal samplings of meridional cross sections were also analyzed for the 21 February 2011 case and preliminary results are similar to that of the previous two cases. However in this case, both the subtropical and the polar jet are showing signs of inertial

instability induced STE. Figure 27 (all panels) shows two distinct jets, one at higher latitudes and one at lower latitudes where inertial instability induced STE is a focal point of interest. Fig. 27 (top row and second row) the high PV wrapping poleward and equatorward around the polar westerly jet makes it all the way down to the surface. However in the high PV wrapping poleward and equatorward around the subtropical jet makes it to the middle troposphere. This is most likely due to more negative EPV values on the anticyclonic shear side of the polar jet causing a greater disruption in the UTLS enhancing meridional circulations. However, this theory warrants further investigation.

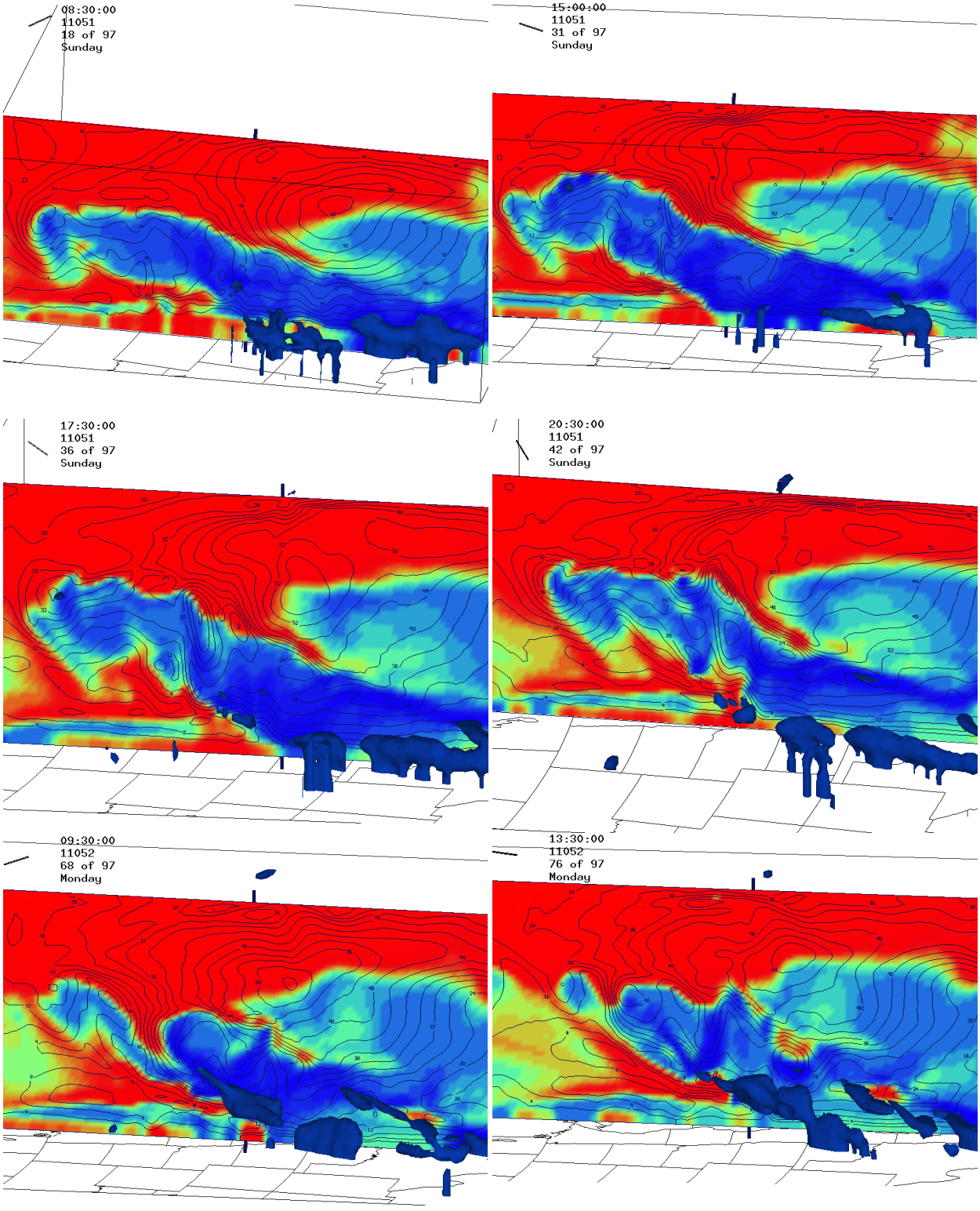
08:30:00
11051
18 of 97
Sunday
15:00:00
11051
31 of 97
Sunday
17:30:00
11051
36 of 97
Sunday
20:30:00
11051
42 of 97
Sunday
09:30:00
11052
68 of 97
Monday
13:30:00
11052
76 of 97
Monday

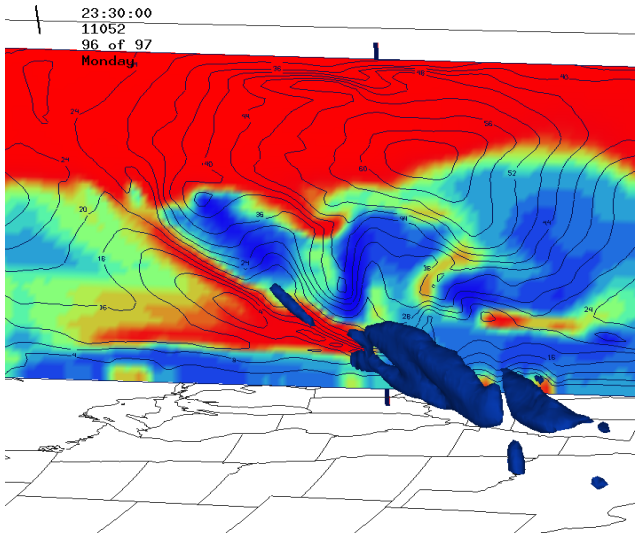

Figure 27. UWNMS longitudinal sampling of meridional cross section across the length of the westerly jet from the west coast of the United States (top panel) to the east coast of the United States (bottom panel) for 21 February 2011 Case showing connection between negative EPV and STE. All panels show jet wind speeds (black contours, every 4 m/s), PV (red shading, PV values < 0, yellow shading, PV values at 0, blue shading, PV values <0, isosurface of EPV (dark blue isosurface, -3 PVU). Top row (left panel) is at 0830 UTC 20 February 2011. Top row (right panel) is at 1500 UTC 20 February 2011. Second row (left panel) is at 1730 UTC on 20 February 2011. Second row (right panel) is at 2030 UTC on 20 February 2011. Third row (left panel) is at 0930 UTC on 21 February 2011. Third row (right panel) is at 1330 UTC on 21 February 2011. Bottom row (only panel) is at 2330 UTC on 21 February 2011.

Each of the three cases presented here show a unique look at the effects of negative EPV on jet circulation patterns and entrainment from a Lagrangian and Eulerian perspective. The Lagrangian point of view revealed a very intense poleward and downward propagation of high PV stratospheric air reaching deep into the troposphere upon interaction with the negative EPV anomalies. The Lagrangian perspective (Fig. 26 third row, both panels) also revealed features similar to that of Fig. 21 as shown in Shapiro (1978). A different perspective was shown with the Eulerian cross sections. The same negative EPV induced poleward and downward circulation patterns were apparent, however the streamfunction revealed individual counterclockwise rotors as a consequence of this anomalous negative EPV. These rotors captured the negative EPV

generated poleward and downward circulation patterns along the entire length of the westerly jet. The streamfunction in the Eulerian cross sections also revealed the Sawyer-Eliassen opposing circulation around the jet. As the Sawyer-Eliassen circulation was quite evident, negative EPV is the primary contributor to STE in these cases and it is this negative EPV that is not analyzed specifically in the Sawyer-Eliassen circulation equation.

7. Inertial Instability and Typhoons Talas and Roke and Hurricane Sandy

7.1 Introduction

Model simulations of tropical cyclones (TC) Talas (2011), Roke (2011), and Sandy (2012) are investigated with the UWNMS to further understand the effects of inertial instability, negative EPV and STE in extra tropical regions. A unique three-dimensional look shows a downward and equatorward circulation around the periphery of each storm, associated with extremely low inertial instability in the outer rainbands of the cyclone. Two vertical model top heights are used, one at 16 km and another at 25 km to test the sensitivity of this peripheral circulation to lid proximity. A distinct mechanism is evident in each scenario as stratospheric high PV air wraps itself around the entire periphery of the cyclone in association with low equivalent potential vorticity (EPV) in and around the outer edges of the storm at tropospheric and stratospheric levels. A comparable mechanism was shown to occur in midlatitude winter cyclones, as negative EPV air at the base of the stratosphere created STE. An STE exchange mechanism will be analyzed here, including an examination into the relationship that this STE has with the surface pressure changes during the evolution of the storm. Additional analysis will include the role of inertial instability in the development of stratospheric gravity waves.

7.2 History of Inertial Instability and Tropical Convection

Low upper tropospheric inertial stability is important for determining the intensity of convective systems (Molinari et al. 1997; Dickinson and Molinari 2000). Many studies have shown that convection should grow with the greatest intensity into regions of lowest inertial instability (Emanuel, 1979). The dynamical feedback that this upper tropospheric inertial instability has on the circulation patterns of middle atmosphere is not completely understood.

In addition to inertial instability in tropical convection, Holton and Alexander (2000) studied the role of gravity waves in driving the transport circulation of the middle atmosphere. However literature concerning the dynamics of extremely low EPV air as it ascends to the base of the stratosphere, and the effect it has on the middle atmosphere, is limited. Hitchman et al. (2001) studied the effects of extreme updrafts during a convective event south of Japan and discovered that a convective updraft radiated gravity waves into the stratosphere and induced a ring of stratospheric ozone to descend around the periphery into the middle troposphere. Observations suggest that smaller scale chaotic mixing, gravity waves, inertial and convective instability, turbulence, and other diabatic processes enable stratospheric air to cross the tropopause (Hitchman et al. 2001).

Other modeling studies (Li and Wang 2011; Wang 2008) have investigated the behavior of outer spiral rainbands and their interactions which can affect the intensity of tropical cyclones. Wang (2008) found that the presence of strong outer spiral rainbands limits the intensity of tropical cyclones. Following the results of Wang (2008), if very low values of inertial instability associated with the outer spiral bands limits the cyclone from intensifying, it is hypothesized here that low EPV air at the base of the stratosphere from intense vertical motion on the

periphery of the storm creates an STE mechanism introducing stratospheric air into the troposphere and inhibiting the strength of the storm. The objective of this study is to understand how small scale negative EPV in a tropical cyclone environment off the coast of Japan, influences STE, thus increasing the surface pressure within the storm, thereby reducing its intensity.

7.3 Analysis and Modeling Methods

TC Roke and Talas are modeled within the UWNMS while utilizing 2.5° ECMWF data. The resolution for these two studies is fixed at 20 km x 20 km x 300 m. There are 152 points in the latitudinal direction, 152 points in the longitudinal direction, and 65 or 85 points in the vertical direction. The time step is thirty minutes. The top of the model is set to either 16 km or 25 km to test the effects that model top height may have on evolution for both storms. This research employs the ability of Vis5D to view the full three-dimensional structure of each tropical cyclone and the associated dynamics.

Both TC Talas and Roke are modeled with model top heights of 16 km and 25 km. This type of approach was implemented to explore whether or not the model height interfered with the apparent mushroom cloud circulation that developed in both storms and to determine if there is a difference in the intensity of the downward circulation associated with each negative EPV anomaly. The relative strengthening, weakening, or neutrality regarding central pressure is also analyzed with this method.

Hurricane Sandy is modeled within the UWNMS using GFS forecasts. The resolution for this case is fixed at 80 km x 80 km x 200 m. There are 110 points in the latitudinal direction, 90 points in the longitudinal direction, and 32 points in the vertical direction. The time step is thirty

minutes. The top of the model is set to 18.5 km. Once again Vis5D is used to analyze case specific features and associated dynamics.

7.4 Case 1- Typhoon Talas

7.4.1 Synoptic Description

Talas was the twelfth named storm of the 2011 Pacific typhoon season. The cyclone formed over the western Pacific Ocean on 25 August 2011 and moved north-northwestward across Japan. Figure 28 (top right panel) shows the actual path of the storm (see figure caption for color coded description). Fig. 28 (top left panel) shows a satellite image of TC Talas using the Moderate Resolution Imaging Spectroradiometer (MODIS) on NASA's Terra satellites as it approaches Japan on 2 September 2011. The cyclone was just south of Japan at this time with the northernmost rainbands reaching the island. On 2 September 2011, it was reported by the U.S. Navy's Joint Typhoon Warning Center that Talas had maximum sustained winds of 50 knots, with gusts up to 65 knots, which was down slightly from the previous day. Fig 28 (bottom left panel) shows a color coded image of rainfall totals from 30 August to 5 September 2011 using Tropical Rainfall Measuring Mission (TRMM) satellite data. The heaviest rainfall, in excess of fourteen inches (shown in dark blue shading) fell to the north of Toyama and Ishikawa. TRMM can measure rainfall from its orbit and provide the vertical heights of thunderstorms within a tropical cyclone. Fig. 28 (bottom right panel) shows a TRMM satellite image from 31 August 2011 displaying heavy rainfall and strong thunderstorms as Talas approaches Japan.

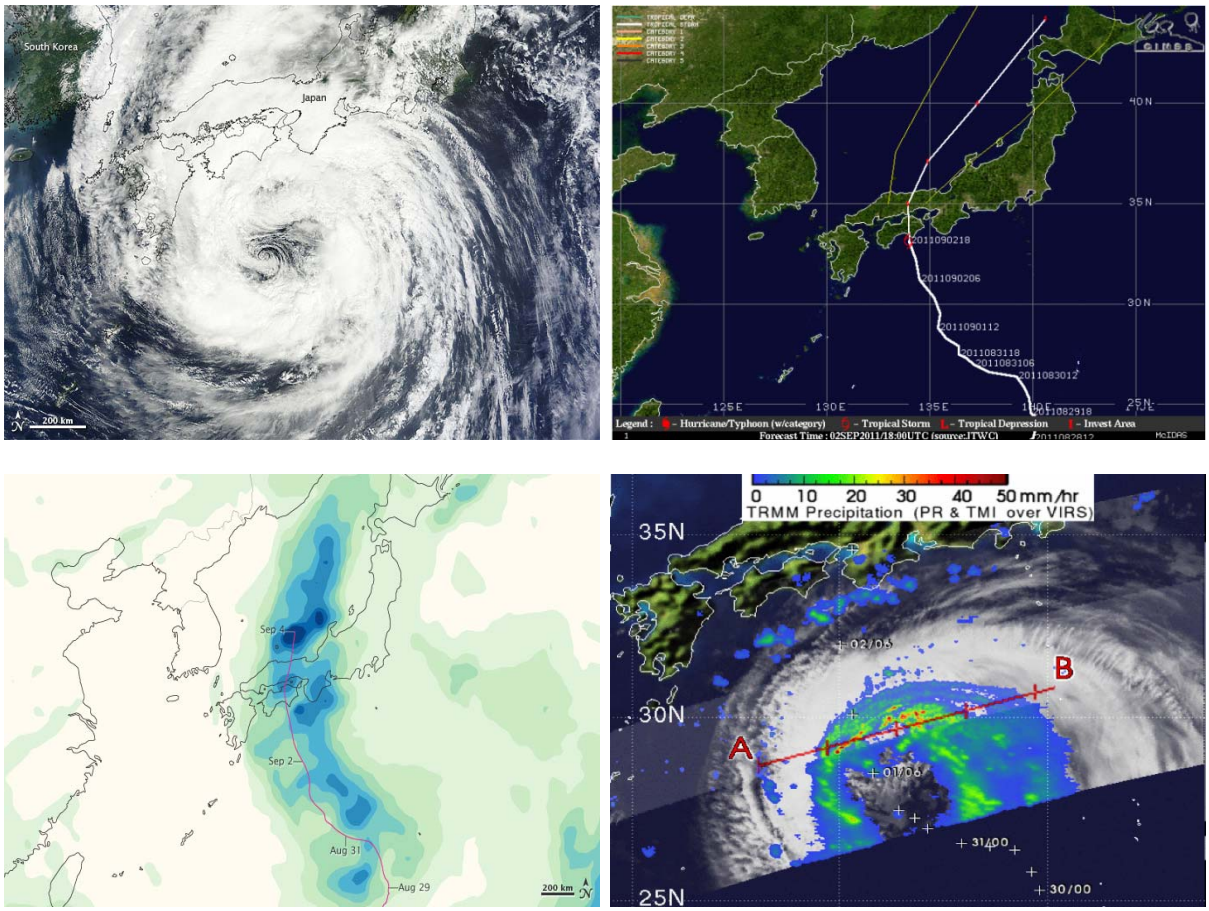

Figure 28. The Moderate Resolution Imaging Spectroradiometer (MODIS) on NASA's Terra satellite acquired this natural-color image on 2 September 2011 (top left panel). CIMSS track of Talas moving over Japan (top right panel). This color-coded image shows rainfall totals from Tropical Storm Talas from 30 August to 5 September 2011(bottom left panel).The heaviest rainfall, more than 14 inches, appears in dark blue. The lightest rainfall, less than 2 inches appears in light green. Areas with only a trace of rain appear pale yellow (bottom left panel). On 31 August 2011 at 7:21 p.m. EDT, TRMM captured several intense thunderstorms in Talas' northern edge- that were about 10 km high. Yellow and green indicate rainfall occurring between .78 to 1.57 inches per hour. Dark red areas are considered heavy rainfall, as much as 2 inches of rain per hour highlighted by the line A to B (bottom right panel).

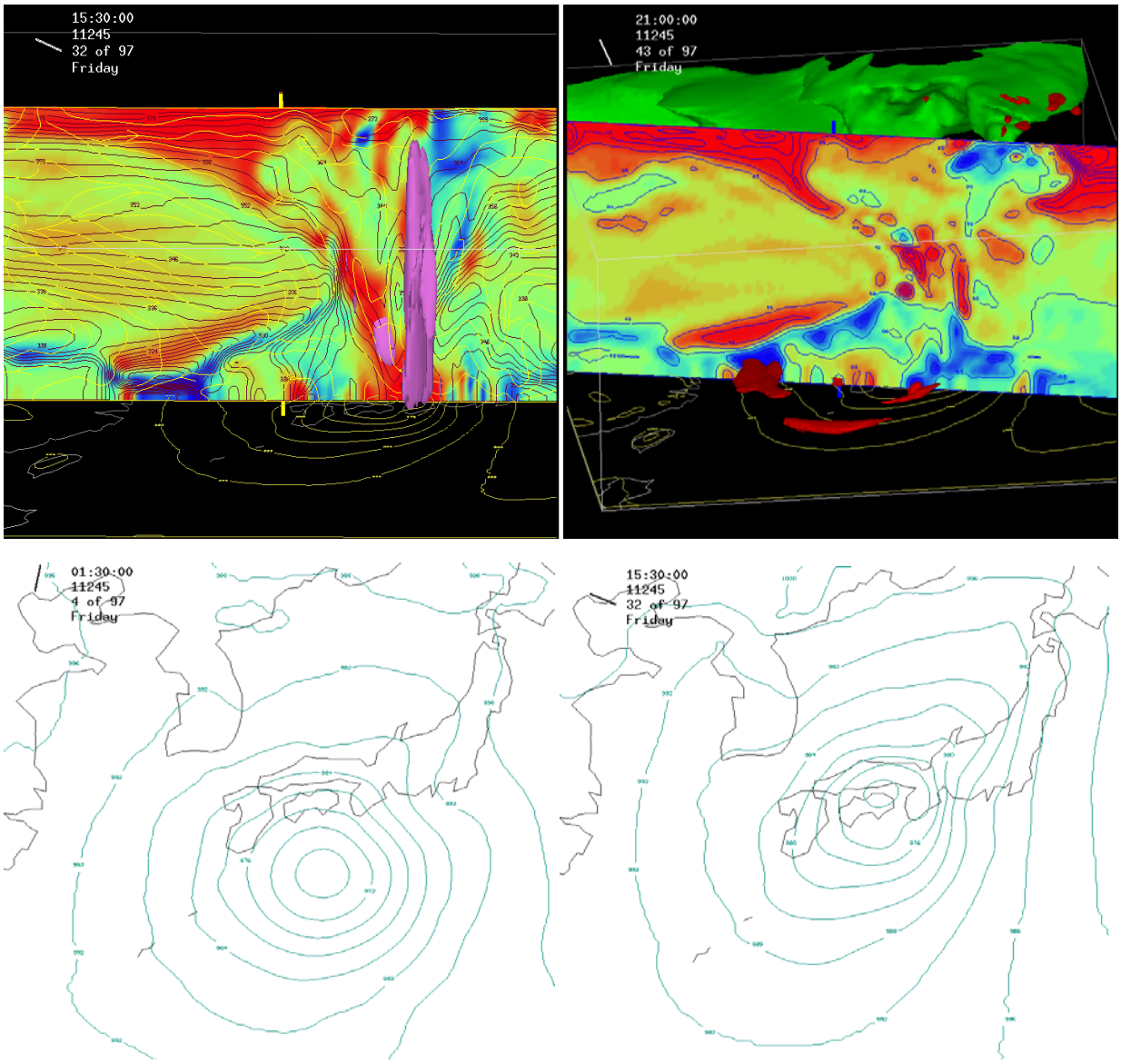

Figure 29. UWNMS model output using 2.5 degree ECMWF reanalysis and a 16 km model top showing (top left panel) 1 September 1530Z showing theta-e (black contours, interval 4K), the .4 m/s vertical velocity isosurface in purple, EPV values in PVU shaded showing positive EPV in red, moderate values in orange, and negative values in blue, and surface pressure contours (yellow contours, interval 4 hPa). (Top right panel) 1 September 2100Z showing (shading same as in top left panel), EPV (black contours, interval 1 PVU), the EPV-2 PVU isosurface in red, and the 45 m/s U component of the wind isosurface in green. (Bottom left panel) 1 September 130Z showing sea level pressure (blue contours, interval 4 hPa). (Bottom right panel) shows 1 September 2011 1530Z (same as in bottom left panel).

7.4.2. TC Talas16 km Model Top

Figure 29 shows the UWNMS results for the 16 km run. The focal point of discussion here is to determine what dynamical processes are involved in a transporting of inertially unstable air to the base of the stratosphere by strong vertical motion, as well as the distinct wrap of stratospheric air around each negative EPV anomaly. Figure 29 (top left panel) shows these circulation patterns as Talas makes landfall over Japan at 1530Z on 2 September 2011. An isosurface of vertical motion (shown in violet) at 5 cm/s carries low EPV air from the surface of the storm to 15 km, inducing a push of stratospheric high PV air around each low EPV anomaly. Fig. 29 (top left panel) shows this low PV air as it travels from the stratosphere at 16 km down into the eye of the cyclone.

Another mechanism stands out in Fig. 29 (top left panel) as the low EPV air deforms the theta-e contours revealing gravity wave patterns radiating away from the extremely low EPV air at 15 km. Recent studies (Kuester et. al. 2008) have concluded that analysis of the movement of convective sources and local winds gives further insight into the mechanism that can cause gravity waves. It is shown here that gravity wave generation in deep convection is favored in association with negative EPV values.

Fig. 29 (top right panel) shows the same effect. High PV stratospheric air wraps itself around the periphery of the storm. This is similar to the results of Hitchman et al. (2001) as they examined a convective complex propagating over the Pacific south of Japan, which resulted in a convective updraft radiating gravity waves into the stratosphere, and induced a ring of ozone to descend into the middle troposphere. It seems that extremely negative EPV can facilitate and intensify mass exchange between the stratosphere and troposphere. Additionally, negative EPV

can be just as important as intense vertical updrafts when identifying mass exchange and stratospheric gravity wave propagation.

Here it is proposed that stratospheric air is brought downward as a consequence of strong vertical motion carrying negative EPV to the base of the stratosphere, as shown in Fig. 29 (top left panel) and Fig. 29 (top right panel). Wu et al. (1996) concluded, through a modeling study of hurricane Bob, that the hurricane motion can be affected by the flow associated with upper level PV anomalies diabatically produced above the hurricane. Here is postulated that there is a relationship between this high PV air injected around the core of the cyclone and hindrance of storm intensification as shown in Fig. 29 (bottom left panel) and Fig. 29 (bottom right panel). The central pressure does not drop below 976 mb between 0130Z on 1 September 2011 and 1530Z on 1 September 2011. The injection of dry air from the stratosphere into the core of the storm near the surface is one mechanism by which a cessation of storm amplification may occur.

7.4.3. TC Talas 25 km Model Top Analysis

It has been shown that PV methods are becoming more widely applied to tropical systems (Wu et al. 1996). Wu and Emanuel (1994) showed that PV dynamics can be applied to the understanding of hurricane structure. Here, PV dynamics will be studied by implementing a 25 km model top height. It will be shown that increasing the model top height yields similar results to that of the 16 km model top. Using the same model times and cross sectional areas for the TC Talas run with a 16 km top, Figure 30 (top left panel) reveals four distinct stratospheric intrusions of high PV air moving into the middle troposphere. Once again low EPV air pushed upward by 4 cm/s vertical motion plumes hits the base of the stratosphere, wraps itself around

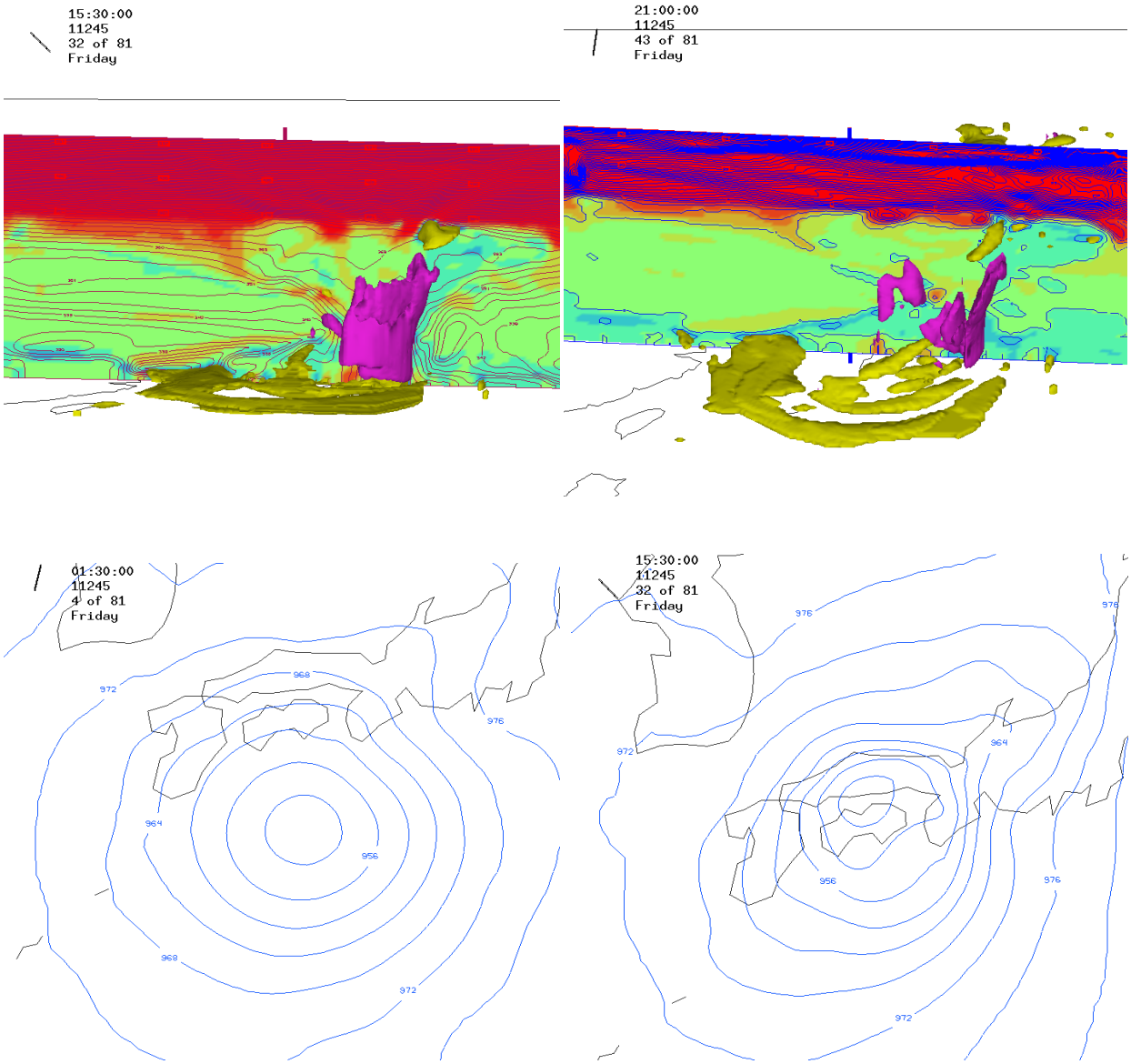

Figure 30. UWNMS simulation of typhoon Talas using 2.5 degree ECMWF data with a 25 km model top at 1 September 2011 showing the relationship between inertial instability, vertical motion, STE and sea level pressure. The top left panel shows an east-west cross section through Talas just to the south of Japan at 1530 UTC with theta-e (black contours, 5 K), vertical motion (pink isosurface, 4 cm/s), negative EPV (yellow isosurface, -2 PVU), and potential vorticity, (red shading, high PV stratospheric air). Top right panel at 2100 UTC same as in top left panel except PV contours (blue, 1 PVU) are shown instead of theta-e contours. Bottom left panel shows surface pressure contours (blue, 4 hPa) at 130 UTC. Bottom right panel same as in bottom left panel except time is at 1530 UTC.

the -2 PVU anomalies, and stratospheric high PV air hangs deep into the troposphere. Through Fig. 30 (top left panel) it is also evident after analyzing the extremely low EPV air slamming into the base of the stratosphere. This very low EPV air at the base of the stratosphere brought about by deep convection is an important factor in large scale atmospheric circulations. An analysis of both model top heights shows stratospheric intrusions extending into the troposphere. The view that each model top offers shows a unique perspective while yielding similar results, including the generation of stratospheric gravity waves. It is important to note that the 25 km model top shows a significant damping of the STE mechanism although it is still evident.

Little is known about low EPV air at the base of the stratosphere and the generation of gravity waves in the stratosphere. Ongoing research investigates the sources and mechanisms that generate gravity waves and the momentum flux they carry to the middle atmosphere (Kuester et. al. 2008). Fig. 30 (top right panel) displays the same dynamical features. High EPV air wraps itself around the periphery of the storm as a result of the convectively driven low EPV air at the base of the stratosphere. Wu et. al. (1996) postulates that hurricanes have strong sources of heating near their centers and these sources tend to redistribute the PV in the hurricane by creating a sink of PV in the upper troposphere above the storm. In the case of TC Talas this low EPV air creates a stratospheric transport pathway by which air spills outward and downward around the periphery of the cyclone. If there is a background vertical shear, the baroclinic hurricane vortex would be tilted, and the negative upper PV anomaly can project a flow extending down into the lower troposphere (Wu et. al. 1996).

As shown in TC Talas 16 km, another possible outcome behind these upper level negative EPV dynamics is a cessation of storm intensification due to stratospheric air entering the core of the storm. TC Talas 25 km reports curious yet contrasting results. Because of the 25

km model top the high PV air entering the core of the storm is damped significantly. This lack of stratospheric air entering the core of the storm results in intensification, as the central pressure dropped 12 mb in fourteen hours. The 25 km model top reveals that if a dose of stratospheric air enters the storm, the cyclone does not intensify. However, if this stratospheric air is damped or muted a cyclone amplification is favored.

Recent studies have explored possible mechanisms behind weakening and lack of intensification in tropical cyclones. For example, Frank and Ritchie (2001) postulated that shear causes the eyewall to become asymmetric and it is these asymmetries in the upper troposphere that become sufficiently strong so that air with high PV values is mixed outward. They explained that it is the high PV values which allow shear to ventilate the eye resulting in a loss of the warm core at upper levels, thus weakening the entire storm. Here it is postulated that the injection of high stratospheric PV air reaches into the center of the storm due to the poleward downward circulation created by very low EPV aloft. The negative EPV structures hit the high tropical tropopause and send very dry high PV air cascading down the periphery of the cyclone and as shown in Fig. 30 (top left panel), producing arm-like structures around each negative EPV anomaly.

Both the 25 km and 16 km simulations revealed an injection of stratospheric high PV air around the periphery of the storm and a local downward and equatorward circulation around each low EPV anomaly. The difference was in storm intensification suggesting that if the injection of stratospheric air into the storm is muted, a strengthening may occur.

7.5 Hurricane Sandy

Preliminary diagnosis and simulations of hurricane Sandy shows similar dynamical aspects as found in Talas. Figure 31 shows some of this work in its early stages. Based on

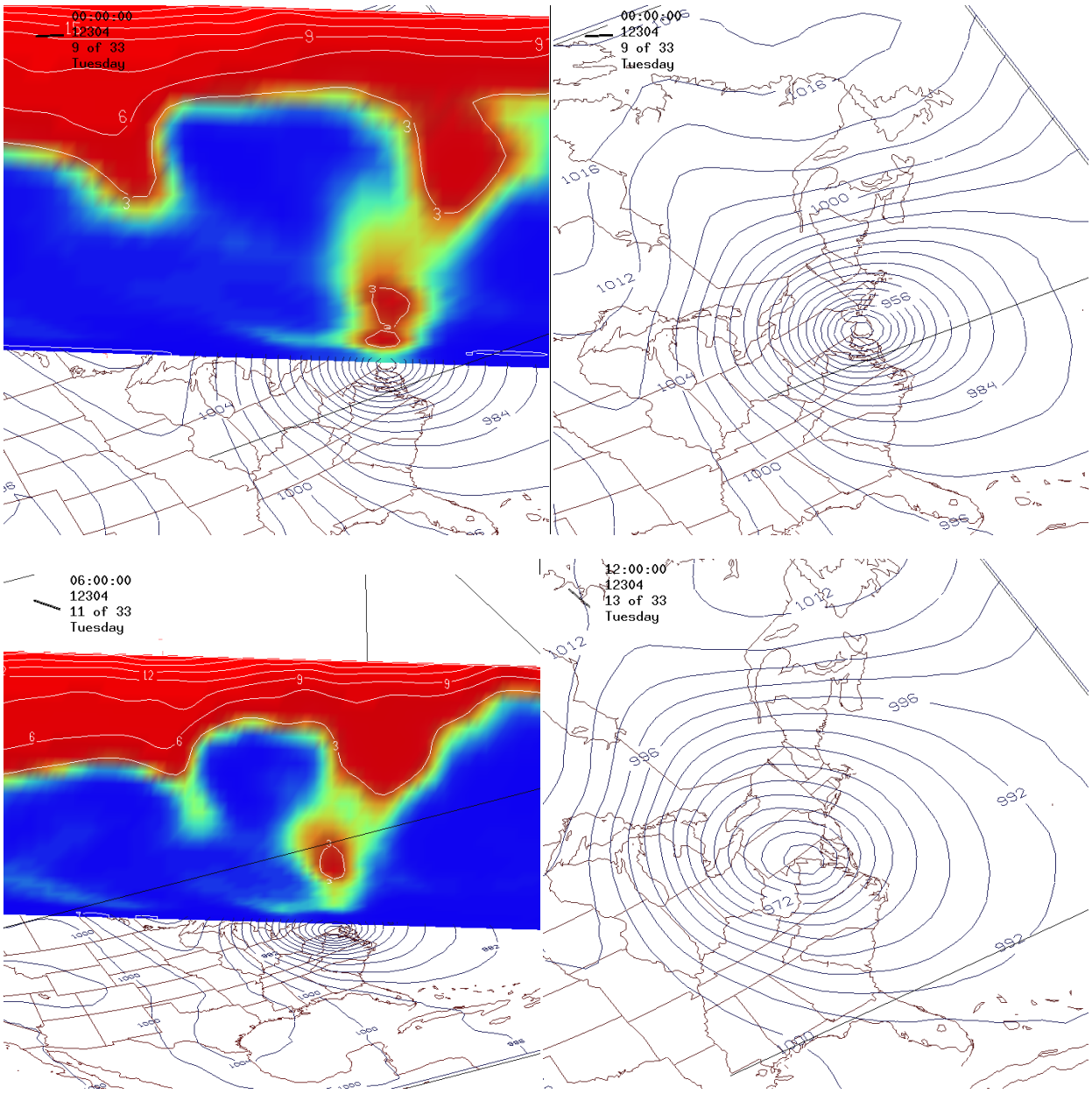

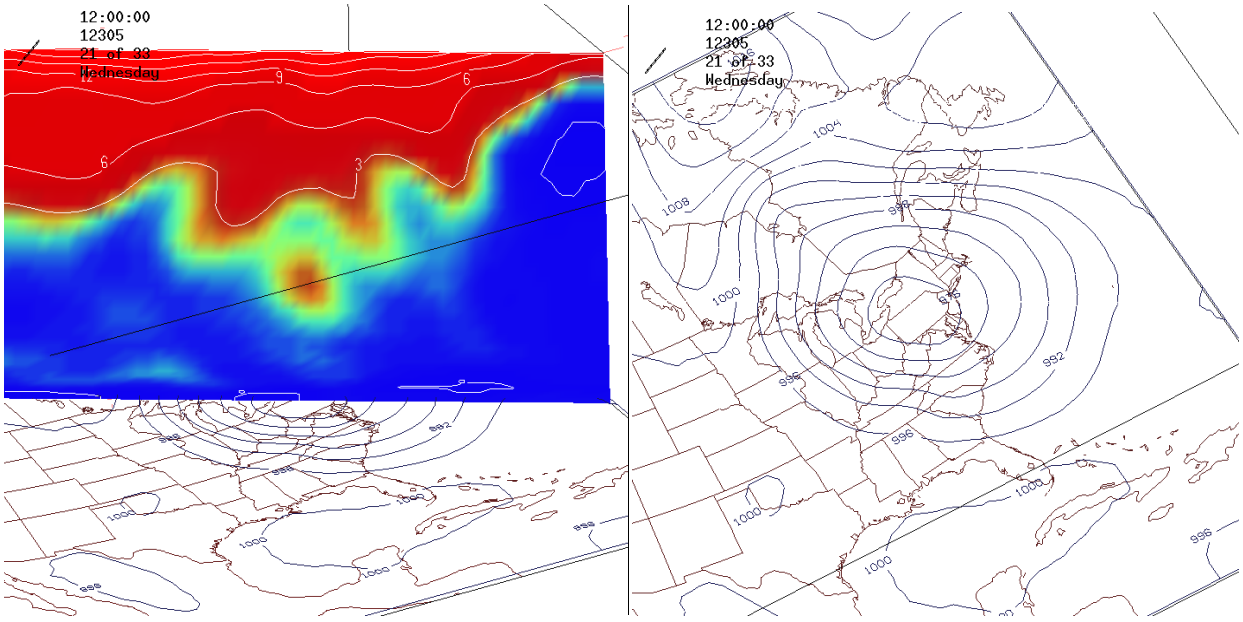

Figure 31. UWNMS simulation of hurricane Sandy initialized with GFS data and a 16 km model top showing a possible STE mechanism around the periphery of the storm and associated surface pressure at (top panels) 0000 UTC on the 304th day (middle panels) 0600 UTC on the 304th day and at (bottom panels) 12Z on the 306th day. Color shadings for all panels are: red (PV < 3 PVU) blue (PV > 3 PVU), white contours (PV), blue contours (surface pressure (contoured every 4 hPa).

Fig. 31 (all left panels) and similar to Talas, a surge of high PV stratospheric air is seen on the periphery of the storm. A curious injection of stratospheric dry air in also evident in Fig. 31 (top left panel), which could be responsible for the rapid increase in surface pressure associate with the storm. The images associated with Fig. 31 show a rapid decline in surface pressure shortly after the stratospheric dry intrusion reaches the core of the storm. The top right panel shows surface pressure at 936 hPa. Six hours later the surface pressure rises 19 hPa to 956 hPa (middle right panel). Six hours after that the central pressure rises again, this time a 21 hPa climb to 976 hPa (bottom right panel). Further analysis is needed to fully understand the extent of

stratospheric dry air intrusions associated with inertially unstable air and surface pressure increase in Sandy and other tropical/extratropical systems.

7.6 Typhoon Roke

Figure 32 supports the inertial instability and high stratospheric PV dynamics regarding Sandy and Talas. The left panel of Fig. 32 shows Roke with a 16 km model top. Areas of negative EPV rise to the top of the model, distort the UTLS, and create an outward and downward circulation of high PV air and a large scale circulation of high PV air around the periphery of the storm. The right panel in Fig. 32 shows Roke with a 25 km model top. The results regarding the

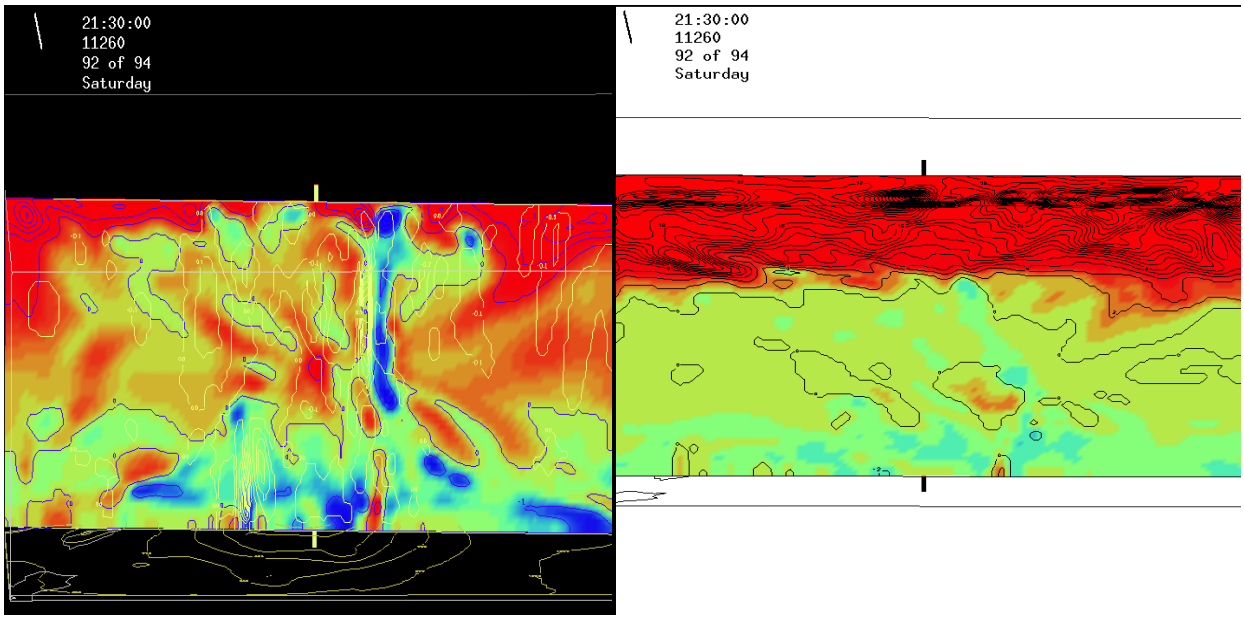

Figure 32. Panel shows UWNMS simulation of Typhoon Roke with a 16 km (left) and a 25 km model top (right) initialized with 2.5 degree ECMWF data showing the possible relationship between inertial instability and STE locally within the storm and around the periphery of the storm. Both panels are an east-west cross section through Roke on the southernmost coast of Japan. Color shading for left panel: dark blue shading (negative EPV, -2 PVU), dark red shading (EPV, < 0 PVU) dark blue contours (EPV contoured every 1 PVU). Right panel: same as in left except black EPV contours.

strength and magnitude of the inertial instability induced STE are somewhat damped. However, inertial instability induced stratospheric gravity waves are much more apparent in the 25 km model top. The stratospheric high PV air coming down and around the periphery of Roke is still visible due to the inertial instability and negative EPV within the storm. Once again, more research is needed to further understand the role of inertial instability and STE in tropical/extra tropical cyclones. Analysis will include tropical cyclones that form over all basins, more specifically the Atlantic Ocean, Gulf of Mexico and the southeastern United States. A focal point of research will be to show the significance of stratospheric dry intrusions resulting from inertially unstable regions in the UTLS and the effects on surface pressure changes.

7.7 Tropical Cyclone Summary

Figure 33 shows a schematic of the dynamics surrounding an idealized tropical cyclone with respect to Talas, Sandy and Roke. As with most tropical cyclones, low EPV in the far outer spiral rainbands. Some of this low EPV air, depending on the strength of the vertical velocity, is lifted to the base of the stratosphere. This results in a local poleward downward circulation around the individual negative EPV anomaly and finger-like apertures to descend into the troposphere. A more broad circulation also develops as the negative EPV hits the bottom of the stratosphere causing a displacement of the isentropes, resulting in gravity wave propagation in the stratosphere. Finally, due to the disruption of the lower stratosphere by the low EPV anomalies, high PV air is entrained downward and equatorward around the periphery of the storm.

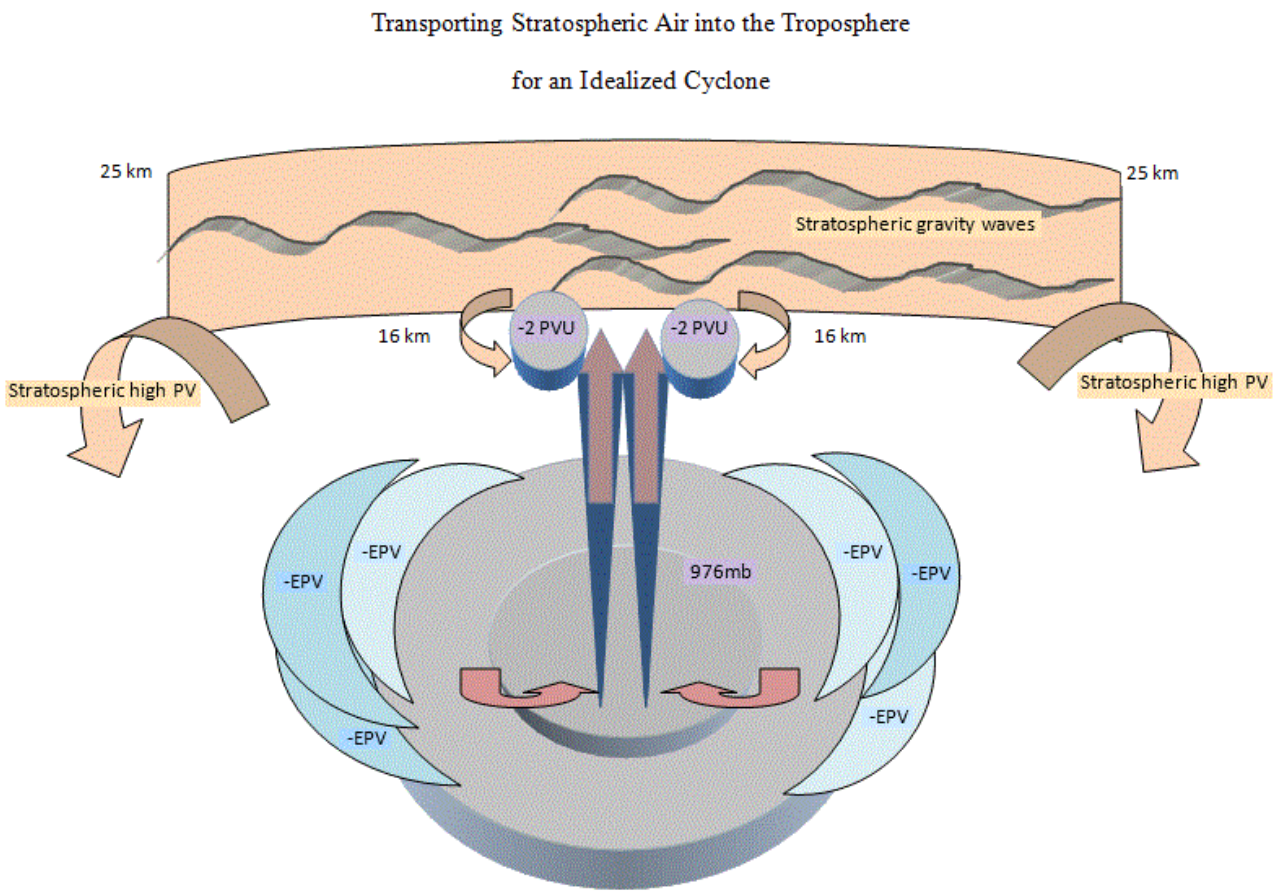

Figure 33. Schematic of the overall dynamics of an idealized tropical cyclone as negative EPV interacts with the base of the stratosphere.

Talas and Roke 2011 and Hurricane Sandy 2012 were studied using the UWNMS to gain insight into the dynamics surrounding a possible cause for a distinct downward circulation pattern involving negative EPV anomalies. As negative EPV is pushed upward by intense vertical motion fields within the core of the storm, these anomalies hit the base of the stratosphere. Within each local anomaly a circulation of high stratospheric PV air wraps itself downward into the troposphere. Additionally a larger scale pattern emerges, in which a

downward and inward circulation appears on the west-east periphery of the storm. This is consistent with Wu and Kurihara (1996) as they concluded that the areal extent of the cyclone's influence on its environmental PV field is far more extensive in the upper troposphere. Here it is shown that the base of the stratosphere is the primary location for the existence of negative EPV in Talas and Roke.

Additional analysis of Roke and Talas shows the propagation of gravity waves emanating within the stratosphere due to the negative EPV anomalies hitting the base of the stratosphere. Past studies have possible mechanism theories for the existence of these waves above deep convection. Fovell et. al. (1992) and Lane et. al. (2001) suggest that a parcel of air rises to its level of neutral buoyancy and oscillates at the local buoyancy frequency, displacing the isentropes of a stable layer directly above. It has been well established that gravity waves are generated from deep convection, but little is known about the dynamics of negative EPV anomalies facilitating stratospheric gravity waves in tropical cyclones. Here it is shown that if stratospheric air enters the core of the storm, the cyclone does not intensify, however if this stratospheric air is lessened an amplification occurs in the central pressure of the cyclone. Additional research is needed to fully understand how the injection of stratospheric air into the central portion of this or any tropical cyclone leads to neutrality or a weakening of the central pressure of the storm.

8. Summary and Future Work

Inertial instability plays an important role in STE in midlatitude cyclones and tropical cyclones Talas, Roke and Sandy. It was shown through the analysis of three midlatitude cyclones that along a surface cold front low EPV develops and through latent heat processes it is carried in

the vertical by strong plumes of vertical motion. As the air with low EPV rises in the vertical, it becomes more negative with values reaching as low as -3 PVU, as seen in Case 1. After reaching the UTLS at maximum height of 14 km the negative EPV anomalies adhere to the anticyclonic shear side of the westerly jet. A subsequent poleward and equatorward circulation develops in each midlatitude case as meridional circulations are enhanced by the negative EPV, disrupting the base of the stratosphere. This enhanced circulation brings high PV air that previously resided in the stratosphere deep into the troposphere. It was shown that a layer of stratospheric-tropospheric air mixed to a depth of about 4 km. As the negative EPV air distrupted the UTLS a waterfall of dense, high PV stratospheric air wrapped itself poleward and downward around the jet, revealing an STE mechanism. It was shown in this research that the overall magnitude of the westerly jet did not affect the STE mechanism that was produced by the inertially unstable regions on the anticyclonic shear side of the jet.

Additional analysis showed that in the midlatitudes inertial instability can facilitate a mesoscale momentum surge, adding additional azimuthal speed to the jet core. Associated with inertial instability there is enhanced divergence on the anticyclonic shear side of the westerly jet, leading to a sudden increase in jet core wind speeds or inertial flare-ups. Both the conservation of angular momentum and geostrophic adjustment theory were used to study the inertial flare-up phenomena. It was shown that as negative EPV is moved upward and poleward from the surface it is transporting air from a lower latitude with higher angular momentum into the jet. The original speed of the air must increase as it moves poleward to conserve angular momentum. It is this sudden surge of momentum, which includes negative EPV, which adds a rotational speed increase, producing an inertial flare-up. From conservation of angular momentum, if a parcel is displaced from 40° to 41° a wind speed increase of 11 m/s can be calculated.

Building upon conservation of angular momentum concepts, it was shown that inertial instability can enhance convergence of air at the left entrance region and the right exit region if present at those locations. This is true, as inertial instability is, by definition, a large departure from geostrophic balance. If the PGF and the Coriolis force are out of balance divergence occurs, particularly on the anticyclonic shear side of the jet. The negative EPV greatly enhances this divergence resulting in an inertial flare-up. In the cases presented, it was shown that this enhanced divergence, through the presence of negative EPV anamolies, increased jet core wind speeds by 12 m/s in half hour to hour intervals.

A side by side view of absolute vorticity, divergence, negative EPV and wind speeds gave insight into the development of inertial flare-ups and emphasized that a decrease in absolute vorticity is related to upper level divergence, which is enhanced by the existence of inertial instability. This inertial instability is the main driver in the creation of inertial flare-ups as inbalances between the PGF and the Coriolis force, as air flows through the jet enhances upper air divergence primarily in the left exit region.

A unique Eulerian and Lagrangian perspective was analyzed to better understand how inertial instability acts as a precursor to STE. The Eulerian cross sections studied one specific time along the jet in which negative EPV was the prime focal point with respect to circulation patterns. Contours of streamfunction revealed an inertial instability driven Sawyer-Eliassen circulation which produced the entrainment of stratospheric high PV air deep into the troposphere. It was shown that as the Sawyer-Eliassen equations only consider absolute vorticity to be positive, therefore in these cases negative EPV was shown to be a significant contributor to STE.

The Lagrangian point of view supported this negative EPV induced STE mechanism as inertial instability affected regions were analyzed at different times along the jet. This type of analysis revealed a more enhanced negative EPV induced poleward and downward circulation as the jet moved north-northeast toward the pole. Results also showed that the inertial instability-driven STE around the polar jet tended to reach deep into the troposphere near the surface, whereas the inertial instability induced STE around the subtropical jet tended to entrain into the middle troposphere. Overall, the Lagrangian and Eulerian perspectives revealed a negative EPV-induced STE mechanism by which air flows poleward and downward around the jet.

As a final analysis topic, the effects of inertial instability in tropical cyclones were explored, with a focus on the interaction between inertial instability, STE, and surface pressure changes in typhoons Talas and Roke. Two different model top heights were evaluated, one at 16 km and one at 25 km, to better understand the dynamical interaction between negative EPV air and STE, more specifically, the effects that dry stratospheric intrusions have on surface pressure changes within the typhoon. The 16 km model top run showed upward motion lifting negative EPV air from the outer rainband portion of the storm. A distinctive local high PV circulation developed around each negative EPV anomaly. Additional analysis showed high PV downwelling of stratospheric air around most of the periphery of the typhoon, in association with the inertially unstable regions, disrupting the base of the UTLS. A very active stratospheric gravity wave field was excited in the region of the negative EPV anomalies, disrupting the base of the stratosphere. The 16 km model top also revealed an intrusion of stratospheric air into the core of the storm, resulting in a temporary cessation of storm intensification in terms of surface pressure. Talas' central pressure remained 968 hPa for fourteen hours as the stratospheric dry intrusion affected the storm intensification process.

A 25 km model top revealed similar dynamical features with respect to negative EPV anomalies and a disruption of the UTLS, resulting in local high PV stratospheric intrusions around the anomalies and broad scale high PV stratospheric air wrapping around the periphery of Talas. These features, although quite evident, were significantly more damped and much less intense as in the 16 km model top. In the high top model run the stratospheric intrusion of dry air into the core of Talas was not as strong, which allowed for slight intensification of the storm from 968 hPa to 964 hPa relative to the low top model run in the same fourteen hour period. This finding may prove that inertial instability-induced dry air intrusions may have a significant effect on the intensification or cessation of surface pressure within tropical cyclones.

Future work on inertial instability induced STE and jet intensification events in midlatitude synoptic cyclones is an important factor in the energy and ozone budget of the troposphere. Through the implement of GOES ozone into the 22 April 2005 case, it was seen that a significant amount of stratospheric ozone is affecting the mid to lower troposphere, as negative EPV anomalies disrupt the meridional flow, leading to a poleward and downward STE mechanism around the midlatitude westerly jet.

Additional analysis with respect to STE in midlatitude cyclones will include a statistical computation into the frequency and severity of inertial instability within midlatitude storms in mid to late winter and early spring. As the midlatitiude jet in the northern hemisphere moves well poleward and is quite weak in the northern hemisphere summertime, more analysis will include looking at parts of the globe in the northern hemisphere summer where jets are the most intense, according to the jet climatology of Koch et al. (2006). The focal point with respect to finding more intense jets will be to determine the seasonality and climatology behind inertial instability induced STE in the northern hemisphere. Preliminary models runs within the

UWNMS have proven that an inertial instability induced poleward and downward circulation of stratospheric air into the troposphere is evident in cases from Russia, Australia, and Antarctica. An additional strengthening of the jet in each of these regions was also observed as inertial instability enhanced the divergence in the left exit region leading to inertial flare-ups.

References

Alexander, M. J., Beres, J. H., Pfister, L., 2000: Tropical stratospheric gravity wave activity and relationship to clouds. *J. Geophys. Res.*, **105**, No. D17, 22, 229-22, 309.

Braun, S. A., Montgomery, M. T., Pu, Z., 2004: High Resolution Simulation of Hurricane Bonnie (1998). Part I: The Organization of Eyewall Vertical Motion. *J. Atmos. Sci.*, 63, 19-41.

Brennan, M. J., G. M. Lackmann, and K. M. Mahoney, 2007: Potential vorticity (PV) thinking in operations: the utility of nonconservation. *Weather and Forecasting*, **23**, 168-182.

Cao, Z., and H. R. Cho, 1995: Generation of moist potential vorticity in extratropical cyclones. *J. Atmos. Sci.*, **52**, 3263-3281.

Cao, Z., and D. L. Zhang, 2004: Tracking surface cyclones with moist potential vorticity. *Advances in Atmos. Sci.*, **21**, 830-835.

Clayson, C. A., and L. Kantha, 2008: On turbulence and mixing in the free atmosphere inferred from high-resolution soundings. *J. Atmos. and Oceanic Techn.*, **25**, 833-852.

Duck, T. J., and J. A. Whiteway, 2005: The spectrum of waves and turbulence at the tropopause. *Geophys. Res. Letts*, **32**, L07801.

Eliassen, A., 1962 : On the vertical circlation in frontal zones. Fremlagt I Videnskaps-Akademiets, 147-160, XXIV.

Eliassen, A., and E. Kleinschmidt, 1957: Dynamic Meteorology. In *Handbuch der Physik*, 48, Springer-Verlag, 1-154.

Emanuel, K. A., 1979: Inertial instability and mesoscale convective systems. Part I: Linear theory of inertial instability in rotating, viscous fluids. *J. Atmos. Sci.*, **36**, 2425-2449.

Frank, W. M., Ritchie, E. A. (2001). Effects of vertical wind shear on the intensity and structure of numerically simulated hurricanes. *Mon. Wea. Rev.*, **129**, 2249-2269.

Halcomb, C. E., and P. S. Market, 2003: Forcing, instability and equivalent potential vorticity in a Midwest USA convective snowstorm. *Meteorol. Appl.* , **10**, 273-280.

Hayashi, H., M. Shiotani, M., and J. Gille, 2002: Horizontal wind disturbances induced by inertial instability in the equatorial middle atmosphere as seen in rocketsonde observations. *J. Geophys. Res., **107**,* 148-227.

Hitchman, M. H., Buker, M. L., Tripoli, G. J., Pierce, R.B., Al-Saadi, J.A., Browell, E.V., Avery, M. A. (2004). A modeling study of an East Asian convective complex during March 2001. *J. Geophy. Res.*, **109**, D15S14.

Hitchman, M. H., and C. B. Leovy, 1986: Evolution of the zonal mean state in the equatorial middle atmosphere during October 1978-May 1979. *J. Atmos. Sci.*, **43**, 3159–3176.

Hitchman, M. H., C. B. Leovy, J. C. Gille, P. L. Bailey, 1987: Quasi-stationary zonally asymmetric circulations in the equatorial lower mesosphere. *J. Atmos. Sci.*, **44**, 2219–2236.

Holton, J. R., 2006: *An Introduction to Dynamic Meteorology.* Academic Press, San Diego, CA, 535 pp.

Hoskins, B. J., M. E. McIntyre, and A. W. Robertson, 1985: On the use and significance of isentropic potential vorticity maps. *Quart. J. Roy. Meteor. Soc*., **111**, 877-946.

Jascourt, S., 1997: Convective organizing and upscale development processes explored through idealized numerical experiments, Ph.D. dissertation, 267 pp., Univ. of Wis., Madison.

Joos, H. and H. Wernli, 2012: Influence of microphysical processes on the potential vorticity development in a warm conveyor belt - a cast study with the limited area model COSMO. *Q. J. Roy. Meteor. Soc*., **138**, 407-418.

Knox, J. A., 1997: Possible mechanisms of clear-air turbulence in strongly anticyclonic flows. *Mon. Wea. Rev.*, **125**, 1231-1259.

Knox, J. A., 2003: Inertial instability, in *Encyclopedia of Meteorology*, Elsevier, pp. 1004-1013.

Koch, S. E., Jaminson, B. D., Lu, C., Smith, T. L., Tollerud, E. I., Girz, C., Wang, N., Lane, T. P., Shapiro, M. A., Parrish, D. E., Cooper, O. W., 2005: Turbulence and gravity waves within an upper level front. *J. Atmos. Sci.*, **62**, 3885-3908.

Krishnamurti, T. N., and V.Wong, 1979: A simulation of cross-equatorial flow over the Arabian Sea. *J. Atmos. Sci.*, **36**, 1895-1907.

Kuester, M., Alexander, M. J., Ray, E. A. 2008. A model study of gravity waves over hurricane Humberto (2001). *J. Atmos. Sci.*, **65**, 3231-3246.

Lang, A., 2011: *The Structure and Evolution of Lower Stratospheric Frontal Zones***.** University of Wisconsin-Madison, Department of Atmospheric and Oceanic Sciences, Madison, WI. Call Number: UW MET Publication No.11.00.L2.

Lindzen, R. S., and K. K. Tung, 1976: Banded convective activity and ducted gravity waves. *Mon. Wea. Rev.*, **104**, 1602-1617.

Li, Qingqing, Wang, Yuqing, 2011: Formation and quasi periodic behavior of outer rainbands in a numerically simulated tropical cyclone. *J. Atmos. Sci.*, 997-1020.

Markowski, P., and Y. Richarsdon, 2010: *Mesoscale Meteorology in Midlatitudes*, John Wiley and Sons, Hoboken, NJ, 407 pp.

Mecikalski, J. R., and G. J. Tripoli, 1997: Inertial available kinetic energy and the dynamics of tropical plume formation. *Mon. Wea. Rev*., **126**, 2200–2216.

Montgomery, M. T., and B. F. Farrell, 1991: Moist surface frontogenesis associated with interior potential vorticity anomalies in a semigeostrophic model. *J. Atmos. Sci.*, **48**, 343-367.

Morgan, M. C., 1998: Using piecewise potential vorticity inversion to diagnose frontogenesis. Part I: A partitioning of the Q-Vector applied to diagnosing surface frontogenesis and vertical motion. *Mon. Wea. Rev*., **127**, 2796-2821.

Pavelin, E., J. Whiteway, R. Busen, and J. Hacker, 2001: Airbourne observations of turbulence, mixing, and gravity waves in the tropopause region. *J. Geophys. Res.*, **107**, doi:10.1029/2001JD00U77S.

Pokrandt, P. J., G. J. Tripoli, and D. D. Houghton, 1996: Processes leading to the formation of mesoscale waves in the midwest cyclone of 15 December 1987, *Mon. Wea. Rev*., **124**, 2726– 2752.

Rayleigh, Lord, 1916: On the dynamics of revolving fluids. *Proc. Roy. Soc. London Ser. A*, **92**, 148-154.

Reverdin, G., and G. Sommeria, 1983: The dynamical structure of thte planetary boundary layer over the Arabian Sea, as deduced from constant-level balloon trajectories. *J. Atmos. Sci.*, **40**, 1435-1452.

Sato, K. and T. J. Dunkerton, 2002: Layered structure associated with low potential vorticity near the tropopause seen in high-resolution radiosondes over Japan. *J. Atmos. Sci.*, **59**, 2782-2800.

Sawyer, J. S., 1949: The significance of dynamic instability in atmospheric motions. *Quart. J. Roy. Meteor. Soc.*, **75**, 364-374.

Schultz, D. M., and J. A. Knox, 2007: Banded convection caused by frontogenesis in a conditionally, symmetrically, and inertially unstable environment. *Mon. Wea. Rev*., **135**, 2095-2110.

Schumacher, R. S., and D. M. Schultz, 2000: Upper tropospheric inertial instability: Climatologies and possible relationship to severe weather prediction. In *Preprints, 9th Conference on Mesoscale Processes*, Amer. Meteor. Soc., Boston, 372-375.

Schumacher, R. S., D. M. Schultz, and J. A. Knox, 2010: Convective snowbands downstream of the Rocky Mountains in an environment with conditional, dry symmetric, and inertial instabilities. *Mon. Wea. Rev.*, **138**, 4416-4438.

Shapiro, M. A., 1974: A multiple structured frontal zone-jet strea system as revealed by meteorologically instrumented aircraft. *Mon. Wea. Rev.,* **102,** 244-253.

Shapiro, M. A., 1976: The role of turbulent heat flux in the generation of potential vorticity in the vicinity of upper level jet stream systems. *Mon. Wea. Rev.* **104,** 892-906.

Shapiro, M. A., 1978: Further evidence of the mesoscale and turbulent structure of upper level jet stream-frontal zone systems. *Mon. Wea. Rev.*, **106**, 1100-1111.

Shapiro, M. A., 1979: Turbulent mixing within tropopause folds as a mechanism for the exchange of chemical constituents between the stratosphere and troposphere. *J. Atmos. Sci.* **37,** 994-1004.

Shapiro, M. A., 1981: Frontogenesis and geostrophically forced secondary cirualtions in the vicinity of jet stream-frontal zone systems. *J. Atmos. Sci.,* **38**, 954-972.

Stevens, D. E., and P. E. Ciesielski, 1986: Inertial instability of horizontally sheared flow away from the equator. *J. Atmos. Sci*., **43**, 2845-2856.

Stohl, A., et al. 2003: Stratosphere-troposphere exchange: A review, and what we have learned from STACCATO. *J. Geophys. Ress.*, **108**, 8516.

Stout, J. E., and J. A. Young, 1983: Low-level monsoon dynamics derived from satellite winds. *Mon. Wea. Rev*., **111**, 774-798.

Taylor, G. I, 1923: Stability of a viscous liquid contained between two rotating cylinders. *Phil. Trans. Roy. Soc. London Ser. A*, **223**, 289-343.

Tomas, R. A., and P. J. Webster, 1997: The role of inertial instability in determining the location and strength of near-equatorial convection. *Quart. J. Roy. Meteor. Soc*., **123**, 1445-1482.

Tripoli, G. J., 1992a: An explicit three-dimensional nonhydrostatic numerical simulation of a tropical cyclone, *Meteorol. Atmos. Phys.*, **49**, 229– 254.

Tripoli, G. J., 1992b: A nonhydrostatic numerical model designed to simulate scale interaction. *Mon. Wea. Rev*., **120**, 1342– 1359.

Uccellini, L. W. Koch, E. Steven, 1987: The synoptic and possible energy sources for mesoscale wave disturbances. *Mon. Wea. Rev.*, **115**, 721-729.

Wang, T.-A. Y. L. Lin, 1998: Wave ducting in a stratified shear flow over a two-dimensional mountain. Part I: General linear criteria. *J. Atmos. Sci.*, **56**, 412-436.

Wang, Y., 2008: How do outer spiral rainbands affect tropical cyclone structure and intensity. *J. Atmos. Sci.*, **66**, 1250-1273.

Whiteway, J. A., E. G. Pavelin, R. Busen, J. Hacker, and S. Vosper, 2003: Airborne measurements of gravity wave breaking at the tropopause. *Geophys. Res. Letts*., doi:10.1029/2003GL018207.

Wu, C-C., Kurihara, Y., 1996: A numerical study of the feedback mechansims of hurricane environment interaction on hurricane movement from the potential vorticity perspective. *J. Atmos. Sci.* , Vol. **53**, 2264-2282.

Zhang, D.-L., H. R. Cho, 1991: The development of negative moist potential vorticity in the stratiform region of a simulated squall line. *Mon. Wea Rev.*, **120**, 1322-1341.